ABSTRACT

Title of Dissertation: DESIGN AND FABRICATION OF ELECTROTHERMAL MICROMOTORS AND COMPLIANT MECHANISMS FOR SPATIAL PARALLEL MICROMANIPULATORS

Wei-Jen Cheng, Doctor of Philosophy, 2005

Directed By: Associate Professor Don DeVoe
Department of Mechanical Engineering

In this dissertation a new class of spatial micromechanisms employing compliant joints and electrothermal motors has been developed. The spatial micromechanisms contain three limbs driven by individual electrothermal linear motors to form multiple degree-of-freedom (DOF) manipulators. At the coaxial point of the actuated limbs, a platform acts as the end effector of the device. Each limb in this spatial mechanism interconnects compliant pseudo-revolute joints, which are capable of providing either in-plane or out-of-plane rotations. Mechanisms are demonstrated using polysilicon surface micromachining, and a new four-layer UV-LIGA fabrication process is also presented for future production of high aspect ratio spatial micromechanisms.

Linear motors are developed to provide bi-directional continuous motions to drive the spatial mechanism. Individual electrothermal actuators within a linear motor employ saw-toothed impactors to provide a synchronized locking/pushing motion

without needing a secondary clamping actuator. These saw-toothed linear motors provide a platform for accurate open-loop position control, continuously smooth motion, high motion resolution, and long life operation.

Electrothermal V-beam actuators using multiple arrayed beams have been shown to provide large output forces up to several mN, sufficient for the spatial micromechanisms developed in this work. Taking advantage of a modeling approach based on the pseudo-rigid-body model, a new force and displacement model for the electrothermal V-beam actuators is developed and shown to provide good agreement with experimental results. The optimization design for the thermal actuators is also discussed to reduce actuation power.

Pseudo-rigid-body modeling is used to simplify the designed compliant spatial mechanisms, allowing the well-known rigid body method to replace the cumbersome matrix method for compliant mechanism analysis. Based on the pseudo-rigid-body model, inverse kinematics is used to find the workspace of a typical microscale mechanism, together with the required movement for each linear motor to allow the end effector to reach a desired position. Dynamic analysis of the mechanism is applied to determine the maximum required forces for each actuator. The manipulator workspace volume defined by maximum link lengths and joint rotation angles is determined by using the Monte Carlo method. A systematic design procedure is finally proposed to enable effective compliant micromanipulator designs.

DESIGN AND FABRICATION OF ELECTROTHERMAL MICROMOTORS AND COMPLIANT MECHANISMS FOR SPATIAL PARALLEL MICROMANIPULATORS

by

Wei-Jen Cheng

Dissertation submitted to the Faculty of the Graduate School of the
University of Maryland at College Park in partial fulfillment
of the requirements for the degree of
Doctor of Philosophy
2005

Advisory Committee:

Associate Professor Don DeVoe, Chairman / Advisor
Professor Balakumar Balachandran
Professor John Melngailis
Associate Professor Peter Sandborn
Associate Professor Guangming Zhang

Dedication

To my fiancée Chunli Shen and my parents for their support and encouragement on this work.

Acknowledgements

I would like to thank my advisor, Dr. Don L. DeVoe, for his guidance and support throughout this work. I also appreciate my former advisor, Dr. Lung-Wen Tsai, for his instruction and encouragement. I am indebted to Tom Laughran and Nolan Ballew for their fabrication assistance, and to Zhen Z. Wu for his kind aid on electric circuit design. Finally I am grateful to my friends and colleagues at Maryland Microfluidics Lab for their assistance and advice. Thanks should also be extended to DARPA and NSF for funding this research.

TABLE OF CONTENTS

LIST OF TABLES

LIST OF FIGURES

NOMENCLATURE

A Cross-section area of the V-beam,

a Thickness of the prismatic joint,

b_i (b) Specific distance,

CE_i The i-th constraint equation,

c_i Degree of constraint on relative motion imposed by the joint i,

c_i (c) Specific distance,

c_n Specific heat of nickel,

D Density of the deposited metal in grams per cubic centimeter,

D_n Density of nickel,

Dof Degree of freedom in the mechanism,

d_i (d) Specific distance,

dl_1 V-beam deflection generated from its first quarter length,

dl_2 V-beam deflection generated from its second quarter length,

d_{max} Maximum displacement in a free loading condition,

d_r Required actuator deflection,

d_t Total tip displacement of the thermal V-beam,

E Young's modulus of nickel,

e_i (e) Specific distance,

F Force delivered from the thermal actuator on the moving direction of the slider,

F_a Actuator maximum force,

F_e Elastic force,

F_i Actuator force for the i-th limb of the manipulator,

F_n Net output force,

F_r Required actuation force delivered from the thermal actuator,

F_s Loading force generated from the spatial mechanism at the end of the slider,

F_t Output force along the moving direction of yoke,

F_{th} Thermal force,

f_i (f) Specific distance,

g Acceleration of gravity,

g_a Gap between the beam and the substrate,

h Thickness of the beam,

h_s Spring thickness,

I Moment inertia of the V-beam,

I_s Moment inertia of the spring beam,

J Current density through the beam,

j_n Number of joints,

K Spring constant of the flexure,

K_Θ Stiffness coefficient in the pseudo-rigid-body model,

K_{ip} Torsional spring constant of the in-plane joint,

K_{op} Torsional spring constant of the out-of-plane joint,

K_s Strip calibration constant from the manufacturer,

k_a Thermal conductivity of air,

k_n Thermal conductivity of nickel,

L Total V-beam length between two anchors,

L_1 Length of the out-of-plane compliant joint near the linear motor,

L_2 Length of the in-plane compliant joint,

L_3 Length of the out-of-plane compliant joint near the moving platform,

L_b Total length of the thin beam acted as a compliant joint,

L_c Length of the cantilever beam,

L_{eff} Effective total link length of the manipulator,

L_g Length of the rigid block between out-of-plane joints and in-plane joints,

L_h Distance between the center of the platform and the platform edge connected with the out-of-plane joint,

L_i Length of the small divided element i,

L_s Length of each folded spring,

L_{total} Total V-beam length in its first quarter after thermal expansion,

L'_{total} Total V-beam length in its second quarter after thermal expansion,

m_c Total mass of the connecting bar,

m_p Total mass of the moving platform,

m_s Mass of the prismatic joint,

N Normal force,

n Total number of generalized coordinates,

n_{in} Total number of points which fall inside the workspace,

n_L Number of links including the fixed link or base,

n_t Total selected points within the rectangular prism,

PI Workspace performance index,

P_a Evaluative parameter for the actuator performance,

P_c Total power consumption,

P_i Distance between the origin of the global coordinate system and the prismatic joint's end of the *i*th limb,

Q_X X component of the point *Q* expressed in the global coordinate system,

Q_Y Y component of the point *Q* expressed in the global coordinate system,

Q_Z Z component of the point *Q* expressed in the global coordinate system,

Q_X^i X component of the point *Q* expressed in the global coordinate system with the parameters of the *i*-th limb,

Q_Y^i Y component of the point *Q* expressed in the global coordinate system with the parameters of the *i*-th limb,

Q_Z^i Z component of the point *Q* expressed in the global coordinate system with the parameters of the *i*-th limb,

Q_{x_i} X component of the point *Q* expressed in the xyz-local coordinate of the *i*-th limb,

Q_{y_i} Y component of the point *Q* expressed in the xyz-local coordinate of the *i*-th limb,

Q_{z_i} Z component of the point *Q* expressed in the xyz-local coordinate of the *i*-th limb,

q_j The *j*-th generalized coordinate,

R Electrical resistance at temperature *T*,

R_0 Electrical resistance at temperature T_0,

S Shape factor,

S_d Deposit stress in pounds per square inch (psi),

s Slope of the triangular wave signal,

T Temperature,

$T_{(x)}$ Temperature on the position *x* of the beam,

T_0 Initial reference temperature,

T_d Deposit thickness in inches,

T_∞ Ambient temperature,

t Time,

t_f Film thickness,

t_p Thickness of the moving platform,

U Number of scales from the stress analyzer,

V_a Actuator total volume,

V_c Actuation voltage the moment the impactor sawteeth initially contact the slider,

V_m Actuation voltage for the impactor teeth to reach the sawteeth bottom limit of the slider,

V_p Velocity of the moving platform,

V_w Workspace volume,

W Deposit weight in grams,

w Width of the beam,

w_s Spring width,

α Thermal expansion coefficient of nickel,

β Offset angle of the thermal V-beam,

β_c Temperature coefficient of resistance,

δ Tip deflection of the cantilever beam,

ε_a Actuator maximum displacement,

ε_{th} Thermal strain,

ϕ_i Rotation angle compared the global coordinate system with the local one settled on the *i*th limb,

γ Characteristic radius factor in the pseudo-rigid-body model,

γ_1^i Characteristic radius factor of the first out-of-plane compliant joint located in the *i*-th limb near the linear motor,

γ_2^i Characteristic radius factor of the in-plane compliant joint located in the *i*-th limb,

γ_3^i Characteristic radius factor of the second out-of-plane compliant joint located in the *i*-th limb near the moving platform,

λ_i Lagrange multiplier,

μ Friction coefficient,

Θ Pseudo-rigid-body angle,

θ Angle of the wedge-shape tooth,

θ_1^i Rotation angle of the out-of-plane joint located in the *i*th limb,

θ_2^i Rotation angle of the in-plane joint located in the *i*th limb,

ρ Resistivity of nickel,

ρ_0 Electrical resistivity of nickel at temperature T_0,

$\rho_i(T)$ Temperature-dependent resistivity of nickel in the small divided element *i*,

σ Internal stress of the film,

σ_{th} Thermal stress,

τ_1 The first-mode time constant,

ν Poisson's ratio,

$\hat{L}$ Lagrangian function,

$\hat{Q}_j$ Generalized external force,

$\hat{T}$ Total kinetic energy of the system,

$\hat{T}_c$ Kinetic energy of three connecting bars,

$\hat{T}_c^i$ Kinetic energy of the connecting bar in the *i*-th limb,

$\hat{T}_p$ Kinetic energy of the moving platform,

$\hat{T}_s$ Total kinetic energy of three sliders,

$\hat{V}$ Total potential energy of the system,

$\hat{V}_c^i$ Potential energy of the connecting bar on the limb *i*,

$\hat{V}_G^i$ Gravitational potential energy of the limb *i*,

$\hat{V}_{ip}^i$ Elastic deformation energy of the in-plane joint connected on the limb *i*,

$\hat{V}_{op}^i$ Elastic deformation energy of the out-of-plane joint attached on the limb *i*,

$\hat{V}_p$ Potential energy of the platform,

$\hat{V}_s$ Total potential energy of three sliders.

Chapter 1

Introduction

1.1 Overview

Micro-scale devices have many potential advantages over their macroscale counterparts, such as small size and weight, low energy consumption, short response time, high resolution, and low cost. In addition, many MEMS fabrication processes are compatible with parallel fabrication methods used in the integrated cuicuit manufacturing industry, allowing hundreds or thousands of devices to be created simultaneously to reduce the average cost of each chip. Moreover, because of the small dimensions, power requirements of MEMS devices are generally very small, with most devices only needing mW or lower power levels to operate.

This dissertation addresses the development of microscale spatial mechanisms capable of taking advantage of these benefits offered by established microfabrication methods. A parallel manipulator is defined by its kinematic structure, which takes the form of a closed-loop kinematic chain, unlike serial manipulators which consist of open-loop chains. In the macro world, many kinds of parallel manipulators have been developed, for example those depicted in Figure 1.1 [1] and Figure 1.2 [2]. Such parallel mechanisms offer several key advantages, such as high stiffness, low inertia, and high payload capacity. Although serial manipulators can offer larger workspace limits, such devices are not easily ported to the microscale world. The primary disadvantage of serial manipulators is that actuators must be mounted on the mechanism's moving joints. This

is a major constraint for MEMS based devices due to practical fabrication limitations. By contrast, actuators in a parallel manipulator can always be attached to the fixed base, and are thus well suited to MEMS manufacturing processes.

For a planar mechanism, the loci of all points in all links can be conveniently drawn on a plane, but actually they lie on parallel planes. A mechanism is said to be a spherical mechanism if the motions of all particles in the bodies lie on concentric spheres. A manipulator is called a spatial manipulator if at least one of the moving links in the mechanism possesses a general spatial motion that cannot be characterized as planar or spherical motion [1]. Since the devices of interest in this work consist of micro-scale parallel mechanisms providing spatial motion, with integrated actuators for driving the mechanism located within the base link, they may be termed spatial parallel micromanipulators.

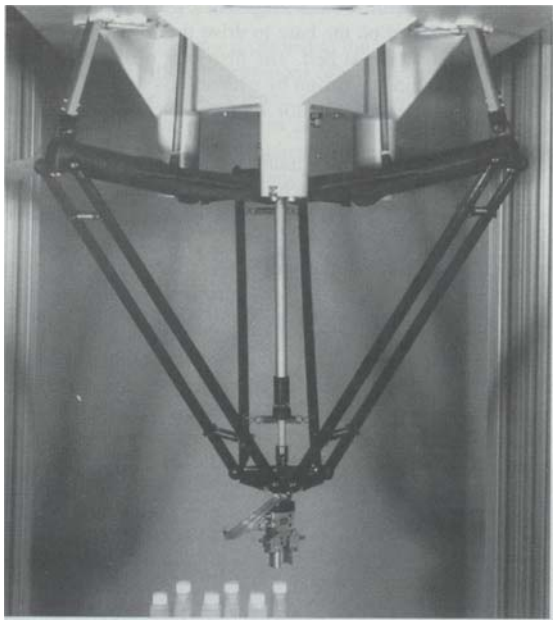

Figure 1.1: A four degree-of-freedom parallel manipulator. (From Demaurex Robotique & Microtechnique S.A., Switzerland.)

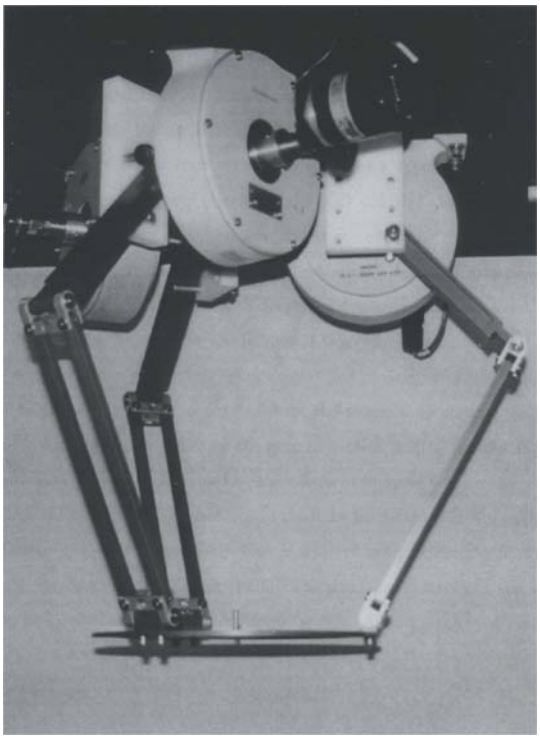

Figure 1.2: A three degree-of-freedom parallel manipulator with only translational movement. (From University of Maryland.)[2]

An important requirement for the proposed spatial parallel micromechanisms is a high force, large displacement motor that can be used to position individual elements of the mechanism. For the sake of a miniature actuator, it is very difficult to generate a high force and a rotating motion from a motor using MEMS fabrication. Thus linear motors are selected to drive the parallel manipulators. Moreover, there are many different kinds of linear motors which have been described in the literature, as discussed in the following section. Ultimately, thermal linear motors will be used for the actuators in the present work due to their ability to provide high force and large displacement output [3].

The ultimate objective of this research is to build microscale parallel manipulators that can be integrated with other devices. There are many potential applications for such

devices. For example, if a gripper is assembled on the bottom of the moving platform of the manipulator, the device can become the micro carrier used to transfer cells or beads. If a cutting blade is attached on the platform, then it may be used as a tool for minimally invasive surgery. If a mirror is attached on the platform, the device can become a multidimensional optical guide.

In previous research at the Maryland MEMS Laboratory at the University of Maryland, the commercially-available MUMPs manufacturing process was selected to fabricate initial parallel manipulators. More details about such manufacturing process will be discussed later. The thermal motors fabricated by this process functioned well and provided a useful testbed for considering various motor and mechanism designs, but they could not supply sufficient force required by the application. Inadequate thickness of the thermal beam was believed to cause the insufficient force due to the limitations of MUMPs process. In this dissertation, a UV-LIGA fabrication process is introduced to overcome this drawback of surface micromachining. On the other hand, strong microstructures can be made from this UV-LIGA manufacturing process.

This dissertation is organized as follows. Several microactuators, linear micromotors, and relevant fabrication processes for multi-layered microstructures are reviewed in the remainder of Chapter 1. Two different fabrication methods for the designed parallel mechanisms, namely MUMPs and UV-LIGA processes, are separately described in Chapter 2. Theoretical analyses of spatial manipulators are combined together in Chapter 3. Since the compliant nature of the mechanisms is the main characteristic which distinguishes the designed mechanisms and actuators, the model analysis is substantially more complicated compared to the traditional rigid body

analysis. To simplify this analysis, the pseudo-rigid-body model will be introduced and applied to analysis of thermal V-beam actuator force and displacement, and the analysis of spatial micromechanism kinematics and dynamics. In Chapter 4, the optimal thermal actuator design and the design process for entire spatial mechanisms are discussed. In Chapter 5, the development of saw-toothed linear motors used to actuate spatial micromechanisms is described. Future work for the spatial micromanipulators and key contributions for this research are provided in Chapter 6.

1.2 Microactuator Review

Since traditional motors are too big to mount on a silicon chip to actuate a micromechanism, microactuators and linear micromotors based on MEMS fabrication methods are required to actuate microscale mechanisms. The following surveys provide an overview of MEMS technologies which may be suitable for actuation of microscale mechanisms.

Many different kinds of microactuators have emerged in recent years. Each kind of actuators possesses its own unique benefits, such as providing large force, consuming less power, offering long displacement, and holding high actuating speed. However, none of them could carry all advantages, in fact, some trade-offs exist between these advantages. For example, most large-force microactuators are only able to contribute very small displacement. The following section will discuss those different kinds of actuators.

Utilizing the electrostatic force to actuate the device is the first kind of those actuators. The main benefit for this kind of actuator is low power consumption. Comb-drive is a representative type of electrostatic actuator. Although each comb-finger only

provides a tiny force, some adaptations, such as adding the numbers of fingers [41], reducing the gap between moving fingers and stators [47], or stacking large-area fingers [48] can magnify the force up to the scale of milli-Newton or several Newton. Changing the motion direction of the comb-drive into laterally driven style is another way to increase the force [49][50], but such method will reduce the total displacement of the actuator. To extend the displacement, Legtenberg et al. [51] used a curved electrode to increase the deflection of the cantilever beam. Distributed Electrostatic Micro Actuator (DEMA) [36] shown in Figure 1.3 is another type of electrostatic actuator. Its working principle is stacking many small driving units, which own two wave-like insulated electrodes, to generate accumulating contraction during actuation. Scratch-Drive-Actuator (SDA) [34][45] is another good example for using the electrostatic force to pull down the parallel plate so as to let the foot of parallel plate move forward. After releasing the stored distortion energy, the parallel plate snaps to its original shape. Figure 1.4 displays the operational principle of the Scratch-Drive-Actuator. Shuffle motor [27] also uses the electrostatic force to pull down the actuator plate, so as to change the shape of the actuator plate and to move the back clamp. Then the back clamp is applied the power to fix in the original place. Finally, the actuator plate is discharged to move the front clamp forward. The whole sequential operation process is shown in Figure 1.5.

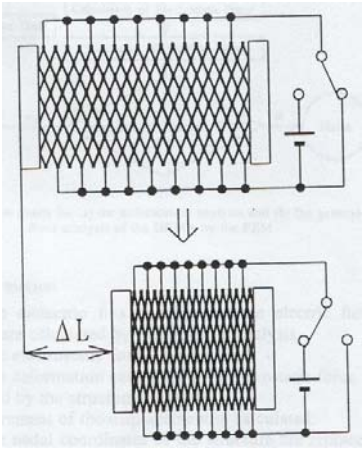

Figure 1.3: Distributed Electrostatic Micro Actuator (DEMA) [36].

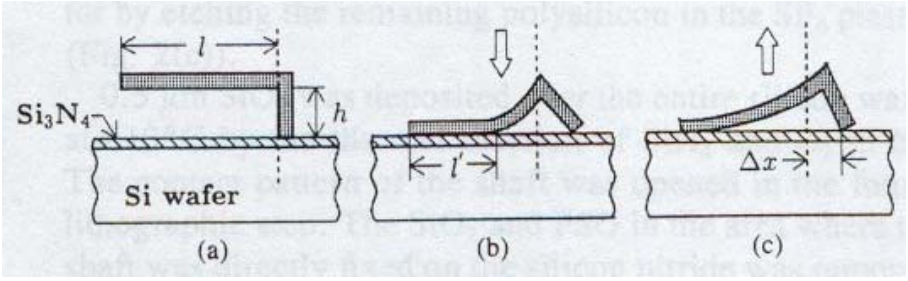

Figure 1.4: Operational principle of the Scratch-Drive-Actuator (SDA) [34].

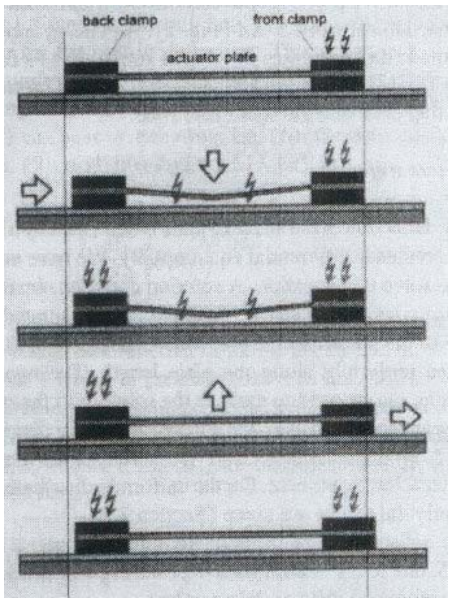

Figure 1.5: Operational process of the shuffle motor [27].

Employing the thermal expansion force to actuate the device is the second group of actuators. U-shape beam [38][52] and V-shape beam [3][5][53][54] are the two main kinds of thermal beams using in this type of actuators. U-shape beam shown as Figure 1.6 connects a narrow hot arm and a wider cold arm in a parallel format. When the power is applied on the both anchors of U-beam, the thermal deflection of a hot arm is greater than that in a cold arm. Thus the tip of U-beam curls up to create the displacement, which is very similar to the behavior of thermal bimorph. Unlike the tip motion of U-beam, the symmetric configuration of V-beam on the both sides of a yoke provides the purely translational movement on the tip of the yoke. Figure 1.7 illustrates that the deformation from thermal expansion thrusts the middle tip of the V-beam to move forward after power is applied on the both anchors.

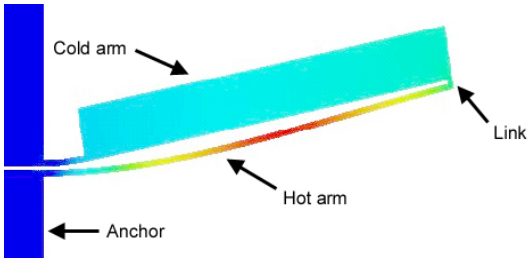

Figure 1.6: Deformation of an electrothermal U-beam microactuator undergoing power on the anchors.

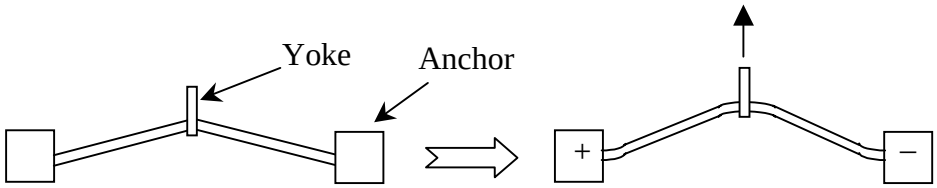

Figure 1.7: Deformation of a thermal V-beam while applying power on the both anchors.

Another kind of actuator is based on the special trait of metal, called Shape Memory Alloy (SMA) [55], which inheres the thermally induced crystalline transformation between the ductile phase and the high strength state. In martensitic phase at low temperature, SMA becomes ductile and easy to deform. However, it transforms to the austenitic phase during heating and will restore to its original shape. Such characteristic can be used to provide force and generate motion for an actuator.

Magnetic actuator is another useful actuator in MEMS systems. Wright et al. [56] mentions a large-force, fully integrated, electromagnetic actuator used for microrelay applications. According to the experimental data, a coil current of 80 mA generates 200 μN force on the testing actuator about a footprint of 8 mm^2.

Since actuators can be scaled to any dimension and be operated under various conditions, one suitable parameter, P_a, was defined to neutralize those above differences in order to evaluate the performance of actuators of different types. The definition of P_a is [37]

$$P_a = \frac{F_a \varepsilon_a}{V_a} \tag{1.1}$$

where F_a is the actuating force, ε_a is the maximum displacement of actuators, and V_a is the total actuator volume. Table 1.1 shows the evaluative parameter for several different types of actuators. Based on the results of this table, the electrostatic actuators hold the lowest density and the SMA actuators possess the highest. Although SMA actuators provide huge force, their linear deformation strain is limited to about 8% [55], which greatly constraints their applications under the circumstances of long displacement.

Table 1.1: Evaluative parameter P_a (J/m^3) for different types of actuators [37].

Type of actuators	P_a (J/m^3)
Electrostatic comb drive	10^2
Electrostatic parallel plate	10^3
Magnetic	10^4
Thermo bimorph	10^5
Thermo pneumatic	10^6
Shape memory alloy	10^7

1.3 Linear Micromotors

Many linear micromotors had been invented and fabricated in the past years. Several kinds of actuators discussed above are used to form various linear motors, such as electrostatic [24][25][26], electrothermal [5][28], acoustic [43][44], electromagnetic [39][57], and piezoelectric linear motors.

Most electrostatic linear motors employ the comb-drive actuators. In order to enhance the actuating force, the laterally driven parallel structure is a common practice for this kind of motor. Meanwhile, to extend the total travel of the linear motor, two pairs of sequentially reciprocal pawls located on opposite sides of the slider straight drive the motor's slider. The operational principle of this linear motor is shown in Figure 1.8.

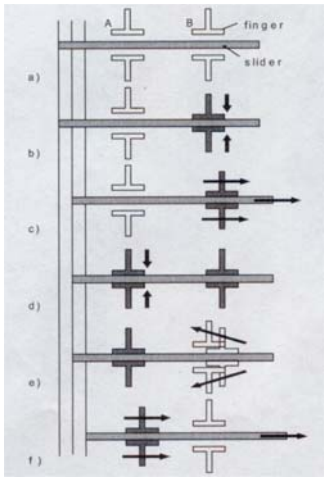

Figure 1.8: Operational sequence of an electrostatic linear motor [24].

The actuating principle of electrothermal linear motor is similar to the previous electrostatic one. The thermal actuators replace the above electrostatic ones, which are

behind the reciprocal pawls, to move the slider. Figure 1.9 shows the operational principle for one kind of thermal linear motors. Because the motion for this kind of thermal or electrostatic motor is intermittent, this linear motor is also called a step motor or vibromotor.

The magnetic micromotor is another type of linear micromotor. It utilizes the change of magnetic field to move a permanent magnet as a slider on guided channels or grooves. For example, a magnet can synchronously move with the rotating or traveling magnetic fields generated by planar coils on the silicon substrates [39]. Figure 1.10 shows one kind of magnetic micromotors. To improve the performance of the magnet motion, an additional long rectangle coil, which is used to generate a levitating force for the magnet, can be built on the lowest layer beneath the magnetic motor described above [57].

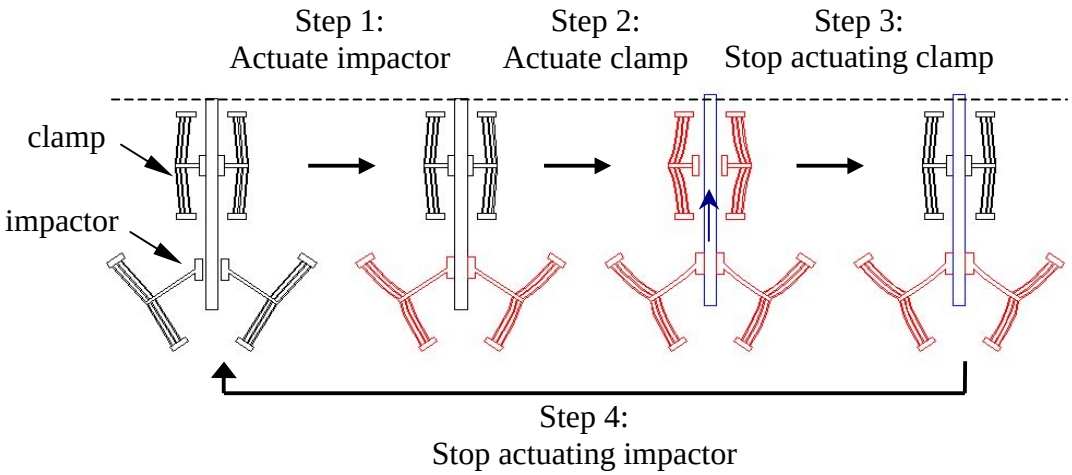

Figure 1.9: Operational sequence of an electrothermal micromotor [5].

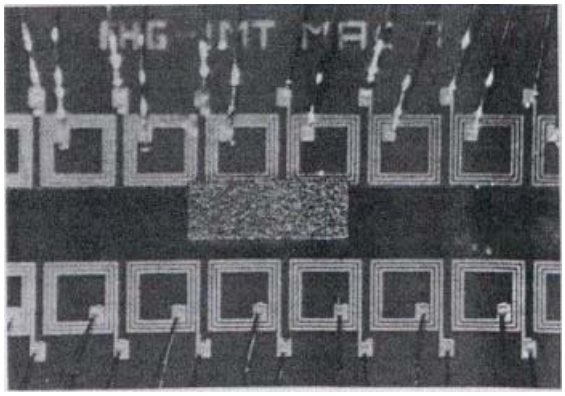

Figure 1.10: Magnet micromotor on a silicon substrate [39].

Surface acoustic wave (SAW) motor [43] demonstrated in Figure 1.11 is the final type of linear micromotor in this section. When high frequency voltage is applied on an interdigital transducer (IDT) on the piezoelectric substrate made from $LiNbO_3$ 128^o Y-cut material, the Rayleigh wave is generated and propagates on the surface of this elastic material. Due to Rayleigh wave traveling on this solid surface, particles inside the solid move along with elliptical loci which provide a longitudinal displacement to move the object (slider) above the surface. A pre-loaded force on the top of the slider must be strong enough to increase the frictional force between the slider and the driven surface. The magnetic force between the magnet and iron plate will provide the pre-loaded force, and such force can be adjusted by changing the thickness of the plastic film as shown in Figure 1.11. This kind of SAW motor owns many advantages, such as high output force, high speed, long stroke up to centimeter scale, high energy density, and high-resolution positioning [44].

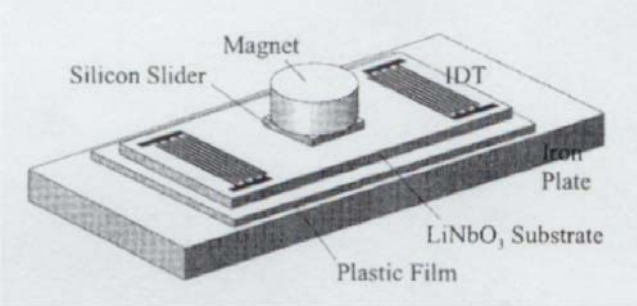

Figure 1.11: Surface acoustic wave linear motor [43].

Figure 1.12 shows the comparison for different kinds of actuators and motors between their minimum resolution and maximum speed. According to the compared results, SAW owns the best performance in this competition. On the other hand,

Figure 1.13 displays another comparison between the driven voltage and the force density for those various actuators and linear motors. SDA and SAW are good selections for high force density outputs, but their actuation voltages are too high to compatible with CMOS chip. Therefore, if a low actuation voltage and a high force density are required, the thermal actuator is the best choice.

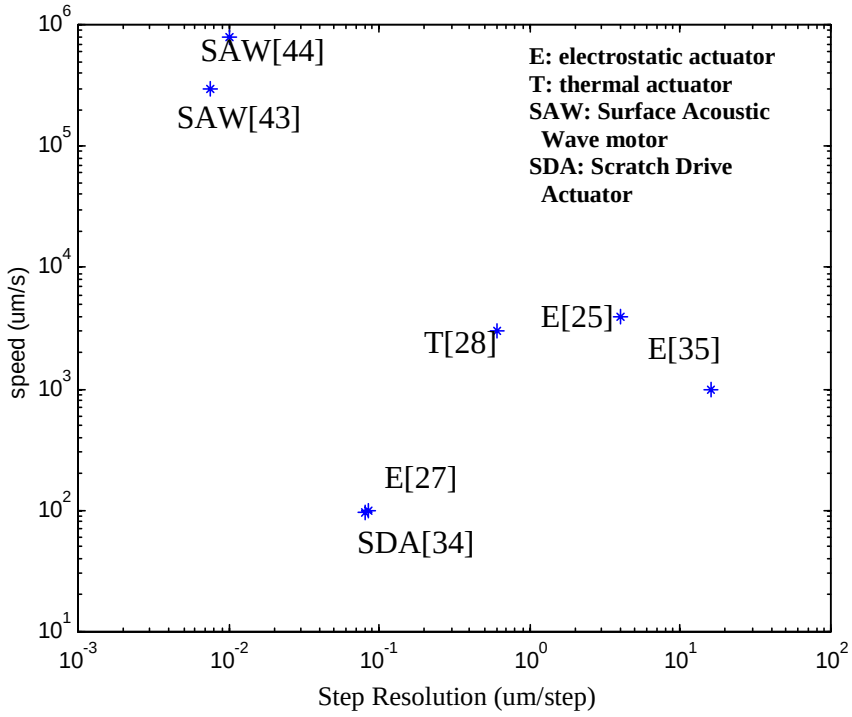

Figure 1.12: Comparison of different actuators between step resolution and speed.

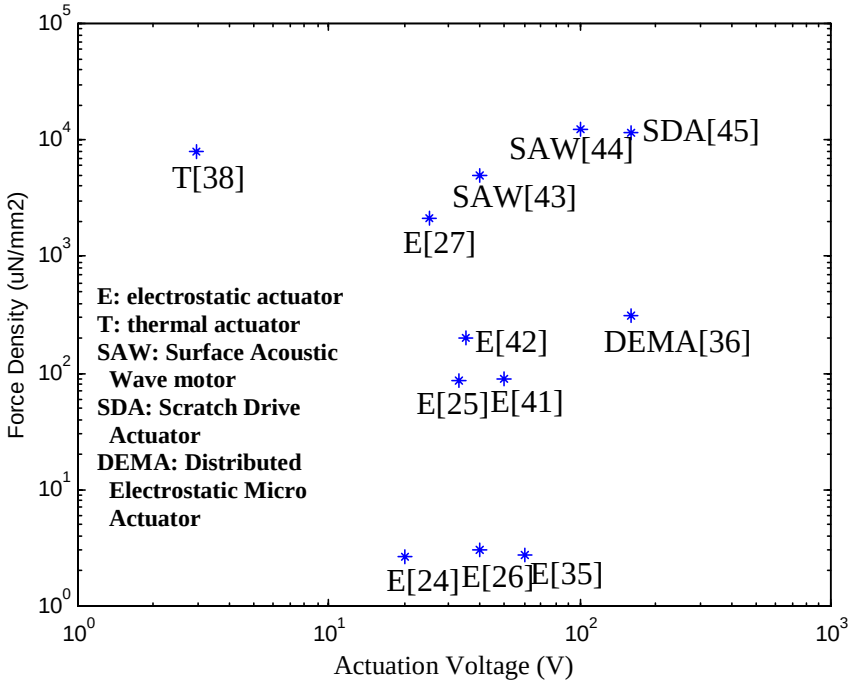

Figure 1.13: Comparison of different actuators between actuation voltage and force density.

1.4 Microstructure Manufacturing Processes

A number of commercial multilayer polysilicon surface microfabrication methods are currently available, such as MUMPs [33] and SUMMiT [8]. However, these processes suffer from constraints to the thickness of each thin layer (<3 um) and limits on the total number of structural layers. While several approaches to form high aspect ratio 3-D structures from surface micromachined features have been explored, such as assembly of hinged polysilicon [6] or polyimide [12] structures, these methods only use one-layered structures to create a 3-D feature, and a large area of silicon base is required to fabricate the basic 2-D structures. Besides, the process of assembly is not easy, and significantly limits the range of features which can be created. Thus, other methods to manufacture 3-D structures have been considered in the literature to avoid the limitations imposed by surface micromachining.

A novel bulk micromachining technology for silicon multilevel microstructures was demonstrated by using a multi-layer stacked wafer bonding method [11] to fabricate fully 3-D microstructures. In this method, deep reactive ion etching (DRIE) is used to make the silicon structure for each layer on a SOI wafer, and then the whole structure is created by the bonding process with multiple aligned wafers. Similarly, using the deep x-ray lithography (DXRL) to form the each level structure from LIGA process, the multi-layered nickel metal structures are accumulated and bound by the procedure of diffusion bonding or solid-state welding [10]. Another unlimitedly layered structure can be formed a 3-D metal mechanism without a binding process by using a planarization with a sacrificial metallic mold (PSMM) as a sacrificial layer, a planarization layer, and a seed layer for the next-level electroplating process to grow multi-level structures [9].

Chapter 2

Fabrication

2.1 MUMPs Polysilicon Surface Micromachining

2.1.1 Process Overview

The MUMPs process [33] offered by Cronos Integrated Microsystems is a commercial fabrication process with seven sequential deposited layers, incluing two layers of structural polysilicon. The process restricts the thickness and the material of each layer. Figure 2.1 shows the processing sequence of the seven-layered structure. In the micromanipulator designs described in this dissertation, two polysilicon layers (Poly1, Poly2) are used as the structures to form the manipulator, and the two oxide layers (Oxide1, Oxide2) are sacrificial layers. The lowest layer, silicon nitride, serves as an electrical insulator, and the Poly0 layer provides an electrical ground plane for electrical routing and ground biasing. The top gold metal layer is employed for both low-resistivity electrical routing and as a bond pad top layer. Details about the fabrication and release process are well documented in Schreiber's thesis [4] and the MUMPs design handbook [33].

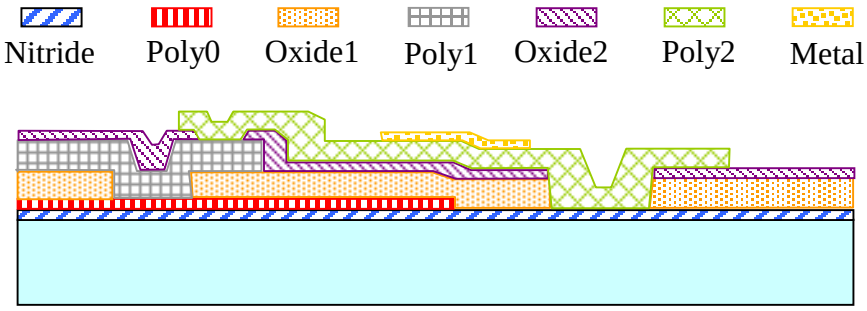

Figure 2.1: Diagram of the seven-layered structure in MUMPs process.

2.1.2 MUMPs Linear Motor Fabrication

Linear micromotors are used to actuate the spatial mechanism in this research. The initial study described in this section focuses on the design for this type of linear motor. Figure 2.2 depicts a previously-developed push-clamp micro stepper motor [3][4] which includes three pairs of thermal actuators symmetrically located on the both sides of a central linear slider, generating equal lateral and longitudinal forces on the slider edge. Two pairs of arrayed thermal V-beam actuators with angled yokes are used to strike and move the slider in both forward and reverse directions. A pair of arrayed V-beam actuators with vertical yokes is used as slider clamps to prevent unwanted slider movement. The operation sequence of this linear motor will be discussed in the next section.

A new electrothermal micromotor design was developed in this work, as shown in Figure 2.3. Unlike the push-clamp micromotor, the new design contains two pairs of thermal actuators with vertical yokes symmetrically located on the both sides of the central slider. The wedge-type teeth on the slider present a distinctive feature of this design. Slipping motion between the two mating wedges provides simultaneous pushing and locking actions. If a reverse direction of movement is required, a second set of two

pairs of thermal actuators with symmetrically-shaped teeth can be added. The operational sequence of this motor will be described in the next section.

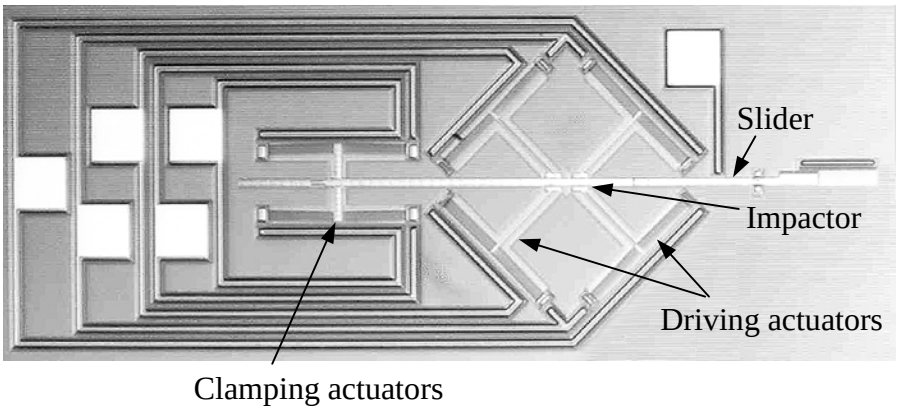

Figure 2.2: Push-clamp micro stepmotor using MUMPs process.

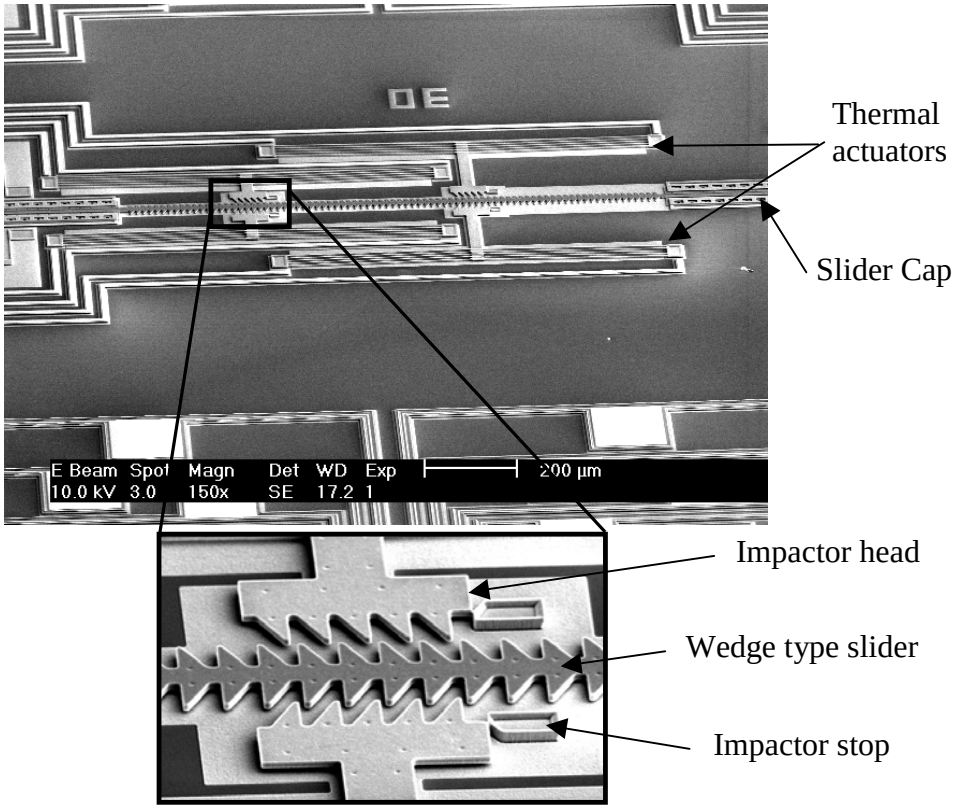

Figure 2.3: Linear motor with the wedge-type impactor actuated by thermal actuators using MUMPs process.

A spatial parallel manipulator displayed in Figure 2.4 is driven by three thermal linear micromotors with wedge-type sliders. Three thermal linear motors settle on the equal angle of a surrounding mechanism to provide the actuation motion for a center moving platform controlled by its surrounding three limbs. However, because of the limitations of MUMPs fabrication process, the thermal actuators cannot supply enough forces to drive the spatial mechanism. The insufficient thickness of thermal V-beams and the number of arrayed beams are believed to be the reasons for providing inadequate force.

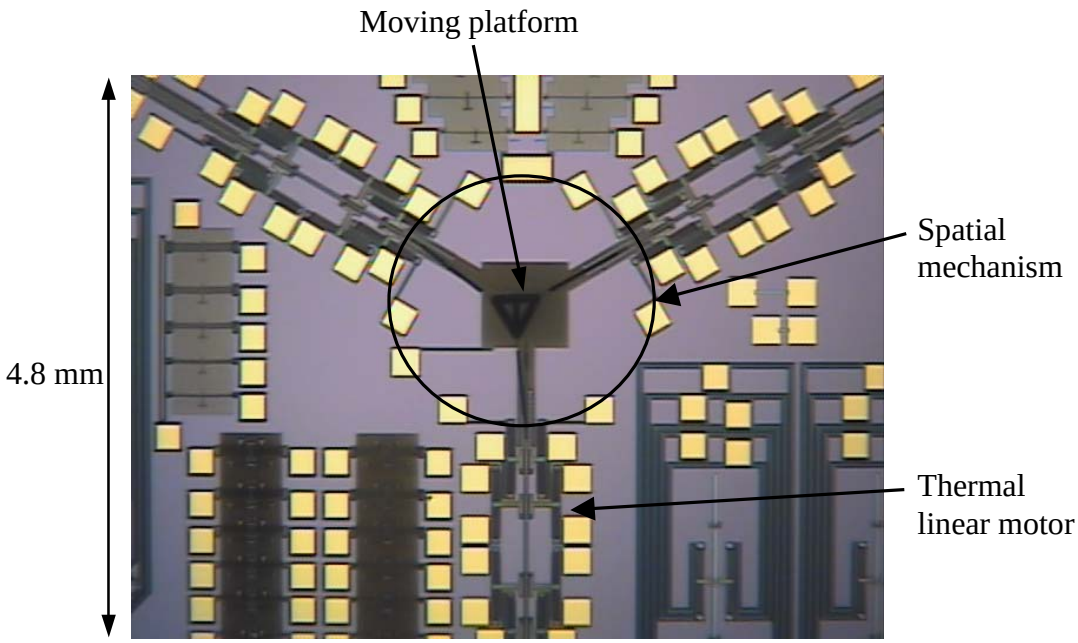

Figure 2.4: Spatial mechanism actuated by linear micromotors using MUMPs fabrication process.

2.1.3 Linear Motor Characterization

Push-clamp stepmotor

In order to drive impactors and clamp in the push-clamp stepmotor, sinusoid and square waves are generated as the actuation signals from LabView or a function generator. The actuating conditions corresponding with signals are shown in Figure 2.5. The phase angle of the square wave controls the moment that the clamp opens and releases the slider. The duty cycle of the square wave influences the open time of the clamp. Both kinds of signals must be matched well, so that the slider can move smoothly without retrogression. In the actuation process, when the clamp releases, the driving impactors must contact the slider and push it to move at the same time. Before the driving impactors move back when the negative slope of sinusoidal signal is applied, the clamp must clip the slider. Such operation can prevent the slider from moving back when the driving impactors leave the slider. Besides, an offset in the control signal of clamp (square wave) is used to prevent the slider from tilt because the clamp will not add too much force on the slider. Such signal can stabilize the slider motion when driving the motor.

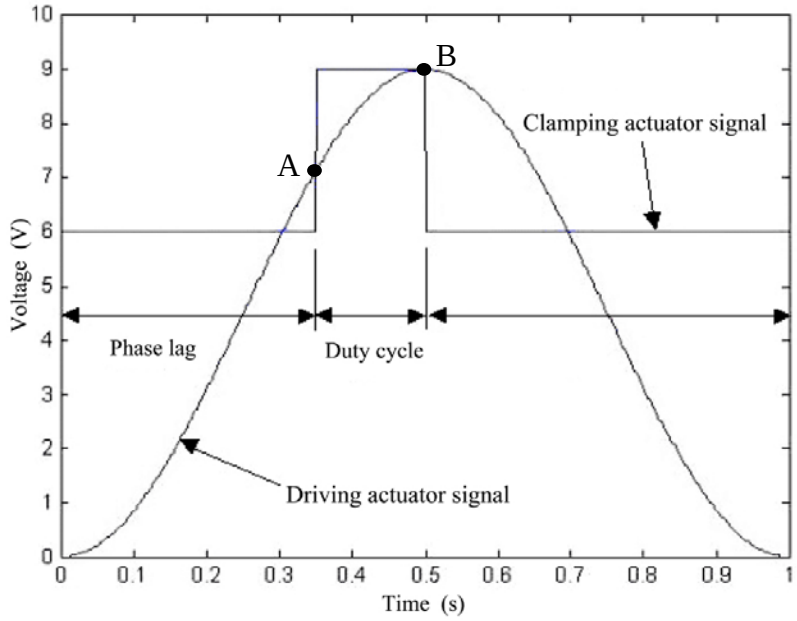

Figure 2.5: Actuation signals for the clamping and driving actuators in the stepmotor.

The operational sequence of this motor is shown in Figure 2.6. In the initial state, the clamping actuators clip the slider after its impactors leave the notches on the slider and then actuate in a small power. The first step is to actuate driving impactors to approach the slider. After the impactors touch the slider, the clamp applied more actuation power begins to release the slider. At this moment, the actuation signals are passing through the point A in Figure 2.5. The voltage on the point A is the required actuation power to let the driving actuators touch the slider, so the phase angle of the square wave can be determined from such voltage. In the next step, when the clamp leaves the slider, the friction force between the slider and the impactors displaces the slider forward. Before the driving impactors begin to leave the slider as the actuation signals are passing through point B in Figure 2.5, the clamp must return to hold the slider preventing retrogression in the slider motion. Then repeating the motion of the first step

and following the same steps as described above, the slider will move continuously in the step motion.

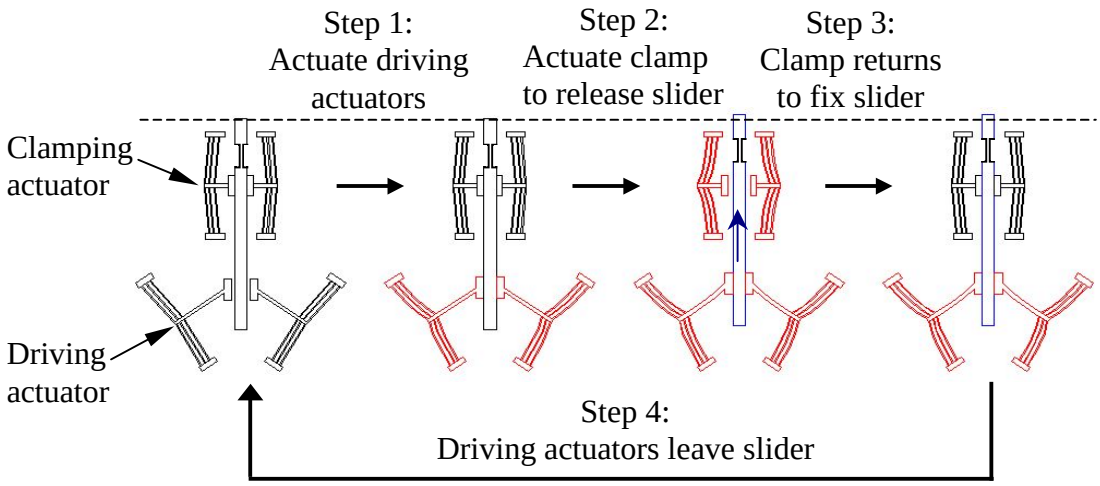

Figure 2.6: Operational sequence of the push-clamp stepmotor.

The different operational speed of slider can be obtained by changing the frequency of actuation signals. Since this linear motor is one kind of stepmotors, the motor slider does not have continuous speed. The roughly average speed can be calculated as

$$\text{Average speed} = \text{step size} \times \text{frequency}$$

Based on experimental results shown in Figure 2.7, the step size/resolution of the motor, which is the displacement per action cycle, is different between the forward and backward direction. A possible explanation for such phenomenon is that the coefficients of friction for the two moving directions are not exactly the same. A picture taken from the sidewall of the slider in Figure 2.8 demonstrates that the surface of the wall is not very smooth and likely to have some stripes on it, which may cause different coefficients of friction in the opposite moving directions. In addition, a slipping motion between the

slider and the impactor head sometimes occurs during their contact, and it causes a few losses in driving motion for some action cycles. Otherwise, the step size of the slider should keep in constant no matter how operational frequency changes.

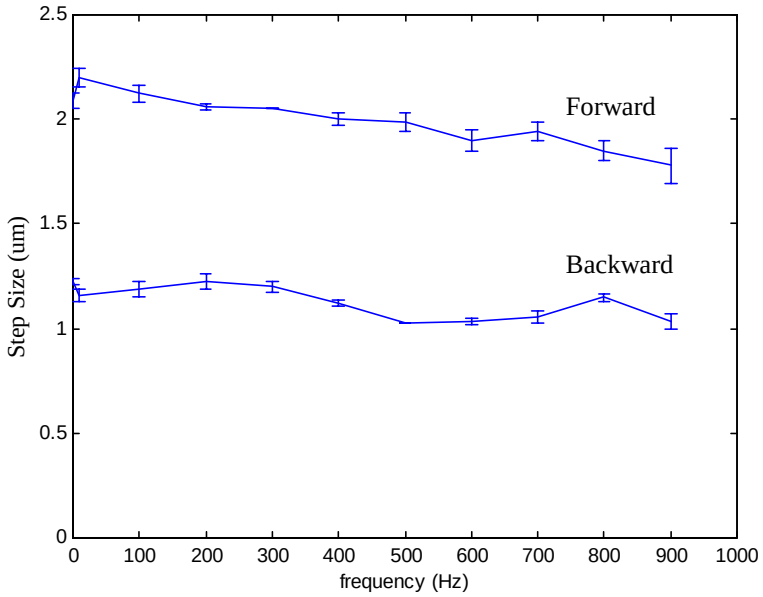

Figure 2.7: Relation between operational frequency and slider's step size as control signals are duty cycle: 10 % , phase angle: 130 deg , clamping actuator signal: 4~6 V and driving actuator signal: 0~8 V.

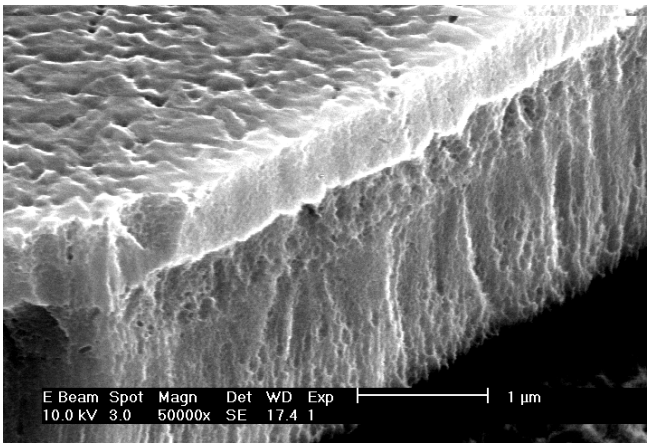

Figure 2.8: Closed view of the slider's sidewall in the push-clamp stepmotor.

In order to understand the influence of actuation signal on the clamping actuator, the phase angle and duty cycle of the square wave are changed to observe the displacement variation for each step motion. If the phase angle is fixed at 130 degrees and using the different duty cycle of the clamp signal controls the releasing time of the clamp, then the step size of slider can be remarkably altered (see Figure 2.9). According to the experimental results, a 0~10 % duty cycle as a control region is the best choice because the curve in such range is almost linear. Figure 2.10 indicates why 130 degrees as the fixed phase angle is the best for the clamp signal. In such phase angle for an actuation signal of the driving actuator, the impactor head touches the slider and produces little force on the slider, so the slider can move immediately while the clamp releasing. Selecting this phase angle is useful for the condition of having a loading at the end of slider, because this control standard makes the driving actuators prevent the slider from receding. Figure 2.11 demostrates the frequency response of this thermal linear stepmotor. The estimated cutoff frequency is about 1600 Hz and its corresponding step size is around 2 um, which means its maximum average operating speed for this linear stepmotor is about 3.2 mm/sec.

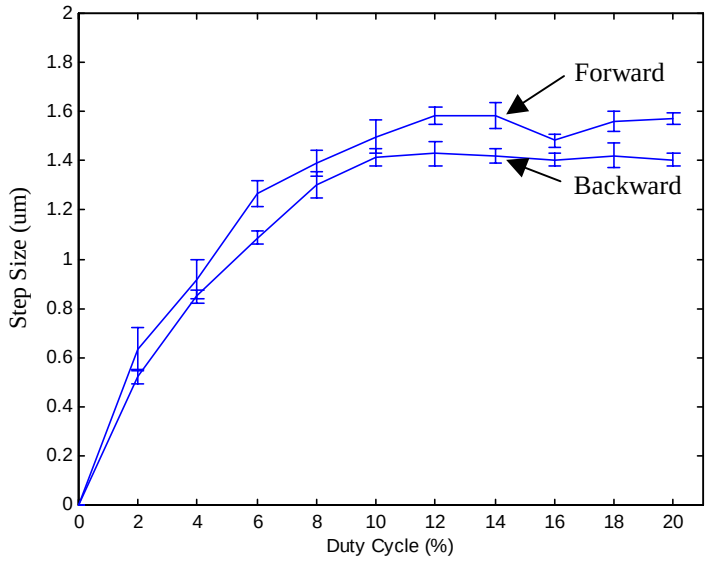

Figure 2.9: Relation of the clamp signal's duty cycle and the slider's step size as the control siganls are operational frequency: 10 Hz , phase angle: 130 deg , clamping actuator signal: 3~6 V, and driving actuator signal: 0~8 V.

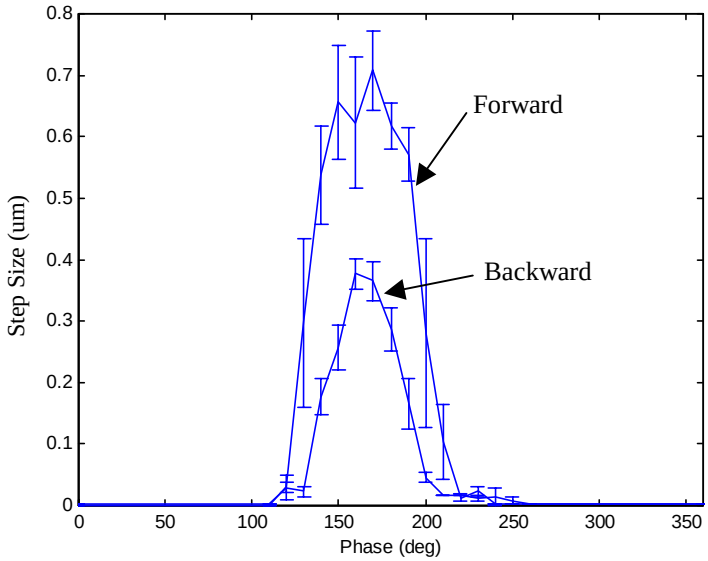

Figure 2.10: Relation of the clamp signal's phase angle and the slider's step size as the control siganls are duty cycle: 2 % , frequency: 10 Hz , clamping actuator signal: 0~6 V, and driving actuator signal: 0~8 V.

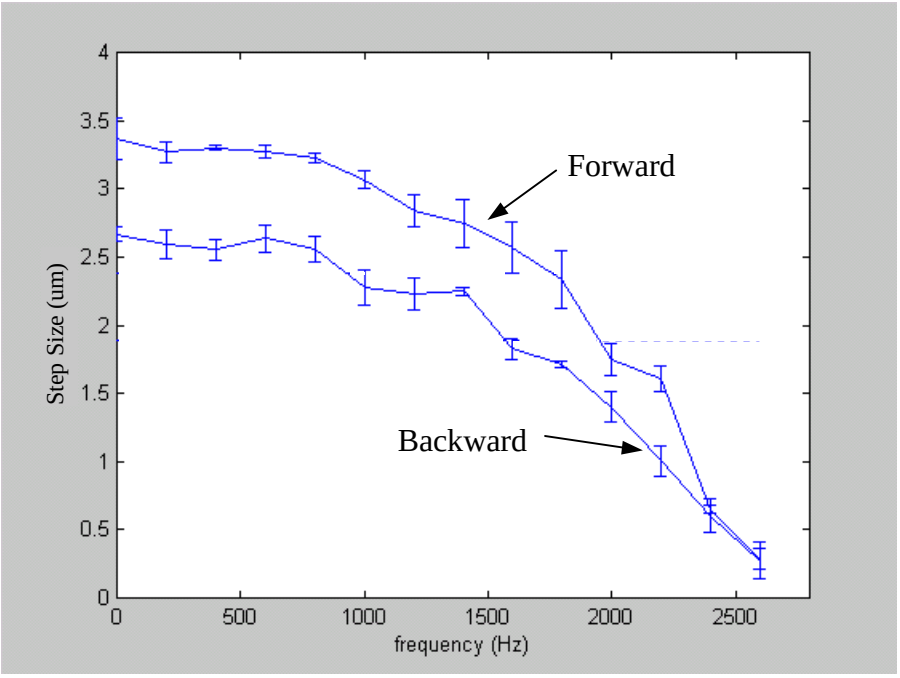

Figure 2.11: Frequency response of the push-clamp micro stepmotor.

Saw-toothed linear motor

In the saw-toothed linear motor, two pairs of thermal actuators take turns to continuously move the slider. The pair of inversely symmetric thermal actuators with wedge-type impactors vertically clamps the slider during actuation. Because two right-triangular teeth, attached on the impactor and the slider, will slip each other on the surface of tooth's tilt side, the vertical motion of thermal actuators transfers to a horizontal movement on the slider. The actuation sequence for single-direction motion of this linear motor is illustrated in Figure 2.12. First, a pair of saw-toothed impactors clamps the slider on opposite sides to balance the lateral forces and pushes the slider in one direction. Next, before this pair regresses, the second pair takes over and touches the

slider's teeth using an overlapping actuation signal to prevent retrogression caused by loading at the end of the slider. Such cycle is repeated to accomplish continuous movement of the slider. Because the frequency response is fast from the previous experiment on the push-clamp stepmotor, the square wave is used as the actuation signal to fit the fast response due to the settling time in creating actuation signals. The duty cycle of this square wave should be greater than 50% to enable two sets of signals from actuators to overlap at their high peaks between two neighboring dot lines, as shown in left hand side of Figure 2.12. Furthermore, the phase angle of the square wave controls the moment of overlap. Both constituent factors of actuation signals, duty cycles and phase angles, are crucial in terms of determining the smoothness of the slider motion.

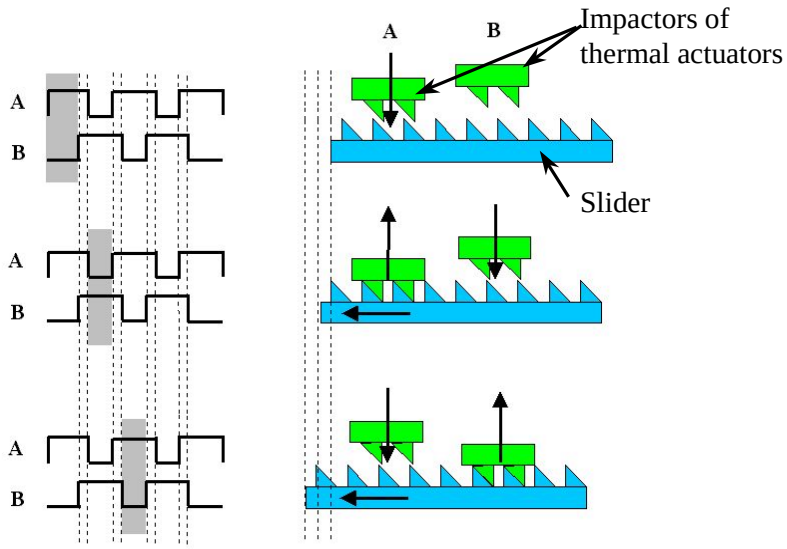

Figure 2.12: Signal sequence (left) and movement (right) of the saw-toothed linear motor.

2.1.4 Discussion

Although the push-clamp stepmotor has good performance on actuating after testing, its unpredictable slipping between the slider and the impactor results in some displacement deviations for each step's movement, even when the duty cycle and phase angle of the clamp signal are fixed. Such disadvantage weakens its potential to become an actuation motor with accurate position control. In addition, the motion of the slider in this stepmotor has a short moment of pause when the clamp clips the slider, so its motion is not entirely continuous, and thus causes some vibration on the slider. However, its advantages include less bond pads, less complexity in actuation, and small occupied areas comparing to the saw-toothed linear motor. According to the above discussion, the slipping between the impactor and the slider is not desirable in this motor, so a large coefficient of friction can reduce the possibility of slipping. Unfortunately, after a long time of collision between the impactor and the slider, the wear may cause the contact surface smoother and as a consequence decrease the coefficient of friction. Then the driving actuator may never push the slider forward in a condition of deficient friction.

On the contrary, a new design of the saw-toothed linear motor produces the smooth and completely continuous motion on the slider, in other words, it will greatly reduce vibration during actuation. Moreover, the yoke of the thermal actuator is rigid and perpendicular to the slider in this kind of linear motor. Unlike the yoke of the driving actuator in the stepmotor is flexible and angled on the slider. Hence the yoke in the saw-toothed linear motor does not bend and change the shape. Such advantage provides more force on the slider without losing force on bending the yoke. Furthermore, this rigid yoke also greatly simplifies the force analysis between the impactor and the slider without

considering the elastic deformation on the yoke. In addition, the resolution of this motor can be infinitesimal because the displacement of the slider is only related to the displacement of the thermal actuator that depends on the amplitude resolution of the power supply. All of these benefits provide a simple open-loop control method for this motor and meanwhile keep its position accurancy in the movement of the slider. Moreover, in this motor, the slipping between the two teeth on the impactor and the slider is essential. Fortunately, the slipping surface becomes smoother after wearing over a period of time and therefore the vibration caused by gliding on the rough surface is reduced. The stability of actuating motion is enhanced accordingly. Thus this motor also extends the duration life due to performance improvement without damage after wearing. Comparing to the push-clamp stepmotor, this motor includes some disadvantages such as more bond pads, more complex actuation procedure, and larger occupied areas.

2.2 UV-LIGA Fabrication

UV-LIGA fabrication process is another suitable method to create multi-layered structures. This process uses UV light to replace the x-ray in LIGA process and still makes high aspect ratio nickel structures. Electroplating is a necessary step to deposit the structure in this fabrication process. Nickel sulfamate is selected as an electroplating bath to increase the quality of plating metal due to its benefits discussed below. Two different photoresists used UV light to form high aspect ratio structure are also discussed.

2.2.1 Electroplating Process

In the past 50 years, nickel sulfamate solutions have been extensively used in electroplating applications. Low residual stress, high deposition rates and good ductility are made those baths attractive. Besides, such solution has a relatively low sensitivity to contaminants such as metallic and organic impurities. Nickel is also the most effective electroplated coating identified for extended periods of exposure to corrosive environments. All of those advantages make nickel sulfamate baths an ideal selection to electroplate nickel as the structures of linear micromotors and micromechanisms.

The properties and behavior of electrodeposited nickel from a sulfamate solution are determined by many variables, including operating conditions, impurities in plating solutions composition, additives and others. Changes in solution composition, operating temperature, current density, solution agitation, current form can alter minor or remarkable deposit characteristics such as hardness, internal stress and crystalline structure[61]. The impurities in nickel deposits such as sulfur, chloride, hydrogen, oxygen, and carbon adversely affect physical properties with increasing concentration. Mechanical properties such as tensile strength and ductility are also affected by impurities, especially carbon and sulfur. Those impurities are influenced by the current density and changes of solution composition, temperature, and agitation [73]. The variables of affecting stress may also influence mechanical properties. That means if the internal stress is controlled in a certain range, the properties of deposit may also be restricted within the constant values. The followings are the discussions of changing deposit properties according to the bath ingredients and the operating conditions.

Bath ingredients

The anode used in sulfamate baths typically comprises nickel and a low amount of sulfur (0.02%) which is used to promote nickel dissolution in the bath. This is because an insoluble anode will increase the stress via potential rise, resulting in hydrolysis of the solution to obtain SO_4^{2-} and NH_4^+, both of which increase stress [67]. In addition, it should be the sulfur-depolarized type if a minimum of chloride is required. Using the wrong anode, exhibiting a higher oxidation potential, could lead to decomposition of the sulfamate. In turn, this would generate the formation of a divalent sulfur product which could co-deposit causing brittleness[61].

Nickel sulfamate is the source of the nickel deposits. Concentrations of 90 to 135 g/L of nickel metal are the most cases for using high-speed plating with very high solution agitation. At very low current density of 10 to 40 A/m^2, high Ni metal content is useful to improve the throwing power to avoid co-deposition of basic nickel salts, and it does not appreciably change the characteristics or properties of the deposit. Low metal content reacted with moderate to high current densities will cause “burning” nickel on deposition [61]. Furthermore, Kendrick [68] indicated that control of stress and properties was possible in a high nickel content bath. The concentration of boric acid should vary with the operating temperature from 30 g/L at 20 ^oC to over 45 g/L at 52 ^oC. Low boric acid causes “orange peel” type of pitting, but high boric acid will tend to separate salt from the solution at lower temperatures. Besides, Lower nickel contents (below 75 g/L) require higher amounts of boric acid. Chlorides or bromides are used in small amount to promote optimum on anode corrosion, because poor anode corrosion incurs compressive stress, brightness, loss of ductility, increased hardness and porosity. However, the

addition of small amounts of chlorides slightly increases the tensile stress of the deposit [61].

The brightener additions into the plating bath affect the ductility of the deposit and its internal stress. Some organic additives such as saccharin induce a compressive stress to avoid the undesirable high tensile stress. Primary brighteners cause compressive stress, loss of ductility and heat resistance. Secondary brighteners cause tensile stress and loss of ductility. Compounding these two types to balance conditions is possible to nearly achieve zero stress. However, the deposits will be more brittle much like that from bright Watts solutions [61]. Oxides and hydrated nickel compounds sometimes occlude in nickel deposited at high current densities in high pH solutions. These impurities must be minimized, otherwise they will decompose to form gas at high temperatures and reduce the ductility and strength [73]. The more details about bath influences in metallic and non-metallic impurities can refer to Mandich et al. [61] and Safranek [73].

Operation conditions

High current densities and/or low temperatures can cause “burning” phenomenon because basic nickel salts deposit. The stress may fluctuate from compressive to tensile, and the properties and characteristics of the deposit are also affected by current density [64]. However, in sulfate/chloride baths, stress increases at an even rate as the current density is increased. Within the normal operation limits, current density and temperature have little effect on the hardness and the structure of deposits [61]. Above pH 5.0, hardness and stress increase but ductility decreases because of the co-deposition of basic nickel salts, whereas, low pH results in faster accumulation of impurities. A pH below 3.5

reduces the cathode efficiency and slightly decreases the plating rate, but it does not change the deposit hardness. The internal stress reaches a minimum at pH 4.0 to 4.2. The influence of temperature on hardness is a parabolic function. The hardness increases more rapidly at lower temperatures. It is not appreciably affected between 35 and 50^{o}C. High temperature can cause sulfamate decomposition with consequent increase in the stress. Ductility decreases rapidly with increasing temperature. A temperature of 71^{o}C must not be exceeded and the best temperature range is from 54 to 60 ^{o}C [61].

Practical operation and electroplating results

Before performing the nickel electroplating process, the plating bath is treated to remove inorganic contaminants by the "plating out" technique. This technique uses a dummy cathode (total size about 25 cm^{2}) to do electroplating for 3 hrs, so that other metal ions, which are more electrochemically active than nickel, can be removed from the solution. During the plating process, the cathode current density is always at less two times larger than the anode current density. This is to ensure the anode can quickly supply ions into the solution, especially if the solubility of anode is poor. Furthermore, in order to keep the homogeneous plating bath at the desired operation temperature, a magnetic stirrer is used at the bottom of plating tank to provide sufficient circulation. To avoid overheating at the certain spots, a hot plate also replaces a general heater to heat up the bath under the plating tank.

The planarization of the structures, which can be controlled by the internal or residual stress of the deposited material, is very important, especially for a micro movable lump. The positive internal stress (tensile stress) causes a concave shape of bar

after releasing, but the negative internal stress (compressive stress) induces a convex shape. Thus the zero or near zero internal stress is perfect to maintain the flat micromanipulator fabricated by electroplating process after releasing. On the other hand, the overall leveling of electroplating deposits is also a main issue in the electrodeposition process. The localized electrodeposition rate is proportional to the regional current density. After the wafer is patterned with photoresist, some portions of the wafer are open to the plating bath and others are covered by the insulating photoresist. As shown in Figure 2.13, the uniform current density is homogeneously distributed on the whole wafer before pattern. However, after pattern the lines of current are twisted to the conductive (open) areas only, so that the current density is higher on the edges of the open area. Moreover, the current density in a narrow conductive area is also higher than the broad zone. Because the area of higher current density is deposited metal faster than the region of lower current density, those non-uniform current densities result in poor leveling with a concave shape above the deposit in each open plating mold. To minimize the curvature of the concave leveling, using a lower current density during electroplating can remarkably improve this situation because it reduces the discrepancies between different zones which hold varied current densities.

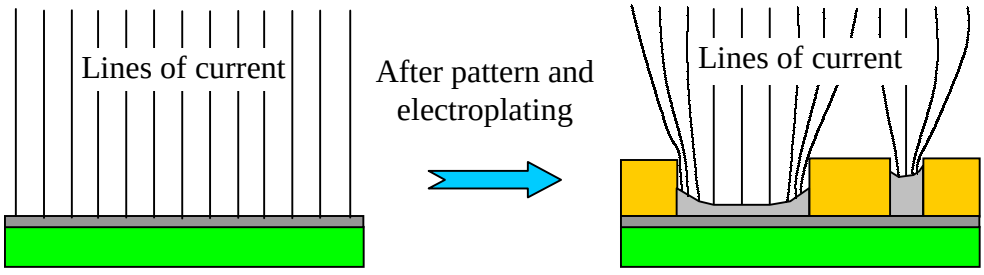

Figure 2.13: Illustration of the current density change after pattern.

It is necessary to measure the deposit stress in evaluating the performance of the electroplating bath to obtain the optimal operation conditions for the bath that provides the minimum internal stress inside the deposited metal. Two basic methods, the spiral contractometer method and the rigid strip method, are most widely used to achieve the stress measurement among several ways. The spiral contractometer is a reliable method to determine intrinsic stress. This technique can detect small stress changes from a magnifying helix through some gears. Such good sensitivity is very helpful when the plating bath is operated near or at zero internal stress. The rigid strip method is simple and sensitive enough for most industrial applications. This technique uses disposable two-legged brass strips, which are opened on opposite sides to ready deposit, to measure the radius of curvature on a single strip caused by deposit stress. The deflection or curvature is measured from a simple scale, as shown in Figure 2.14, and then transferred into the corresponding stress using the simple formula. The formula from the manufacturer of this deposit stress analyzer, Specialty Testing & Development CO., is

$$S_d = \frac{UK_s}{3T_d} \tag{2.1}$$

where S_d is the deposit stress in pounds per square inch (psi), U is the number of scales from the stress analyzer, K_s is the strip calibration constant from the manufacturer, and T_d is the deposit thickness in inches. If the deposit thickness cannot be determined by the actual measurement, it can be estimated by total weight of deposit on the strip. Since the plated surface area on the standard test strip is always fixed in 7.74 cm^2, the deposit thickness can be calculated as

$$T_d = 0.0509 \frac{W}{D} \tag{2.2}$$

where W is the deposit weight in grams and D is the density of the deposited metal in grams per cubic centimeter.

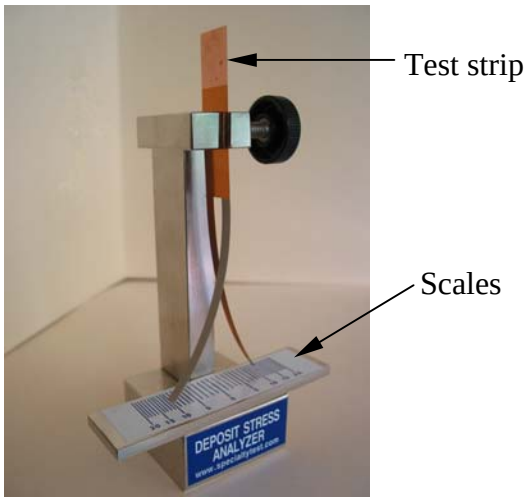

Figure 2.14: Deposit stress analyzer for the rigid strip method.

Figure 2.15 displays the several relations between the deposit stress measuring from rigid strip method and the temperature of plating bath on different plating conditions of varying current densities. According to the experimental results, different current densities possess unique performance curves. In low current density of 50 A/m^2, the deposit stress is fluctuated in different bath temperatures, and the curve of stress becomes a valley shape when the current density is increased to a moderate level of 200 A/m^2. However, the deposit stress drops exponentially when the temperature is raised in the higher current density of 350 A/m^2. Therefore, it is very complex to define which temperature is the best to produce the minimum deposit stress.

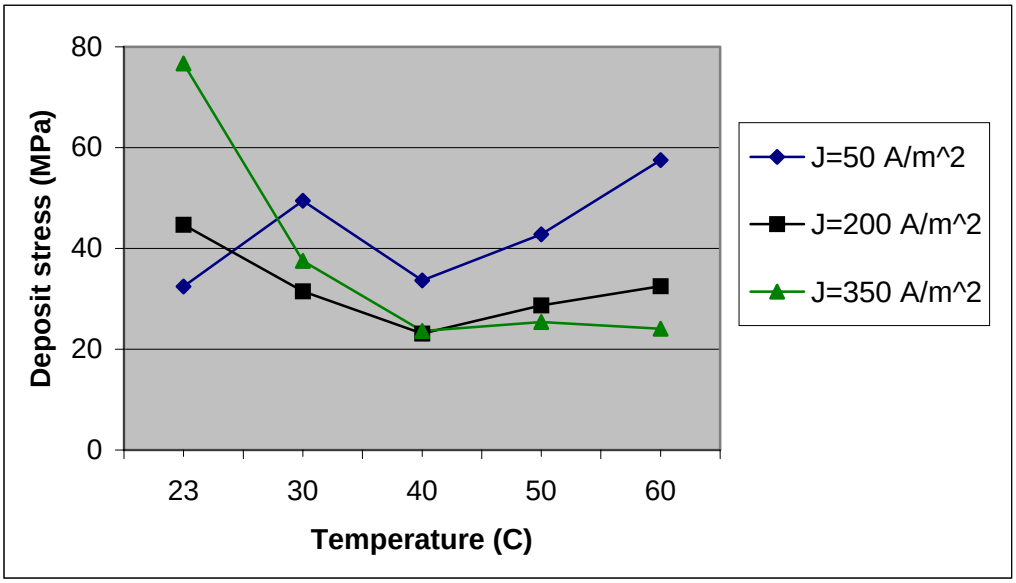

Figure 2.15: Bath temperature Vs. Deposit stress on different current densities.

Actually, low temperature bath is more suitable to deposit Ni metal as the structures in this research, because high temperature bath changes the dimension of the deposited structure due to swell and reflow of the photoresist mold in high temperature. Furthermore, based on the above discussions about electroplating baths, the near zero deposit stress and good leveling of the deposited structures require a low current density and high metal content in the electroplating process. Therefore, the low temperature bath and the low current density are the best selections to obtain good shape of deposited structures. However, because of higher gas content (hydrogen) inside the deposits, the overall surface of deposit is not smooth at very low temperature such as room temperature at 23 ^{o}C. Thus, according to experimental results in Figure 2.15, the temperature of 40 ^{o}C can also obtain the lowest deposit stress in the low current density of 50 A/m^2. In addition, using a low current density results in much higher sulfur content [65] which correlates with the higher compressive stress in deposits [64], so it may

compensate the tensile stress of the deposits close or at zero in most deposit conditions. Table 2.1 is the list of the compositions of electroplating bath and its plating conditions to produce the minimum deposit stress and good leveling on the top surface of deposit. The mechanical agitation type of nickel sulfamate solution in an electroplating bath is directly from Technic, Inc.

Table 2.1: Compositions of the plating solution and the plating conditions.

Nickel sulfamate $Ni(NH_2.SO_3)_2$	320 g/L
Nickel, as metal	77 g/L
Nickel bromide $NiBr_2$	45 g/L
Boric acid H_3BO_3	30 g/L
pH value	4.0 - 4.2
Bath temperature	40 ^oC
Cathode current density	50 A/m^2

Using the electroplating bath described in Table 2.1, the relation between the growth (deposit) rate and the current density is shown in Figure 2.16. The growth rate is proportional to the deposited current density, and it is used to estimate the deposit time to obtain the desired deposit thickness. Figure 2.17 displays the relationship between the deposit thickness and its residual stress. In the range of the fabrication thickness from 2 um to 25 um, the thicker deposit generates less residual stress. This character is helpful to maintain the planarization of the electroplating structure after releasing.

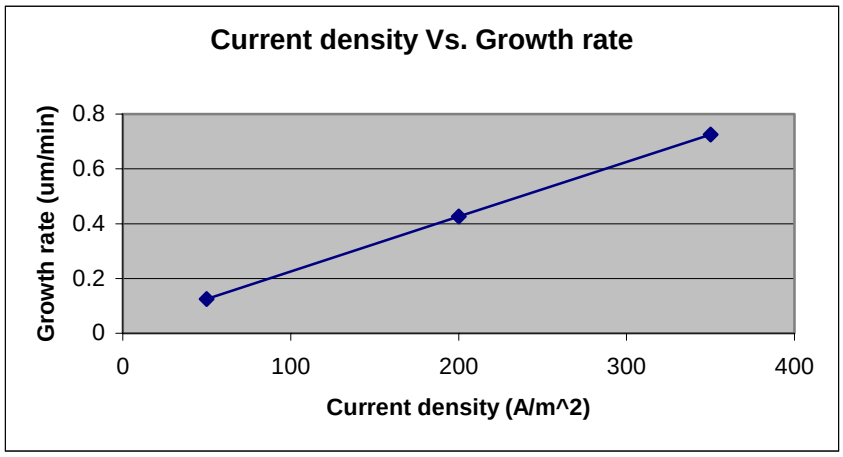

Figure 2.16: Growth rate versus current density in the nickel sulfamate bath.

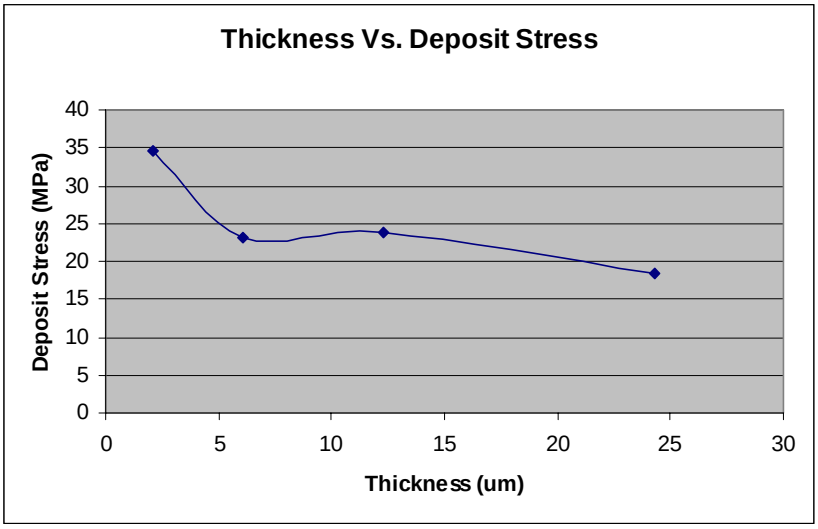

Figure 2.17: Deposit thickness versus deposit stress in the nickel sulfamate bath.

2.2.2 Surface Micromachined Using SU8 and Electroplating

SU-8 is a negative, epoxy-type, near-UV photoresist based on EPON SU-8 epoxy resin. It has been initially developed and patented by IBM and is commercially available from MicroChem Corp. This photoresist with many advantages due to its low optical

absorption in the UV range has been broadly used in many MEMS applications. Its remarkable benefit is easy to obtain high aspect ratio structure with low cost. The ratio can achieve up to 20 in the good process and its maximum thickness can reach 2 mm. A perfect vertical wall, which is often acquired after developing, is another important feature comparing to other photoresists. Moreover, this photoresist is also applicable to bioindustry due to its no toxicity and biocompatibility. However, the drawbacks of SU8 are that the highly crosslinked epoxy remaining after development is difficult to remove without damaging the electroplated metal and its shrinkage rate can reach as high as 7.5% after post bake.

Because the thicker thermal beams provide more force, SU8 photoresist is very suitable to be the complementary mold to fabricate a powerful thermal actuator after electroplating. In the past research, two layers of structures formed a meso-scale linear motor. The structures in the first layer make anchors for suspending thermal actuators. The second layer creates the main structures of the linear motor that contain the slider and the thermal actuators as shown in Figure 2.18. Unfortunately, after using Nanostrip to remove crosslinked SU8, some nickel structures of this linear motor are disappeared or separated from the Si/SiO_2 wafer because Nanostrip also attacks Cu, used as a seed layer for electroplating, and moderately hurts nickel causing damage or disappearance on most small size structures. Dynasolve 185 is another chemical to remove crosslinked SU8 without damaging any metal by simply heating up to 60^oC. However, this solution only peels off crosslinked SU8, not dissolves it, so some suspended beams cannot be completely released because the residual crosslinked epoxy still stay beneath the beams

without elimination. Therefore, utilizing SU8 as sacrificial layers is not feasible to make a suspended structure.

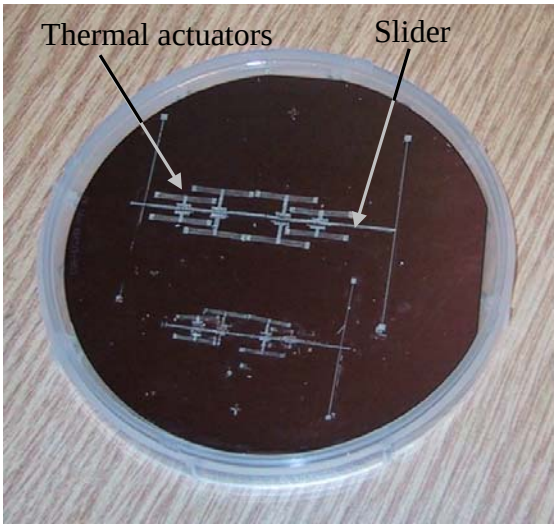

Figure 2.18: Product of a meso linear motor with thermal actuators on a 4-inch wafer using SU8 as sacrificial layers.

The whole manufacturing process using SU8 is shown in Figure 2.19. This multi-layered fabrication process is based on the conventional plating-through-mask technology. The first step is using sputter to deposit Ti 300Å and Cu 3000Å on the Si/SiO_2 wafer as a seed layer, and then using a spinner to coat SU8 on this wafer. A 2 um-thick SiO_2 on the wafer is used as an electrical insulated layer. After SU8 is solidify by a soft bake process in the oven or the hotplate, the wafer is put on Karl Suss MA6 to do lithography under UV light. Then the post exposure bake in the oven follows to increase the crosslink speed of the exposed SU8. The pattern or electroplating mold of the first layer is formed after the whole wafer is immersed in the SU8 developer to do development. The next step is using nickel sulfamate bath to deposit the first layer's

structure. After the previous electroplating process, the wafer is polished by abrasive on polish cloth to flat the all levels of nickel structures and the photoresist mold. Then a 5000Å-thick Cu is sputtered on the whole wafer to be another seed layer for the second layer structure. Similarly, the wafer coming from the previous step is spun SU8 and patterned again to obtain the electroplating mold for the second layer structure. The same electroplating bath is used to deposit nickel to acquire the second layer structure. In the final step, Nanostrip is used to remove the SU8 mold and Ti/Cu etchant is used to eliminate exposed seed layers.

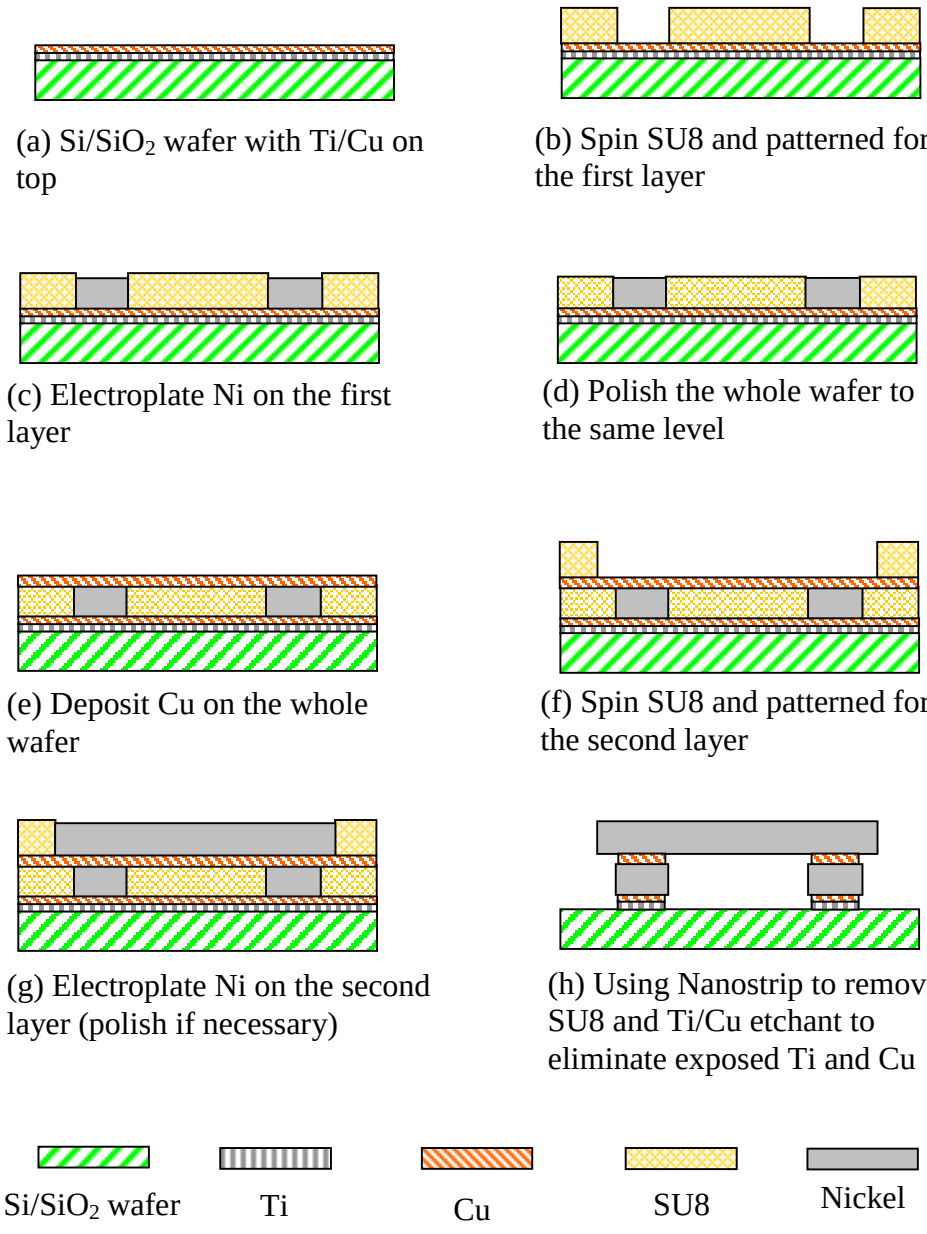

Figure 2.19: Whole procedure of a multi-layered thermal actuator fabrication using SU8 and the electroplating method.

2.2.3 Surface Micromachined Using AZ9245 and Electroplating

Since crosslinked SU8 is difficult to remove, another photoresist has to replace it as a sacrificial layer. Clariant's AZ9245 is very easy to remove and its coated thickness can also achieve thick enough to be the electroplating mold. The manufacturing process of two-layered structure is very similar to the above fabrication process using SU8 and presents in Figure 2.20. The first step is to prepare a 4" silicon wafer with 2 μm-thick silicon oxide on its top as a substrate. The oxide layer is used as an electrical insulated layer. Then 300Å-thick Ti and 3000Å-thick Cu deposit on the wafer as an electroplating base or a seed layer. Titanium is used to increase adhesion between copper and silicon oxide. The successive step is to spin the AZ9245 on the wafer and pattern the first layer structure. When spinning the photoresist, the multiple coating sometimes is necessary to increase the thickness of photoresist. If this situation happens, the wafer needs to bake in the oven or hotplate to solidify the first coating photoresist before spinning the next one. The next process is to immerse the whole wafer into an electroplating bath to deposit nickel as the structure. After electroplating, the level of the plating nickel is not very flat, thus CMP (chemical mechanical polishing) method is applied to level the whole surface of the wafer. The succeeding step is to deposit 5000Å-thick Cu on the whole wafer as a seed layer for the second layer structure. The subsequent steps for the second layer structure are the same as previous ones. The final step is to remove the sacrificial layer, AZ9245, and some portions of seed layers. Acetone is a very good solvent for AZ9245 and it does not harm any metal. Eliminating uncovered adhesion layer between copper and silicon oxide with Ti etchant will complete the whole releasing process. In order to

prevent large, compliant structures from sticking to the substrate, a supercritical CO_2 drying step is better to perform after the whole wafer finishes the wet release process.

Using above conventional plating-through-mask technology in the multi-layered fabrication process, thermal stability of the lower photoresist layer dominates the structural quality of the above layer because the thermal reflow of the lower photoresist layer always happens during the high temperature cycles in the above layer's metal deposition and photoresist baking [9]. To solve this problem, relative low temperature of 60^oC is used to soft bake the coating photoresist while making any layer of structure above two and the temperature of electroplating bath is also always kept in 40^oC. After electroplating and polish processes, the hard bake step in 60^oC for a long time is necessary to evaporate all residual solvent within the photoresist mold to prevent bulging of the seed layer before depositing Cu for the next layer. The multi-layered structure simply follows the same fabrication processes on each layer, including pattern, electroplating, and polish, to accumulate layer by layer until the required number of layers.

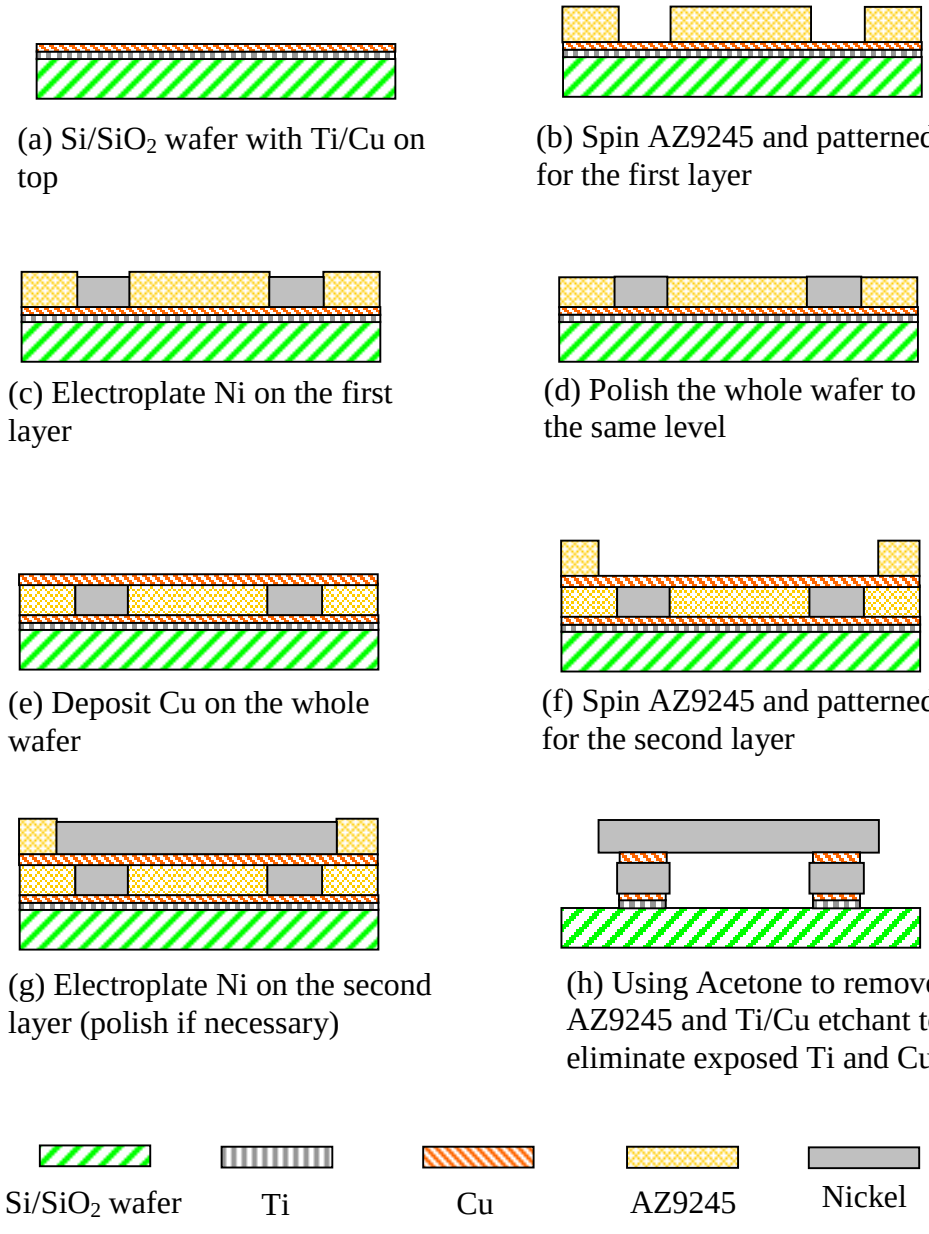

Figure 2.20: Whole procedure of a multi-layered thermal actuator fabrication using AZ9245 and the electroplating method.

During the structure release process, a short copper etching is performed to remove the thin seed layer. Two different kinds of Cu etchant, 15% dilute nitric acid and ammonium hydroxide, had tried in this research, and the surface conditions of the nickel structures after using them are shown in Figure 2.21. According to experimental results, the etching rate of Cu in the dilute nitric acid is much higher than that in ammonium hydroxide, but the etching strength of dilute nitric acid slightly attacks nickel to produce many small etching holes on the surface of structures. The right hand side of Figure 2.21 demonstrates good surface conditions of the nickel structure after etching Cu with the mixed solution of NH_4OH: H_2O_2 = 50: 1. A small amount of hydrogen peroxide is used to increase the etching rate of Cu without damaging nickel. In the whole releasing process, the nickel structure is only scarcely harmed by Ti etchant TFT from Transene Company during etching the Ti film. Therefore, using Acetone as a remover of sacrificial layers and the mixed solution of NH_4OH: H_2O_2 = 50: 1 as a copper etchant, the device of nickel structure after releasing still keeps in a good shape and brightness. The two-layered structure of a linear motor shown in Figure 2.22 has been successfully fabricated by this manufacturing technology. This linear motor includes four pairs of thermal actuators and two folded support beams on the both sides of the slider. The supported beams are used to suspend the slider after releasing, so that the slider can move on straight direction paralleled on the top surface of the wafer and settle above the wafer during no motion.

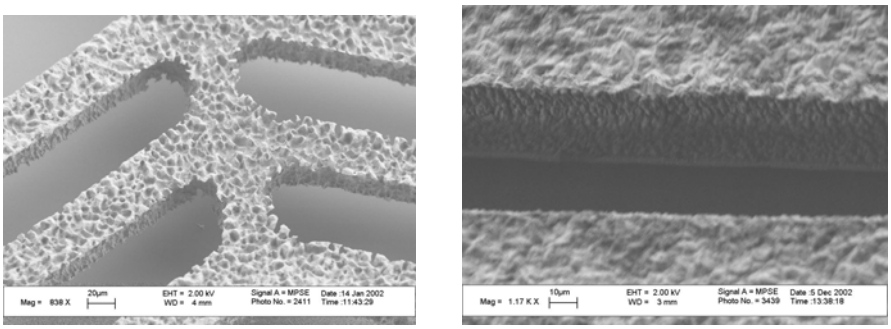

Figure 2.21: Surface conditions of the nickel structures after using different copper etchants. The left picture displays the result using 15% dilute nitric acid and the right using the mixed solution of NH_4OH : H_2O_2 = 50 : 1.

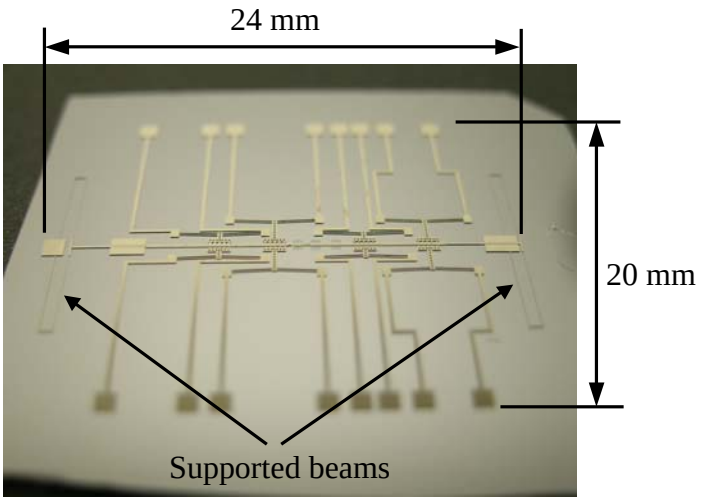

Figure 2.22: Linear motor fabricated by UV-LIGA process.

An easier fabrication procedure illustrated in Figure 2.23 makes the two-layered structure with merely doing the electroplating process once. In this method, the 2-μm thick silicon oxide layer on the wafer becomes another sacrificial layer and electrical insulation material, so one-layered structure can form the suspended structure. Figure 2.24 displays some structures of thermal actuators and linear motors through this process on a 4-inch wafer.

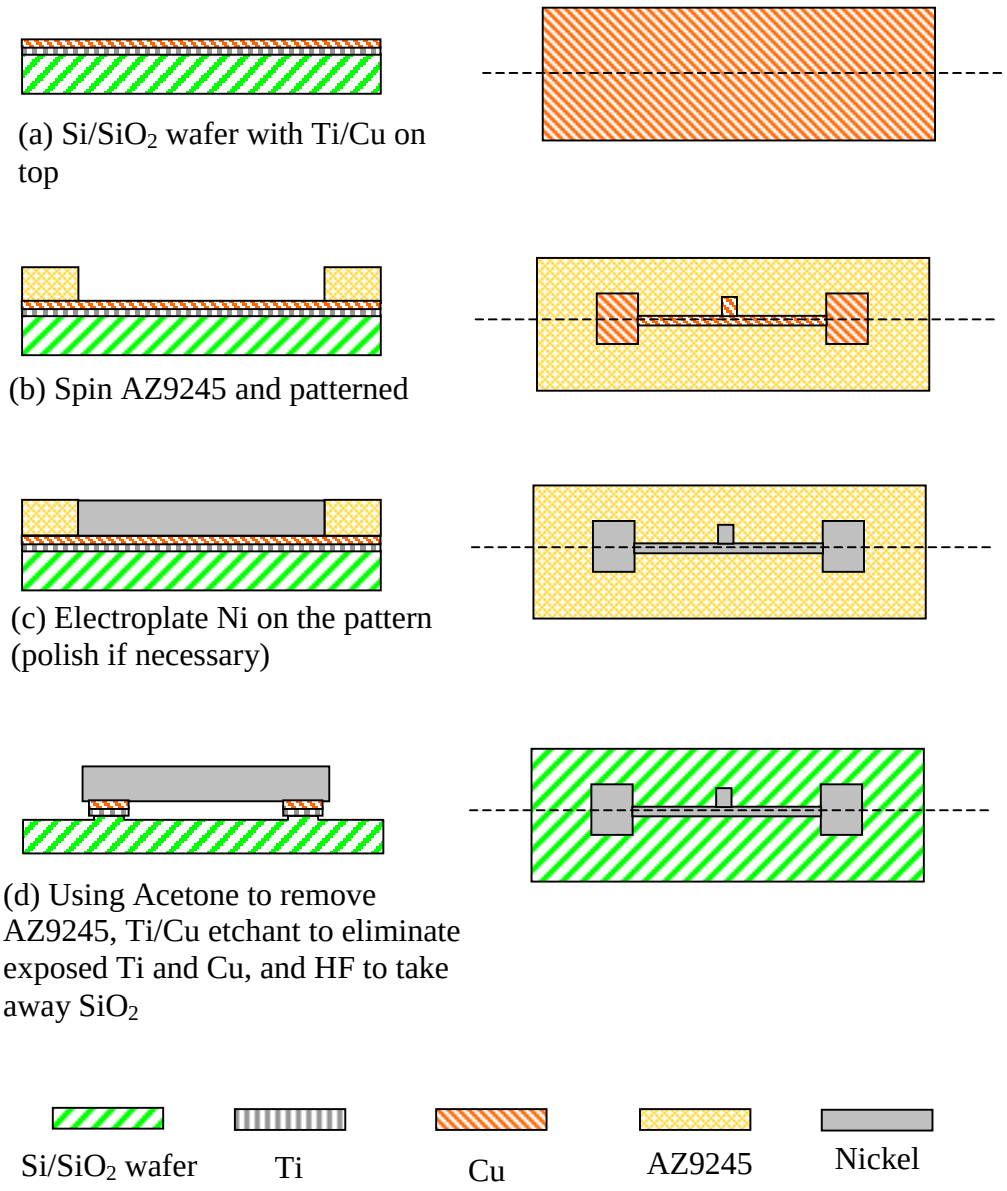

Figure 2.23: Whole fabrication procedure of a thermal actuator using AZ9245 and the electroplating method with one-layered structure method.

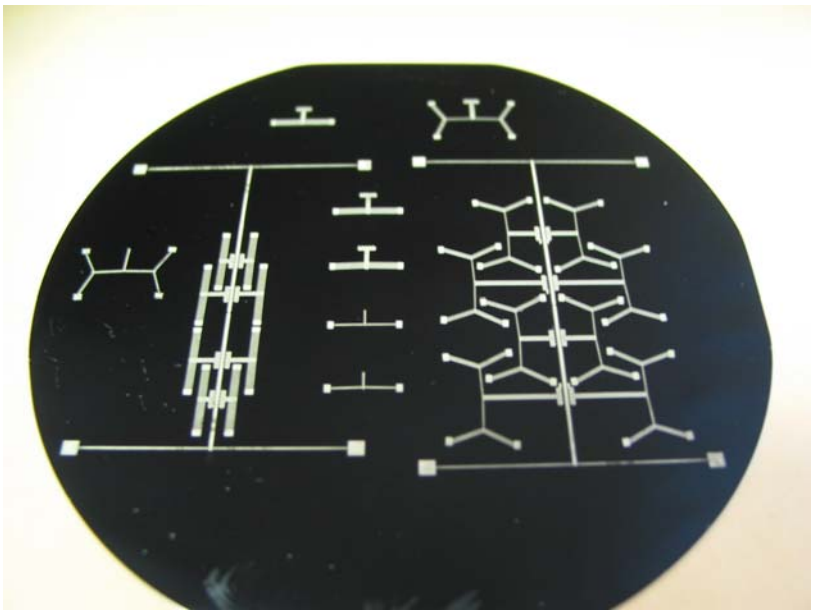

Figure 2.24: Thermal linear motors on a 4” wafer using UV-LIGA process with one-layered structure method.

2.2.4 Discussion

In electroplating process, some additives such as brightener can improve the overall leveling of the nickel deposit. However, the amount of additives is difficult to control, so the leveling is still not flat enough to satisfy the requirement in the fabrication process. Periodically Reverse Electroplating (PRE) or Pulse Periodic Reverse (PPR) method, which is periodically exchanged the polarity between cathode and anode to alter the direction of current during electroplating, had been tried to enhance the leveling of the deposit in this research. When the direction of the electrical current is reversed, the original accumulated nickel on the wafer will be removed back to the nickel electrode. For the area of higher current density with a bigger electrodepositing rate, the removing rate of this area also gets faster after the electrode is interchanged. The control factors of

this method are the duration time and the magnitude of the reverse current. Therefore, the deposit metal is alternatively deposited and removed in different rates, which reduces the discrepancy of deposit levels located on different areas. However, after testing this method, the “burning” nickel with higher deposit stress is deposited on the wafer due to severe current change.

Polish process is used to planarize the surface during fabrication of multi-layered structure. The experiment proves that this process may increase a little stress gradient on the structure. Using microscope focus method to measure the tip deflection of the long cantilever beam can calculate the stress gradient as [69]

$$\frac{d\sigma}{dt_f} = \frac{E}{1-\nu}\frac{2}{L_c^{\,2}}\delta \tag{2.3}$$

where σ is the internal stress of the film, t_f is the film thickness, E is the elastic modulus of material, ν is Poisson’s ratio, L_c is the length of the cantilever beam, and δ is the tip deflection of the cantilever beam. The stress gradient of nickel film from the electroplating process changes from 1.91 MPa/um to 2.82 MPa/um after polishing. Therefore, the polish process needs to carefully treat in the Ni films to avoid significant stress gradients which could lead to unwanted curvature of the released elements.

The high-aspect-ratio structure is the most challenging process in fabrication of multi-layered structure using UV-LIGA method. Although SU8 can easily make a high aspect ratio of plating mold with extremely vertical sidewalls shown in Figure 2.25, the difficulty of removal becomes a mortal disadvantage for this photoresist acting as a sacrificial layer and an electroplating mold. In contrast, AZ9245 is a good choice because nothing remains after removal. However, it is very difficult to obtain vertical sidewalls in the electroplating mold after development without special treatment. Figure 2.26 shows

the cross section of the nickel structure after using PDMS molding. Based on this figure, the upper surface of the Ni structure is larger than the bottom. This is because when the developer, AZ 400K 1:4, dissolves the exposed photoresist in the development process, it also slightly attacks unexposed photoresist if the whole wafer is immersed in the developer to form the electroplating mold. Therefore, the groove of the mold becomes trapezoid shape with a wider open on top, especially for the high aspect ratio channel due to longer development on top. However, using spray developer and spinning the wafer to do development can improve this imperfect shape of sidewall.

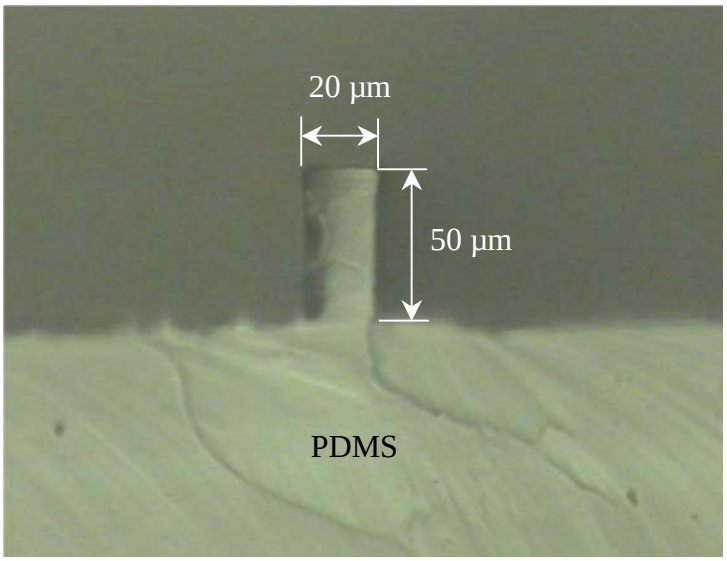

Figure 2.25: Cross-section of SU8 mold after using PDMS molding.

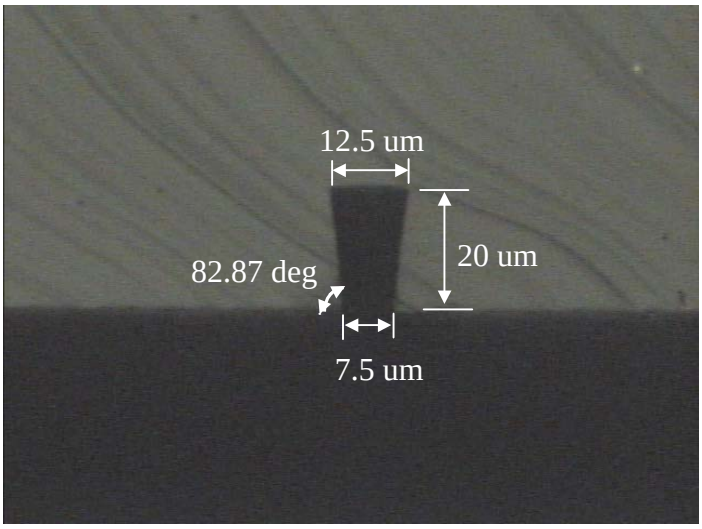

Figure 2.26: Cross-section of a nickel beam using AZ9245 as an electroplating mold.

On the other hand, the structure obtained from the two-layered fabrication process is observed the smaller internal stress than that from the one-layered process. The possible reason is that the cross-linked AZ photoresistor slightly self-deforms so as to release the little deposit stress during Ni electroplating [62]. Although annealing process can further decrease the internal stress, the thermal V-beams permanently deform in the high temperature annealing process due to over stretch. Thus the annealing process is not feasible for reducing stress in my designed devices. Using one relatively soft sacrificial layer under a long suspended beam to do fabrication is very useful to obtain low internal stress structures without through anneal process to release its internal stress, and this inherent low stress will keep long suspended or free beams horizontally.

During releasing the device, the layer separation is the most serious problem due to poor adhesion between each layer of structures. The reason is that the select Cu etchant also slightly etches the Cu film under the nickel structure through capillary attraction

during removing the exposed Cu film. This slight under-cutting affects the adhesion between each layer's structures, and it also happens in the final releasing process on removing exposed Ti film. To solve this problem, using dilute etchant can improve the adhesion and decrease the possibility of under-cutting in the adhesion layer. In one-layered structure fabrication method, HF is used to remove SiO_2 to release the structure, but it also attacks Ti at high etching rate producing under-cutting through capillary attraction. To prevent the separation between structures and the wafer, enlarging the anchors of the structures or using Cr to replace Ti as an adhesion layer is a good way to obtain successful devices. To sum up, extremely dealing with the releasing process is crucial in the whole fabrication process.

2.3 Summary

The MUMPs silicon process restricts the structure thickness of each layer and the number of the layer, so that some designs of devices or mechanisms cannot fit this fabrication method. Contrarily, the thickness of each layer and the number of the structure layer are both flexible in the UV-LIGA fabrication process. Because of the limitations of MUMPs process, UV-LIGA process will be selected as the fabrication process to make my designed micromanipulator in the next chapter. In addition, an equivalent device with the UV-LIGA process will cost 20-times less than the MUMPs silicon process, and it also provides the stronger structures and has lower costs of capital fabrication equipment.

Although SU8 photoresist is easy to form the electroplating mold for the high-aspect-ratio structure in UV-LIGA process, the difficulty of removing this photoresist makes it impossible to fabricate the multi-layered structures. AZ photoresist can

substitute SU8 to become a material for mold and it is also a good sacrificial layer due to quickly dissolving in the solvent such as Acetone. Therefore, AZ photoresist is selected to be the electroplating mold in my fabrication process.

Besides, the saw-toothed linear motor owns more benefits mentioned in the previous section than the push-clamp stepmotor, such as accurate open-loop position control, continuously smooth motion, infinitesimal motion resolution, and long duration life. Thus the saw-toothed linear motor is selected as the actuator to drive my design micromanipulator.

Chapter 3

Spatial Micromechanism Modeling

3.1 Device Description

A complete designed spatial micromechanism shown in Figure 3.1 contains three prismatic joints, driven by individual electrothermal linear motors, which connect to compliant pseudo-revolute joints capable of providing either in-plane or out-of-plane rotation. At the coaxial point for all three limbs with prismatic and compliant joints, a small platform acts as the end effector of the device. Although current designs use platforms on the order of 200 um wide, overall dimensions of 24 mm in diameter are typical for the full mechanism including linear motors and bond pads. The manipulator is fabricated in four consecutive electroplated layers. The bottom layer is 10 um thick and is used to create anchors for the thermal actuators and bond pads, as well as dimples for sliding elements. The function of anchors is to suspend the thermal beams after releasing, so the beams can move on the parallel plane of the wafer. Besides, because each linear motor is symmetric on both sides of the slider, the electric circuits can connect related bond pads to reduce the total number of bond pads from 16 to 6 on each linear motor. The 20-um thick second layer serves to form the thermal actuators, linear motor's slider, prismatic joints, electric circuits, bond pads, anchors of slider caps, and in-plane compliant joints. The 5-um thick third layer provides out-of-plane compliant joints, and creates anchors for capping elements which prevent the prismatic joints from lifting off the substrate after moving. The final 20-um thick layer includes the slider caps, prismatic

joint caps, and the end effector platform of the mechanism. In the final goal, a platform can move in three-dimensional space, as shown in Figure 3.2, through its surrounding actuators driving three individual limbs of the mechanism. The following sections will individually depict the main three parts of this device in detail.

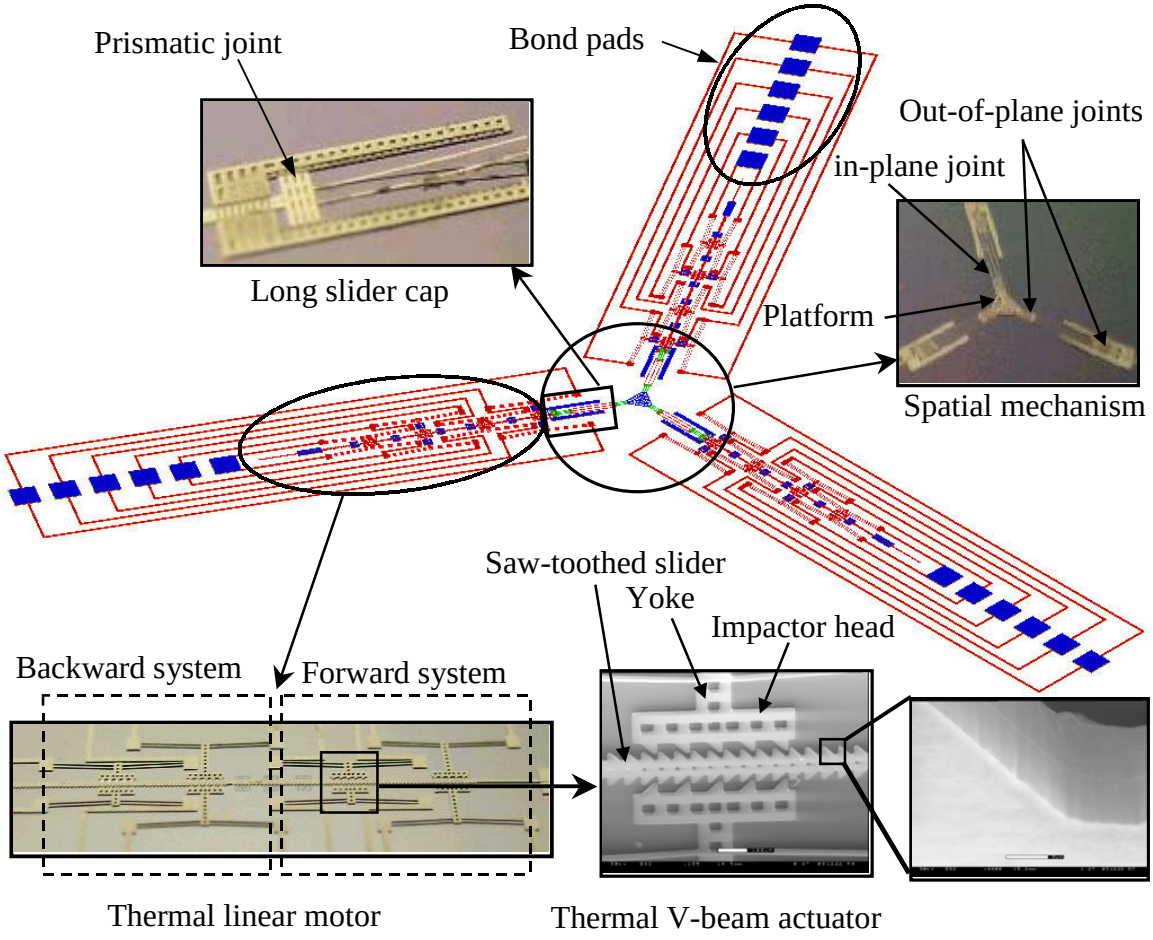

Figure 3.1: Micro parallel manipulator with thermal linear motors.

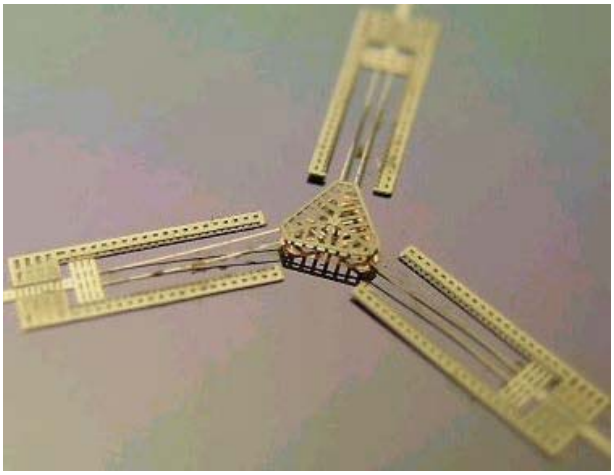

Figure 3.2: Pop-up platform of a spatial mechanism.

3.1.1 Thermal Actuator

The thermal actuator inside the linear motor generates the power to drive the slider in a straight continuous motion and meanwhile supply the force on the slider to overcome the loading. The V-beam actuator produces only translational motion on the middle tip of the V-beam, and it is also suitable for arraying V-beams to provide more force without losing its deflection. The multiple arrayed V-beams can share the common anchors located on the both ends of V-beam, so they are effectively wired in parallel to activate simultaneously. As shown in Figure 3.3, the thermal actuator owns two pairs of V-beams.

The impactor with wedge-type tooth attaches in the front of actuator's yoke. This impactor matching the saw-toothed slider can give a good mechanical efficiency on the output force of the slider, which will be discussed in the section 3.4. In addition, if the yoke of thermal actuator is stiff enough, which means it can still maintain straight forward movement without bending and only slipping motion occurs on the contact surface of the wedge, then the displacement of the slider can be simply determined by the

deflection of the thermal beam. This situation can also be easily achieved by adding the stop beside the impactor head, as shown in Figure 2.3.

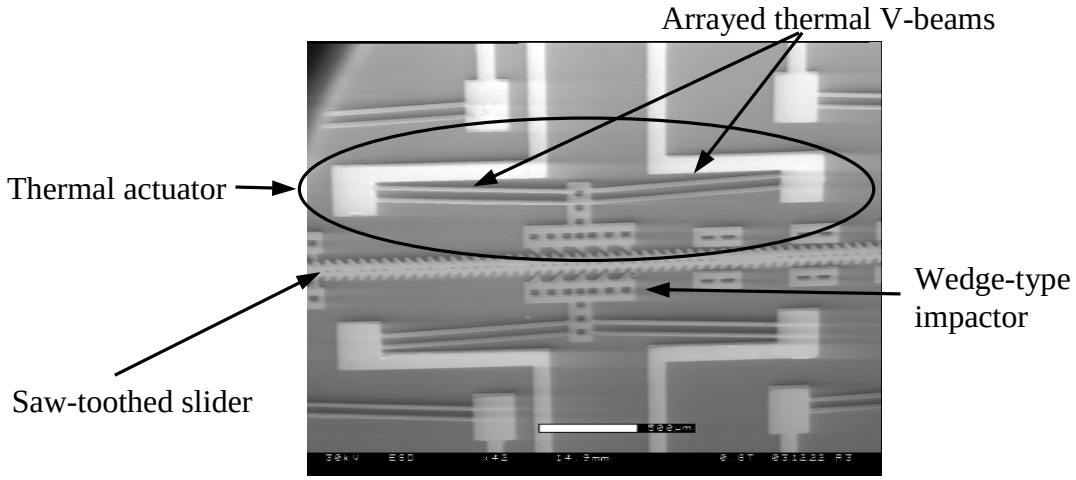

Figure 3.3: Thermal actuators and the slider of a linear motor.

3.1.2 Linear Micromotor

The linear micromotor shown in Figure 3.4 employs four sets of thermal V-beam actuators matched with a saw-toothed slider. Each thermal actuator contains two pairs of V-beam actuators to generate sufficient force to push and lock the slider. The two adjacent sets of thermal actuators close to the mechanism serve to move the slider in the forward direction, and the remaining two sets use opposing teeth to push the slider in the reverse direction. The actuation details of this linear motor will be discussed in the later chapter. The total travel of each bi-directional linear motor in fabricated devices is as large as 4.1 mm. The travel length can reach 8.2 mm if the shape of the tooth on the slider changes to an isosceles trapezoid, and the four sets of thermal actuators with impactors

are relocated to match this new shape of tooth.

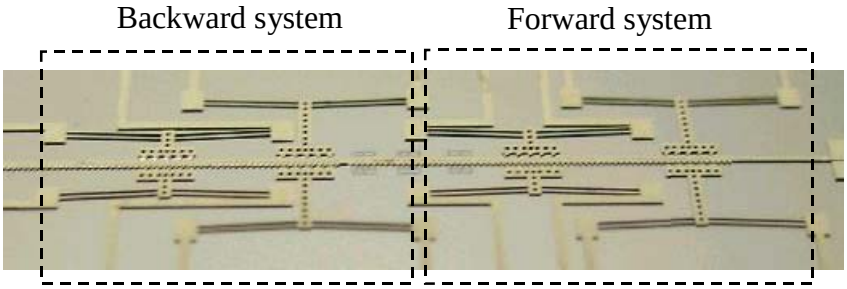

Figure 3.4: Four pairs of thermal actuators in a saw-toothed linear motor.

3.1.3 Spatial Micromechanism

The spatial mechanism shown in Figure 3.5 contains three identical kinematic chains connected with the center platform. In the connection sequence from the base to the platform, each chain consists of a prismatic joint, a first out-of-plane compliant joint, an in-plane compliant joint, and a second out-of-plane compliant joint. In order to constrain the prismatic joint to remain within the wafer plane during slide, long slider caps, as shown in Figure 3.1, are located on the end of each linear motor connected with a prismatic joint. The out-of-plane compliant joint fabricated in the third layer is a thin flat beam, so it easily rotates in the pitch direction during deformation. The in-plane compliant joint fabricated in the second layer is a high-aspect-ratio beam, so it should easily deform in the yaw direction. In the design, two parallel beams are used as in-plane joints to enhance the stiffness in the roll direction, so that they can prevent the joints from deforming in the roll direction. The compliant joints in this spatial manipulator are aimed to ideally deform in the only one direction, so that the mechanism analysis can be easy to handle. The kinematics and dynamics of this mechanism using the pseudo-rigid-body

model will be discussed in the later sections.

After the whole structure is released, the platform must be higher than all limbs to ensure it will move upward during actuation. Using a needle fabricated from the first and second layers to support the platform can make sure the platform is in the highest position after release. The structures, including the platform, compliant joints and sliders of thermal linear motors, drop down to the wafer plane during releasing. Because the third layer is thinner than the first layer in the design, the needle beneath the platform stops the falling platform when other structures keep dropping. Therefore, comparing to all other movable structures after releasing, the platform maintains in the highest position. However, if the above method is used, the slider of the linear motor may have a risk of stiction on the wafer due to the lack of dimples under the slider.

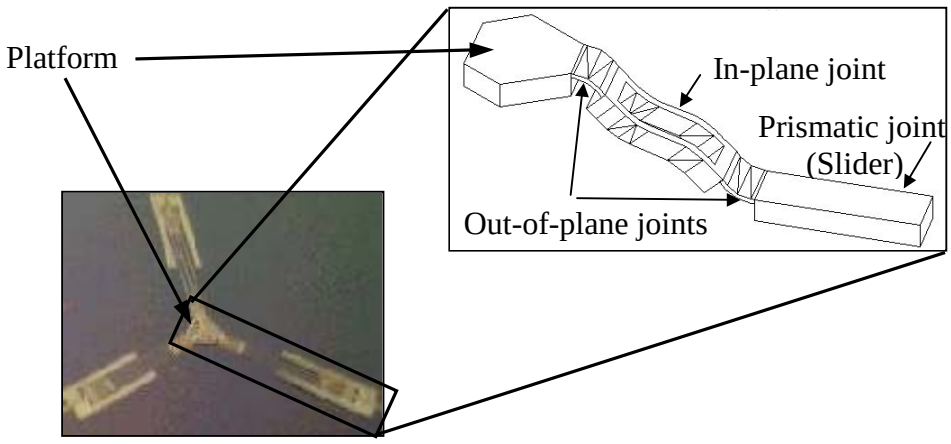

Figure 3.5: Micro spatial mechanism in a designed micromanipulator.

3.2 Thermodynamic Analysis of Thermal Actuators

3.2.1 Introduction

The analysis and design of thermal actuators require solving the electrothermal, thermomechanical and heat transfer problems. The actuator uses the constant current or power passing through the whole V-beam to cause thermal expansion. In this Joule heating process belonging to an electrothermal problem, the heat transfer phenomenon needs to be considered to obtain a steady-state heat equation. After thermal expansion on the beam, the V-shape beam can ensure its deformation along the desired direction. The output displacement and force on the middle tip of the V-beam due to its thermal expansion is a thermomechanical problem. In the following sections, the theoretical models in the displacement and force analysis with the pseudo-rigid-body model are discussed. The experimental results of fabricated thermal actuators are used to verify the theoretical models.

The pseudo-rigid-body model [29] uses a virtual pivot with a torsional spring connected with two rigid links to represent a compliant body, so the end point of the flexible beam after elastic deformation can be described as the last end point of two connected rigid links, as shown in Figure 3.6. Unlike the matrix method [16] [18], using this method to express the compliant mechanism will greatly simplify the process of analysis and shorten the calculation time.

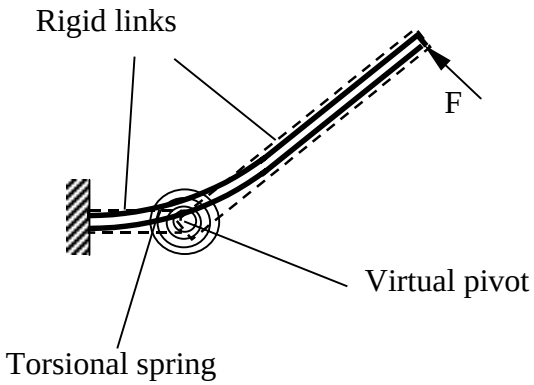

Figure 3.6: Pseudo-rigid-body model of an elastically deformed beam.

3.2.2 Displacement Analysis Using Pseudo-Rigid-Body Model

Because the displacement of thermal actuator depends on the thermal expansion of V-beam due to Joule heating, the temperature distribution on the line-shape beam determines the amount of thermal expansion. In the case of a very small gap under a suspended beam, the conduction through the air to the substrate is a dominated heat loss and the convection and radiation heat loss can be negligible [20]. To calculate the total heat conduction loss from the whole surrounding edge of the beam to the substrate, the shape factor is introduced to represent the ratio of the total heat flux divided by the heat flux passing through the bottom of the structure. Besides, this ratio is independent of the temperature variation on the cross-section of the beam.

Shape Factor Analysis:

Figure 3.7 shows the contour of heat flux from surrounding edge of the beam to the substrate using ANSYS finite element model. According to the simulation result, the most heat loss is from the bottom of the beam to the substrate. The shape factor (S) is

developed by finite element modeling using ANSYS, and given by

$$S = \frac{h}{w}\left[2.09\left(\frac{h}{g_a}\right)^{-0.663}\right] + 1 \tag{3.1}$$

where w is the width of the beam, h is the thickness of the beam, and g_a is the gap between the beam and the substrate. In this simulation, beam thickness is varied from 5 to 60 um and the gap is varied from 2 to 6 um, but the beam width keeps in 10 um as the design limitation which is the minimum beam width done in my fabrication process. Figure 3.8 compares the above fitting equation with the ANSYS simulation results.

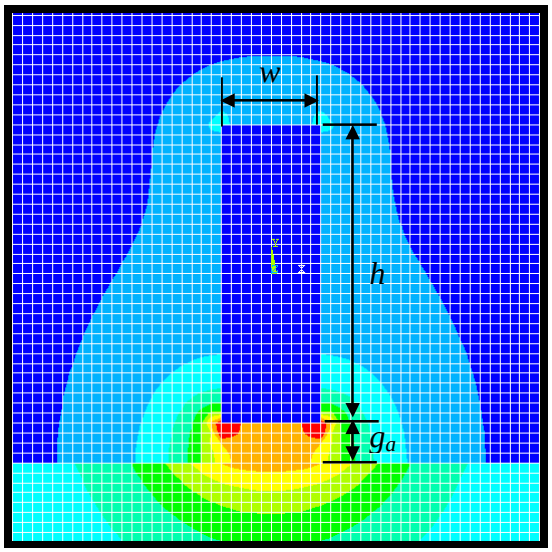

Figure 3.7: Contour of the heat flux from the surrounding edge of a beam to the substrate using ANSYS simulation.

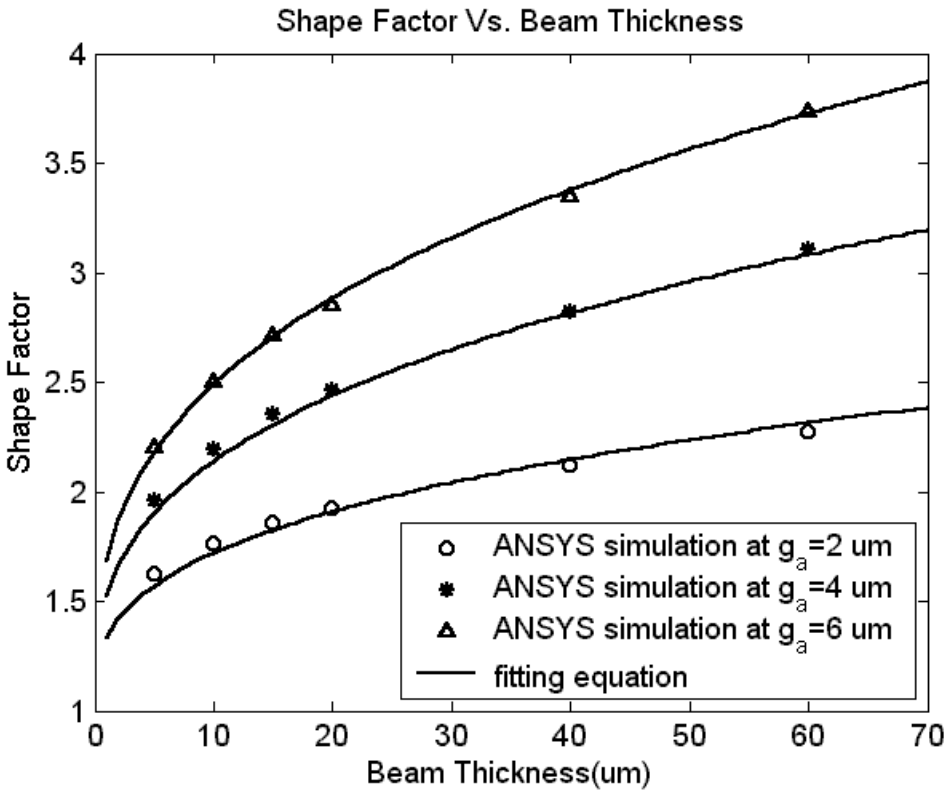

Figure 3.8: Comparison of the shape factor equation with simulation results.

Electrothermal Analysis:

In order to simplify the electrothermal model of the thermal V-beam, the thermal conductivity, resistivity, and thermal expansion coefficient of nickel are initially assumed to be independent of temperature. Besides, because the substrate has a relatively large thickness as a heat sink, the upper surface of the substrate and the anchor of the thermal actuator are assumed to maintain at ambient temperature. Figure 3.9 displays the differential element of V-beam actuator applied the constant current for the model analysis. The steady-state heat equation can be written as [3]

$$k_n wh\frac{d^2T_{(x)}}{dx^2} + J^2\rho wh - Sk_a w\left(\frac{T_{(x)} - T_\infty}{g_a}\right) = 0 \qquad (3.2)$$

where k_n is the thermal conductivity of nickel, k_a is the thermal conductivity of air, $T_{(x)}$ is the temperature on the position x of the beam, T_∞ is the ambient temperature, J is the current density through the beam, ρ is the resistivity of nickel, L is the length of V-beam between two anchors. Solving this differential equation with the boundary conditions, $T_{(0)} = T_{(L)} = T_\infty$, the temperature distribution on the V-beam is

$$T_{(x)} = T_\infty + \frac{J^2 \rho}{k_n m^2}\left(1 - \frac{e^{m(L-x)} + e^{mx}}{e^{mL} + 1}\right) \tag{3.3}$$

where $m^2 = \dfrac{Sk_a}{k_n g_a h}$

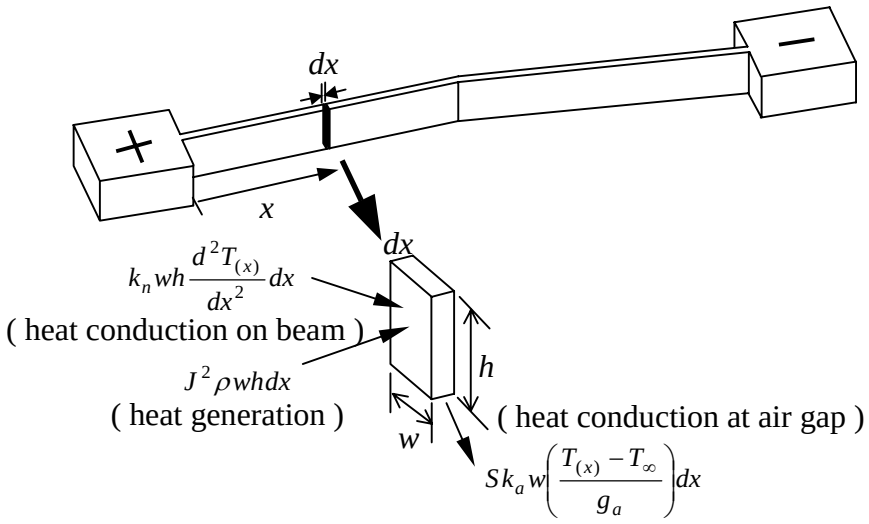

Figure 3.9: Differential element of a V-beam actuator used in the electrothermal model analysis.

Thermomechanical Analysis:

The V-beam will be buckled after heating up because both ends are clamped and its total length is extended. Figure 3.10 displays the elastic deformation of the left half V-

beam after Joule heating using the pseudo-rigid-body model. For the clamp-clamp beam, there is an inflection point in the middle of the deformed beam and only force without any moment applies at this point. According to the ANSYS simulation, this inflection point only has 0.0005% shift error in the middle place between the anchor and the yoke, as the centerline shown in Figure 3.10. Hence, it is reasonable that assuming this inflection point of the curve consistently resides in the middle place, and the displacement of thermal V-beam after Joule heating can be calculated as the following steps using this assumption. First, the total length of thermal V-beam for the first quarter after thermal expansion, L_{total}, is

$$L_{total} = \frac{L}{4} + \Delta L = \frac{L}{4} + \alpha \int_0^{L/4} \left[T_{(x)} - T_\infty\right] dx \qquad (3.4)$$
$$= \frac{L}{4} + \frac{\alpha J^2 \rho}{k_n m^2}\left[\frac{L}{4} + \frac{\sinh(mL/4)}{m\cosh(mL/2)} - \frac{\tanh(mL/2)}{m}\right]$$

where α is a thermal expansion coefficient of nickel. Based on the pseudo-rigid-body model and the above assumption, the position of the inflection point (X', Y') can be obtained as

$$X' = \frac{L}{4}\cos(\beta) \qquad (3.5)$$

$$Y' = \sqrt{\gamma^2 L_{total}{}^2 - \left(\frac{L}{4}\cos(\beta) - (1-\gamma)L_{total}\cos(\beta)\right)^2} + (1-\gamma)L_{total}\sin(\beta) \quad (\gamma = 0.8517) \qquad (3.6)$$

where γ is a characteristic radius factor in the pseudo-rigid-body model, β is an offset angle of the thermal V-beam. Then the deflection generated from this quarter length, dl_1, is

$$dl_1 = Y' - \frac{L}{4}\sin(\beta) \tag{3.7}$$

Since the temperature distribution is different between the first quarter and the second quarter of the V-beam, the deflection of each quarter is necessary to consider separately. The total length of thermal V-beam for the second quarter after thermal expansion, L'_{total}, is

$$\begin{aligned} L'_{total} &= \frac{L}{4} + \alpha \int_{L/4}^{L/2} \left[T_{(x)} - T_{\infty}\right] dx \\ &= \frac{L}{4} + \frac{\alpha J^2 \rho}{k_n m^2}\left[\frac{L}{4} - \frac{\sinh(mL/4)}{m\cosh(mL/2)}\right] \end{aligned} \tag{3.8}$$

Using the same calculation process, the deflection generated from this second quarter length, dl_2, is

$$\begin{aligned} dl_2 = &\sqrt{\gamma^2 L'^{\,2}_{total} - \left(\frac{L}{4}\cos(\beta) - (1-\gamma)L'_{total}\cos(\beta)\right)^2} \\ &+ (1-\gamma)L'_{total}\sin(\beta) - \frac{L}{4}\sin(\beta) \end{aligned} \tag{3.9}$$

Then the total displacement of thermal V-beam, d_t, is the summation of dl_1 and dl_2, namely,

$$d_t = dl_1 + dl_2 \tag{3.10}$$

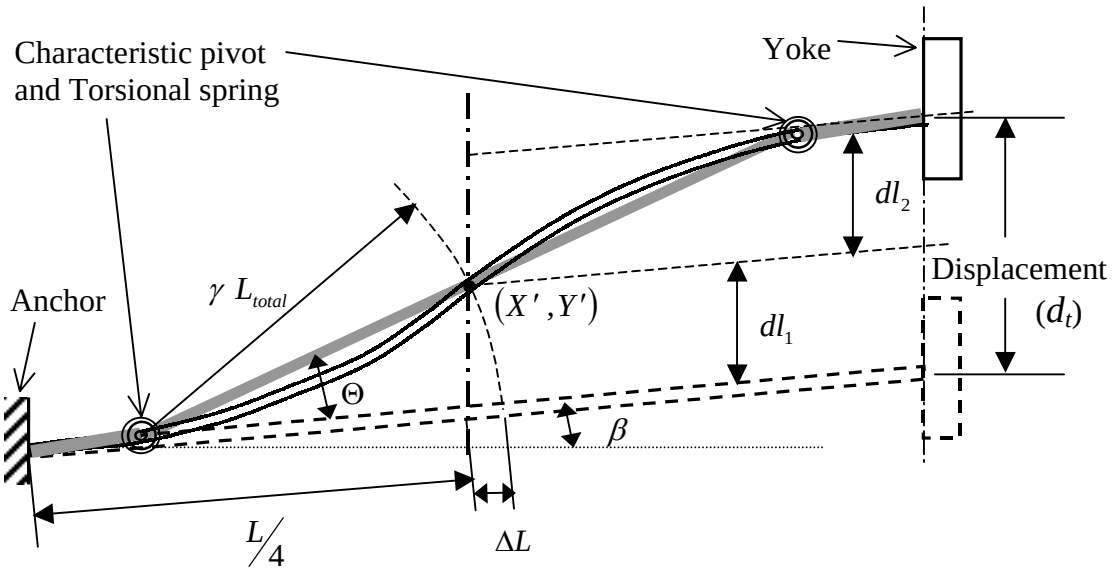

Figure 3.10: Illustration of an elastic deformation of the left half V-beam using the pseudo-rigid-body model after Joule heating.

3.2.3 Force Analysis Using Pseudo-Rigid-Body Model

Thermal force is the dominant source to produce the output force of thermal actuator on the yoke due to thermal expansion and it is proportional to the thermal strain. If the thermal V-beam does not change the shape during heating, then the thermal force, F_{th}, inside the half of V-beam at the zero displacement of the thermal V-beam should be

$$F_{th} = \sigma_{th} A = E\varepsilon_{th} A = E\frac{\alpha\int_0^{L/2}\left[T_{(x)} - T_\infty\right]dx}{L/2} A = \frac{E\alpha\, w\, h\, J^2\rho}{k_n m^2}\left(\frac{2 + mL\, e^{mL} + mL - 2\, e^{mL}}{mL\left(e^{mL} + 1\right)}\right) \quad (3.11)$$

where σ_{th} is thermal stress, A is the cross-section area of the V-beam, E is the Young's modulus of nickel and ε_{th} is the thermal strain. Then the output force along the moving direction of yoke, F_t, at the zero displacement due to thermal stress is equal to

$$F_t = 2F_{th}\sin(\beta) = \frac{2E\alpha\, wh\sin(\beta)J^2\rho}{k_n m^2}\left[1-\frac{2\tanh(mL/2)}{mL}\right] \tag{3.12}$$

However, during appearing the displacement on the tip of V-beam, the thermal strain on the V-beam will gradually change smaller due to stress release in the beam's deformation. Therefore, the magnitude of F_t varying with the displacement becomes zero as the tip of V-beam reaches the maximum displacement (d_{max}) in a free loading condition with a certain input current because the thermal V-beam gains the full extension. This can be explained why the maximum output force of V-beam occurs on the zero displacement and zero output force appears at the maximum displacement during a fixed input current [3]. Now, under the loading condition of yoke, the variation of the thermal strain is assumed to be inversely linear proportional to the displacement of the V-beam, and the V-beam angle connected with the yoke is assumed to maintain in β as an offset angle during the V-beam deformation. Then the output force $F_{t(d_e)}$ at the displacement d_e along the moving direction of yoke due to thermal stress could be

$$F_{t(d_e)} = F_{t(0)}\frac{d_{\max} - d_e}{d_{\max}} \tag{3.13}$$

Actually, the maximum displacement is equal to the displacement evaluated by the previous discussion in Eq. (3.10). In addition, according to the pseudo-rigid-body model in Figure 3.11, the displacement d_e on the yoke of V-beam is caused by a force F_e as

$$F_e = \frac{32EI\,K_\Theta\Theta}{L^2\cos(\Theta+\beta)} \quad , \quad \Theta \cong \sin^{-1}\left(\frac{2d_e\cos\beta}{\gamma L}\right) \tag{3.14}$$

where Θ is a pseudo-rigid-body angle shown in Figure 3.10, I is moment inertia of the V-

beam, and K_Θ is a stiffness coefficient equaling to 2.6762 [29]. Then the net output force on the yoke, F_n, at the displacement d_e can be calculated as

$$F_n = F_{t(d_e)} - F_e \tag{3.15}$$

In general, the elastic force F_e is much smaller than the force $F_{t(d_e)}$ generated from the thermal stress in the V-beam.

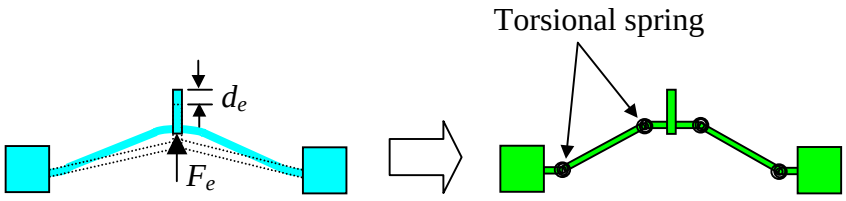

Deformed thermal V-beam

Pseudo-rigid-body model of the deformed thermal V-beam

Figure 3.11: Pseudo-rigid-body model of the deformed thermal V-beam.

3.2.4 Experiment and Testing Results

The fabricated thermal V-beams have been tested to verify the above analysis models. To obtain the better results, the supercritical dry process was used to prevent stiction problems after removing all sacrificial layers. Otherwise, in most cases, the thermal actuators can also be successfully released after completely soaking in acetone or methanol and then moving into a hot oven at 80^{o}C to evaporate the solvent.

In the test process, the constant current applied through probes located in contact

with the bond pads on the anchors of thermal beams. The microscope monitor was used to observe the displacement when the current was applied, and the caliper was used to measure the displacement. Then the measurements transferred to real displacements according to the proportion of amplification under the microscope. Figure 3.12 shows the relation between input current and its corresponding displacement on tips of different configurations of thermal V-beams which are varied in the width (W), length (L), thickness (H) and offset angle (Ang). The material properties for the theoretical analysis using the pseudo-rigid-body model (PRBM) are listed in Table 3.1. Based on the results of Figure 3.12, the matches between model analysis and experimental results at large current levels have considerable discrepancies. Those discrepancies are believed to be caused by the strong temperature dependence of material properties such as the electrical resistivity, the thermal conductivity, and the coefficient of thermal expansion. Therefore, the following model analysis will take this into account and accordingly improve the analysis accuracy. At the case of offset angle equaling 2 degrees, large discrepancies appear in the beginning of the low current level. The possible reason is that the V-beam buckles at other places rather than at the tip of V-beam due to insufficient offset angle for the V-beam. However, once the tip of V-beam moves, the deformation will concentrate on this tip.

Table 3.1: Material properties used in the V-beams analysis.

Property	value
Young's modulus of nickel (E)	195 GPa
Resistivity of nickel (ρ)	8.47×10^{-8} ohm-m
Thermal conductivity of nickel (k_n)	90.5 W/m-K
Thermal expansion coefficient of nickel (α)	13.4×10^{-6} K^{-1}
Thermal conductivity of air (k_a)	0.026 W/m-K
Ambient temperature (T_∞)	298 K
Specific heat of nickel (c_n)	444 J/kg-K
Density of nickel (D_n)	8900 kg/m^3

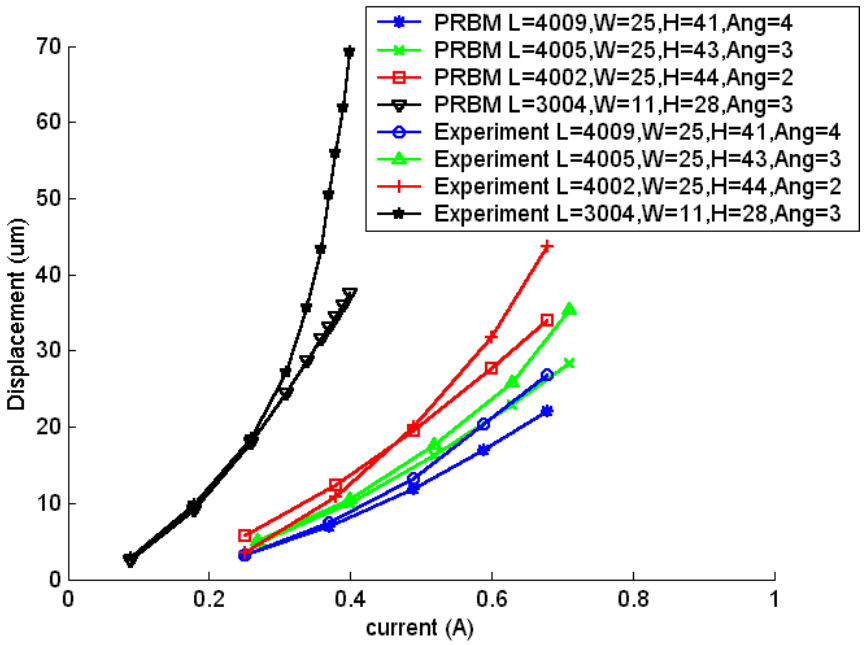

Figure 3.12: Displacement vs. input current for different configurations of thermal V-beams.

Figure 3.13 displays displacement versus current for different pairs of thermal V-beams with the same configuration. In this model analysis, every pair of V-beam is assumed passing through the same current and possessing the same deformed shape during heating due to the same geometry and electrical resistance on each pair. Hence in multiple pairs of V-beam, the current passing through each pair is equal to total input current divided by the number of pairs. Then the identical analysis for the single pair of V-beam can be used to evaluate the displacement of multiple pairs of V-beams. Again, large discrepancies at higher current levels are occurred due to the strong temperature dependence of material properties.

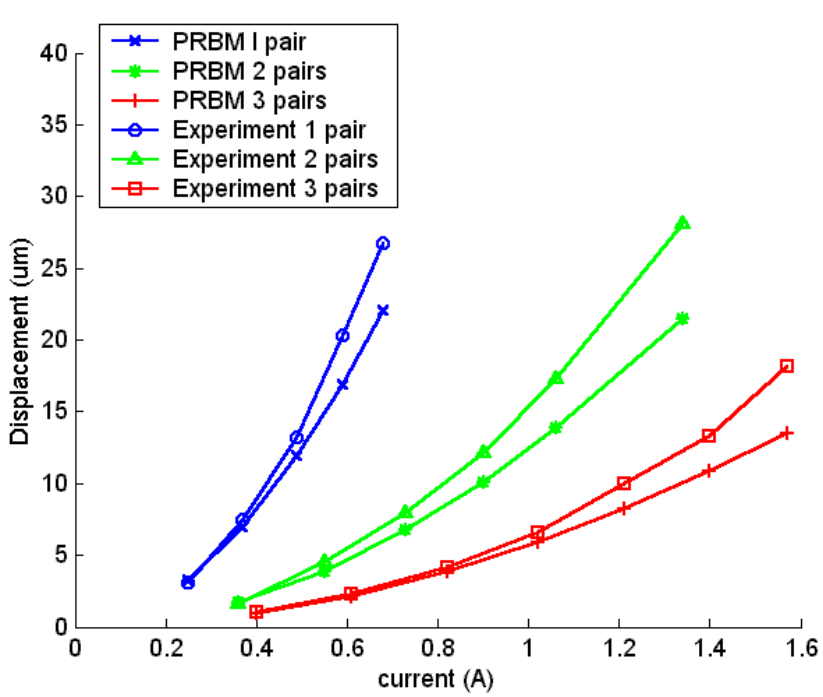

Figure 3.13: Displacement vs. current for different pairs of thermal V-beams. (L = 4009 um, w=25 um, h= 41 um, β = 4 deg)

In order to measure the force, the folded flexure spring is connected with the yoke of the thermal V-beam, as shown in Figure 3.14. Then the force applying on the folded flexure spring is the displacement of the yoke multiplying the spring constant. The flexure spring constant, *K*, is determined from its geometry of the folded flexure spring and it equals

$$K = \frac{12EI_s}{L_s^3} = \frac{Eh_s w_s^3}{L_s^3} \tag{3.16}$$

where I_s is the moment inertia of the spring beam, L_s is the length of each folded spring as shown in Figure 3.14, h_s is the thickness of the spring, and w_s is the width of the spring. Figure 3.15 demonstrates the net output force vs. current for different pairs of thermal V-beams. In this case, each pair of thermal V-beam is assumed to be the same condition, so the input current is equally divided to pass through each pair and the total net output force is the summation of the all pairs of thermal V-beams. Based on the experimental results in Figure 3.15, when the higher current is applied on the V-beams connected with a spring at the end of the yoke, the V-beams become weak and soft causing the dropping force at high temperature. The experimental results also show the bad agreements with the theoretical model on the higher input current. It is still believed that the source of these errors is from the temperature sensitivity of material properties.

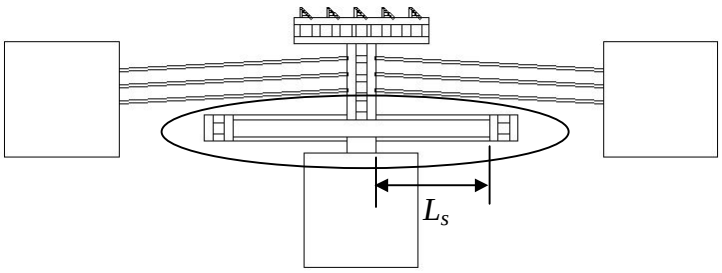

Figure 3.14: Folded flexures used to measure the V-beam force.

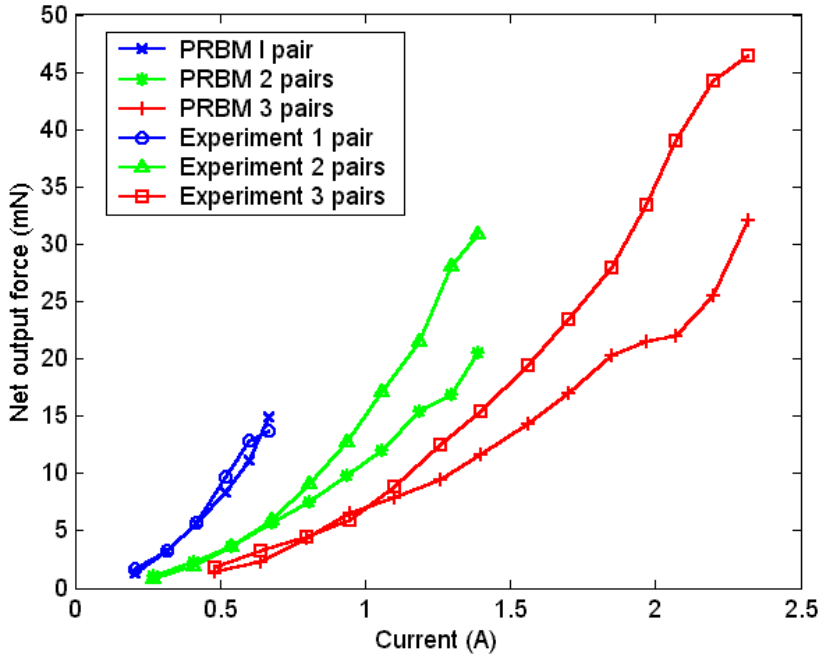

Figure 3.15: Net output force vs. current for different pairs of thermal beams. (L = 4005 um, w=22 um, h = 41 um, β = 3 deg)

Since the temperature dependence of material properties is a major concern to correct the errors on the higher input current, some material properties such as the thermal conductivity, the electrical resistivity, and the coefficient of thermal expansion

have to be identified the variations with the temperature. However, the data of temperature dependent material properties are not easy to know and to define them, especially for the electroplated nickel. In this research, the nickel is assumed to be high purity after electroplating. From the experimental data [71], the fitting equation for the thermal conductivity of nickel is approximated by

$$k_n(T) = 6.2\times10^{-11}T^4 - 2.9923\times10^{-7}T^3 + 5.3241\times10^{-4}T^2 - 0.3878T + 163.41 \quad (3.17)$$

where T is the temperature in the unit of ^{o}K. Figure 3.16 shows the above fitting equation in a solid line compared with those experimental data on thermal conductivity of nickel. On the other hand, there are good data about the coefficient of thermal expansion varied with temperature from the electroplated nickel using a nickel sulfamate bath. The fitting equation from those data is defined as

$$\alpha(T) = 10^{-6}\times\left(6.25\times10^{-9}T^3 - 1.6279\times10^{-5}T^2 + 1.721\times10^{-2}T + 9.1168\right) \quad (3.18)$$

The above fitting equation and the data from Safranek [73] are displayed in Figure 3.17.

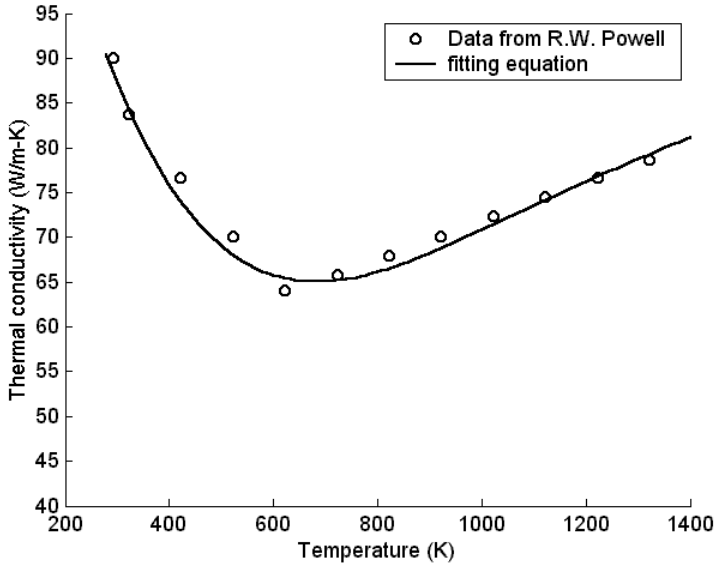

Figure 3.16: Thermal conductivity of nickel varied with temperature.

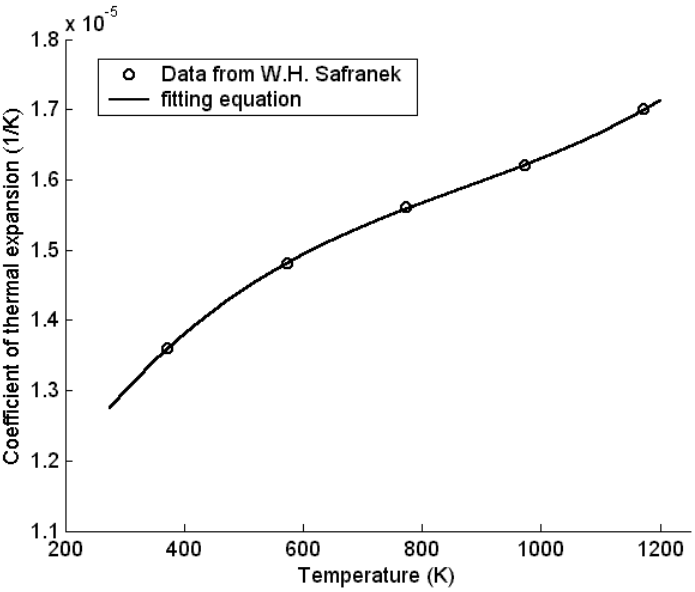

Figure 3.17: Coefficient of thermal expansion varied with temperature in nickel.

No exact equations or experimental data can be found in the literature about the temperature-dependent electrical resistivity of the electroplated nickel. However, there is

a simple theory about the relation between the electrical resistance and the temperature, that is,

$$R = R_0\left[1 + \beta_c (T - T_0)\right] \tag{3.19}$$

$$\Rightarrow \rho = \rho_0\left[1 + \beta_c (T - T_0)\right]\left[1 + \alpha (T - T_0)\right] \approx \rho_0\left[1 + \beta_c (T - T_0)\right] \tag{3.20}$$

where R and R_0 are the electrical resistance at temperature T and T_0, respectively, β_c is the temperature coefficient of resistance, and ρ_0 is the electrical resistivity of nickel at initial reference temperature T_0. According to the literature, the values of ρ_0 and β_c for nickel are 8.4e-8 ohm-m [73] and 2.3e-3 K^{-1} [74], respectively. Thus the temperature-dependent equation of electrical resistivity in nickel is

$$\rho(T) = 8.4 \times 10^{-8} + 1.932 \times 10^{-10}(T - 293) \tag{3.21}$$

Consequently, after considering the temperature-dependent material properties, the equation of temperature distribution on the thermal V-beam becomes extremely nonlinear during heating. Only numerical solution can be used to approximate the equation by dividing the half beam into n elements and using the temperature of the previous element n-1 to determine the material properties for the next element n. The program has been written by MATLAB™ to obtain this numerical solution for the displacement and force on thermal V-beams. In the same previous cases, considering temperature effects on the material properties, the revised predictions of displacement and force using the numerical method are shown from Figure 3.18 to Figure 3.20.

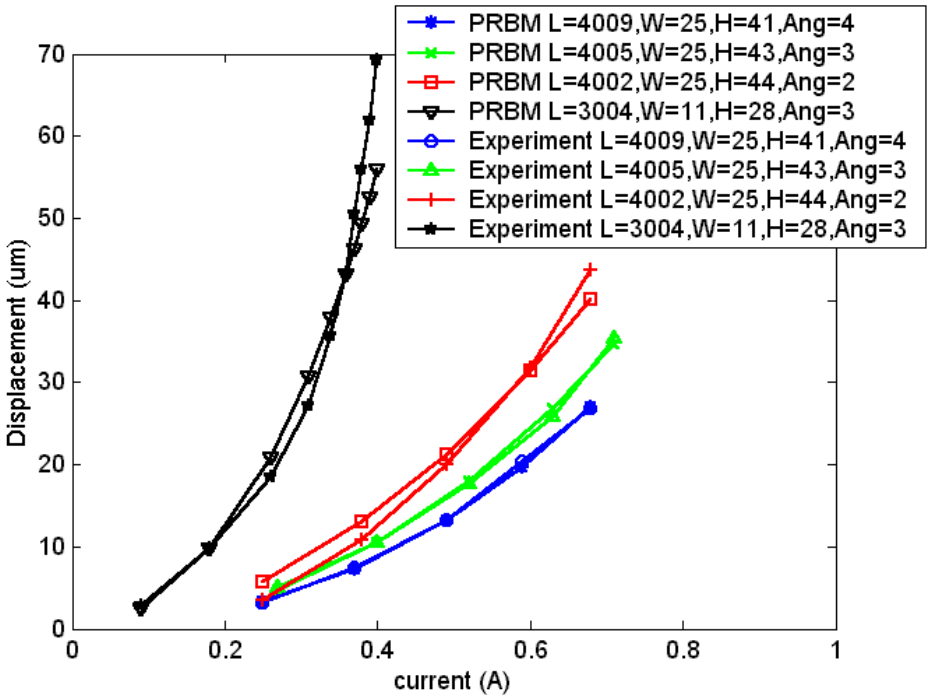

Figure 3.18: Displacement vs. current for different configurations of thermal V-beams considering temperature-dependent material properties.

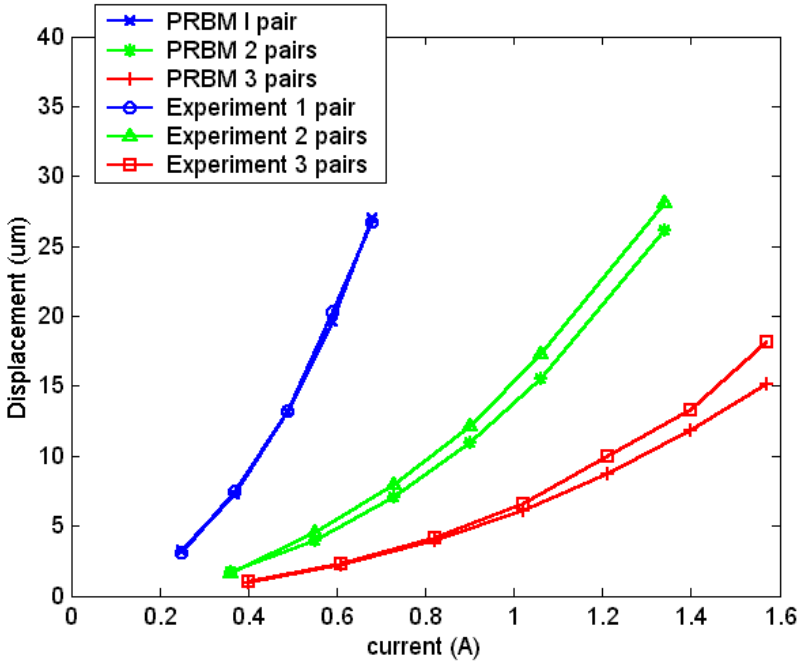

Figure 3.19: Displacement vs. current for different pairs of thermal V-beams considering temperature-dependent material properties.

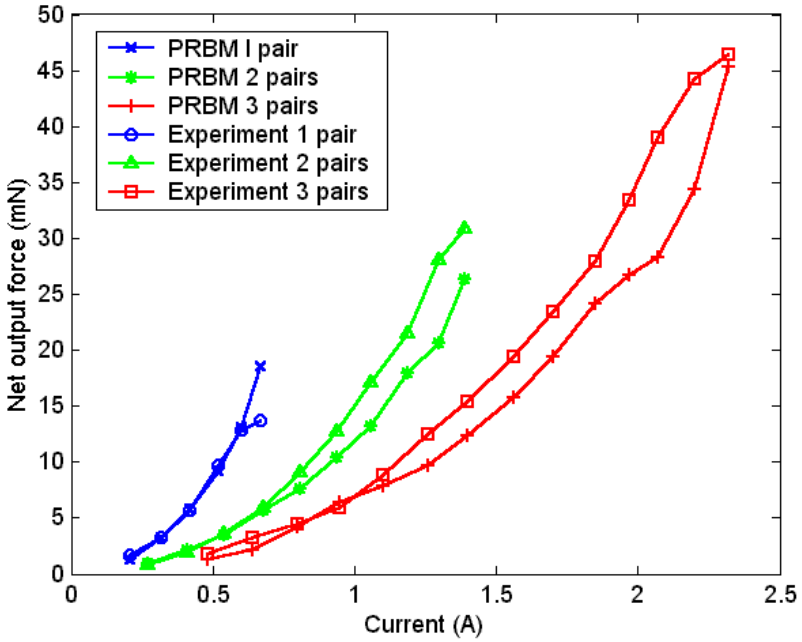

Figure 3.20: Net output force vs. current for different pairs of thermal beams considering temperature-dependent material properties.

Comparing with the previous results without considering the temperature effects on material properties, the agreement between the experiment and the model is much better on the higher current. The temperature effects on material properties in nickel will be discussed below. First, the decrease in the thermal conductivity at high temperature stores more heat inside the beam, then higher temperature inside the beam tends to increase the deflection due to heat storage. Even when the thermal conductivity converts into rising after the nickel temperature exceeds the curie temperature of nickel around 354^{o}C, the deflection of thermal V-beams still continues increasing due to the dominant deflection effect from other material properties, especially from the electrical resistivity. After another fitting equation of the thermal conductivity acquired from the experimental data [71][72] with different purity is used to calculate the numerical solution, it is

discovered that the thermal conductivity holds a small influence on the displacement of thermal V-beams. Additionally, the increase in the thermal expansion coefficient and the resistivity at high temperature undoubtedly raise more deflection. The increase in the resistivity enhances the temperature inside the beam; moreover, the increase in the thermal expansion coefficient enlarges the expanding length. Hence, the displacement on the thermal beam at high temperatures will be revised much more to match the prediction in the model analysis while considering temperature-dependent material properties. However, some discrepancies between theoretical and experimental results are still remained. They are not only from the assumption in the theory and the measurement uncertainty in the experiment, but also from the contact resistance and the thermal resistance on a probe during measurement. In a bad connection situation, the contact resistance always dominates the most part of the total testing electrical resistance due to the lower electrical resistance of nickel beams. Using the large probe tip head or soldering the wire to the bond pad can reduce the contact resistance between the testing sample and the measurement instrument, but the contact resistance is still difficult to control due to varied contact conditions. Therefore, the contact resistance is believed to be the main error source in the experimental data. Furthermore, the matching agreement in the single pair of V-beam is better than the multiple pairs. The bad matching discrepancies on the multiple pairs are believed to cause from the inaccuracy of the shape factor derived from the single pair. The shape factor used in the model analysis for the multiple pairs should be smaller than that used in the single pair because the heat out of the beam can affect the adjacent beam’s heat dissipation on itself sidewall surface. That is why the predictions are always smaller than the experimental results under the conditions

of the multiple pairs in Figure 3.19 and Figure 3.20. Therefore, in order to further improve the agreement, the shape factor using in the PRBM has to be modified to fit the conditions of the multiple pairs. Alternatively, the space between each pair of V-beam can be enlarged to reduce the mutual heat effects to agree with the conditions in the single pair.

3.3 Frequency Response Analysis of Thermal Actuators

The frequency response experiment is performed on a thermal actuator mounting vertically and used a laser Doppler vibrometer to measure the displacement with focusing the laser on the side of an impactor. Figure 3.21 shows the frequency response of the thermal actuator with a length of 2003 um, a width of 15 um, and a thickness of 22 um while actuating in various input power. The full stroke of motion can be maintained at low frequencies. After the frequency passing 60 Hz, the response begins to drop due to insufficient time for finishing each heating/cooling cycle. As illustrated in the figure, the time constant of this thermal actuator is maintained at about 10 ms regardless of its displacement and input power. Since the horizontally traveling length of the tooth on the slider is 30 um in this test, the operational speed can be as high as 1.8 mm/s calculated from the maximum operational frequency (60 Hz) multiplying the traveling length of the slider per cycle (30 um).

The theoretical analysis of the first-mode time constant, τ_1, can be calculated from [3]

$$\tau_1 = \left(\frac{\pi^2 k_n}{c_n D_n L^2} + \frac{S\, k_a}{g_a h c_n D_n} \right)^{-1} \tag{3.22}$$

where c_n is the specific heat of nickel and D_n is the density of nickel. Using the material properties in Table 3.1, the above testing V-beam actuator is predicted to have a first-mode time constant about 3.34 ms. The error between the theory and the experiment is believed to induce from using the constant material properties for nickel without considering temperature effects.

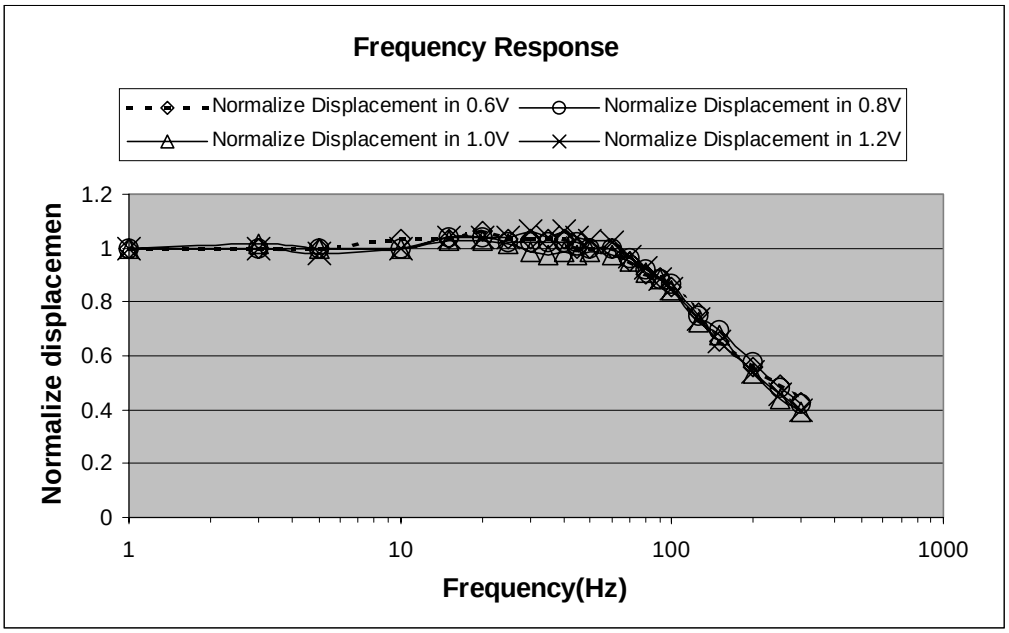

Figure 3.21: Frequency response of a thermal actuator showing independence to actuation voltage.

3.4 Linear Micromotor Force Analysis

The force analysis between the thermal actuator and the slider will be discussed in this section. As mentioned in the section 2.1.4, this force analysis is easier than the push-clamp stepmotor due to no elastic deformation on the yoke. Therefore, the direction of

force generated from the thermal V-beams can be considered to parallel the moving direction of the yoke. To simplify the model analysis, only one single wedge element on the slider and the impactor is studied, as shown in Figure 3.22. On the body 1 as an impactor of the thermal actuator, the static balance force without considering the impact effects is

$$\begin{cases} N\cos\theta = \mu N\sin\theta \\ F_n = N\sin\theta + \mu N\cos\theta \end{cases} \tag{3.23}$$

where μ is a friction coefficient on the contact surface between the slider and the impactor head, N is a normal force on the contact surface, θ is an angle of the wedge-shape tooth and F_n is the previous net force generated from thermal V-beams. Then solving Eq.(3.23) the friction coefficient and the normal force are

$$\mu = \cot\theta\,, \quad N = \frac{F_n}{\sin\theta + \cot\theta\cos\theta} \tag{3.24}$$

On the body 2 as the saw-toothed slider in Figure 3.22 , another equation for static balance is

$$\begin{aligned} 2N\cos\theta &= F_s + 2\mu N\sin\theta \\ \Rightarrow F_s &= \frac{2F_n(\cos\theta - \mu\sin\theta)}{\sin\theta + \mu\cos\theta} \end{aligned} \tag{3.25}$$

where F_s is the loading force generated from the spatial mechanism at the end of the slider.

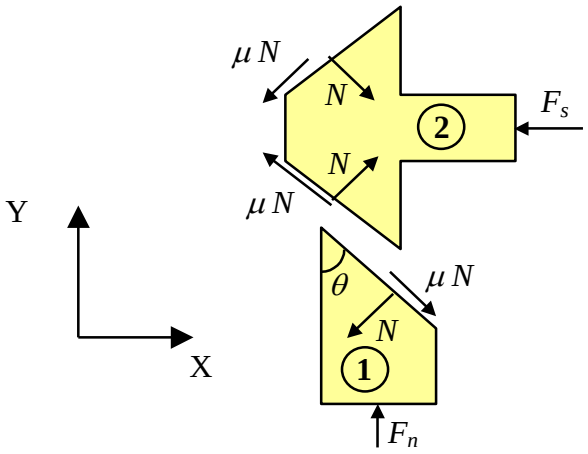

Figure 3.22: Free body diagram of a saw-toothed slider and an impactor head of a thermal actuator.

In order to move the slider forward, the parallel slider force F delivered from the thermal actuator has to cancel the loading force F_s, and then let the remained force drive the slider forward. The characteristic of a wedge is used to achieve $F > F_s$ by amplifying the force generated from the thermal actuator. For example, if $F > 2F_n$ is desired, the relation from Eq.(3.25) must be

$$\sin\theta + \mu\cos\theta < \cos\theta - \mu\sin\theta \tag{3.26}$$

Therefore, in the condition of gaining at least double actuator force on the slider, if the wedge angle θ is known as a design requirement, the coefficient of friction must satisfy

$$\mu < \frac{\cos\theta - \sin\theta}{\cos\theta + \sin\theta} \tag{3.27}$$

On the other hand, if the coefficient of friction is determined, the wedge angle must satisfy

$$\theta < -\tan^{-1}\left(\frac{-1+\mu}{1+\mu}\right) \tag{3.28}$$

The relation between the wedge angle and the friction coefficient on this situation is shown in Figure 3.23. The lower section of this figure offers higher mechanical efficiency. The mechanical efficiency of this motor is defined as

$$\text{Mechanical efficiency} = \frac{F}{F_n} = \frac{2(\cos\theta - \mu\sin\theta)}{\sin\theta + \mu\cos\theta} \tag{3.29}$$

Figure 3.24 displays the relationship between the wedge angle and the mechanical efficiency according to different friction coefficients. Based on analytical results, the smaller wedge angle is selected, the larger mechanical efficiency of the linear motor is generated. However, If this wedge angle is too small then the sharp tip will be difficult to fabricate and it will also be too weak to support the slider. As discussed above, the contact surface between the slider and the impactor becomes smoother after wearing a while. That means the friction coefficient becomes smaller and the mechanical efficiency will also be increased. This is very useful to improve the performance of the mechanism because the higher loading can be sustained in the moving platform after operating a while in this manipulator.

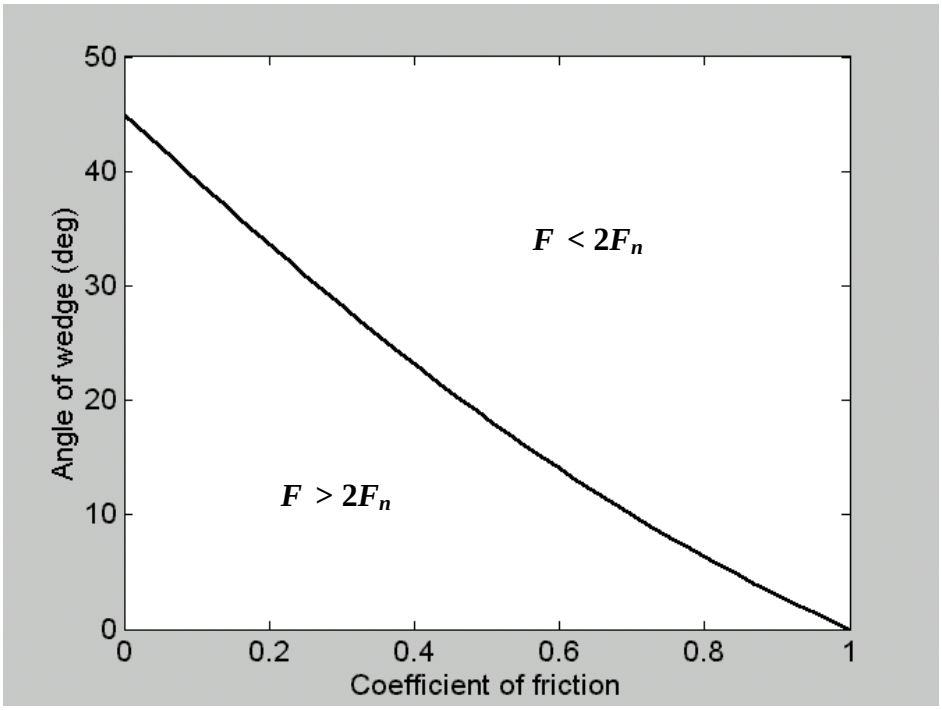

Figure 3.23: Two parts of an output slider force in different conditions.

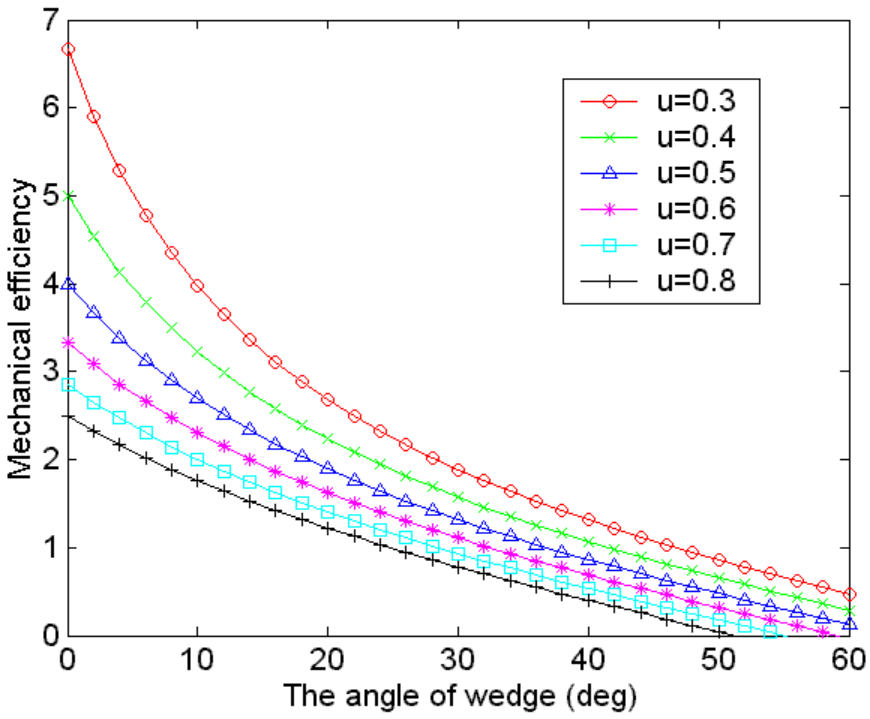

Figure 3.24: Relation between mechanical efficiency and the wedge angle on different friction coefficients.

3.5 Kinematic Analysis of Spatial Parallel Micromanipulators

Using the matrix method [16][18] to derive the compliance matrix of the whole mechanism is very cumbersome and complex, especially for a compliant mechanism. Unfortunately, the designed micromechanism fabricated from the UV-LIGA process belongs to a compliant mechanism, which means that the joints in the mechanism are compliant. In order to simplify the analysis process, the well-known rigid body kinematics can be applied on the complex analysis of a compliant mechanism after the pseudo-rigid-body model [13][29] is used to describe a compliant mechanism.

3.5.1 Pseudo-Rigid-Body Model of Micromanipulators

The compliant joints in the mechanism are modified to become pseudo rigid bodies first, so the compliant mechanism can obtain its pseudo-rigid-body model to simplify the analysis process. If out-of-plane joint only rotates in the pitch direction and can be ignored the insignificant deformation in other directions during applying the force at the free end of the beam, then it would like a traditional revolution joint with a torsional spring connected with two rigid rods, as shown in Figure 3.25. In this figure, L_b is the total length of thin beam acted as a compliant joint, and the value of γ is not substantially changed, which is varied between 0.8517 and 0.8391 due to the different loading directions applied on the free end of beams [29]. Figure 3.26 exhibits the pseudo-rigid-body model of the in-plane compliant joint mounted on the designed mechanism. In the in-plane compliant joint, two characteristic pivots locate on the flexible beam due to

the conditions of a clamp-clamp beam, so the pseudo-rigid-body model of this joint is like two traditional revolution joints with torsional springs connected with three rigid links.

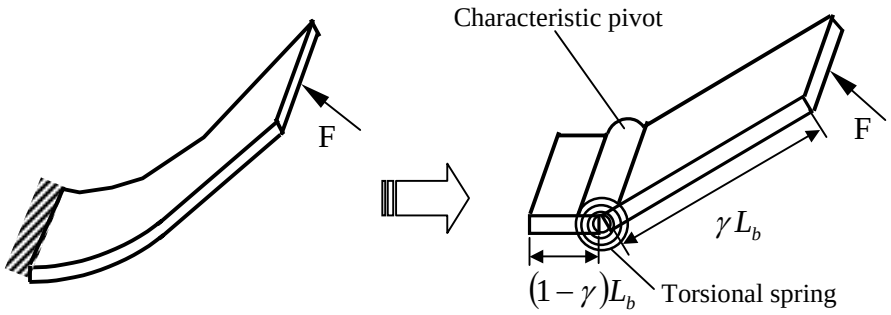

Figure 3.25: Pseudo-rigid-body model of the out-of-plane compliant joint.

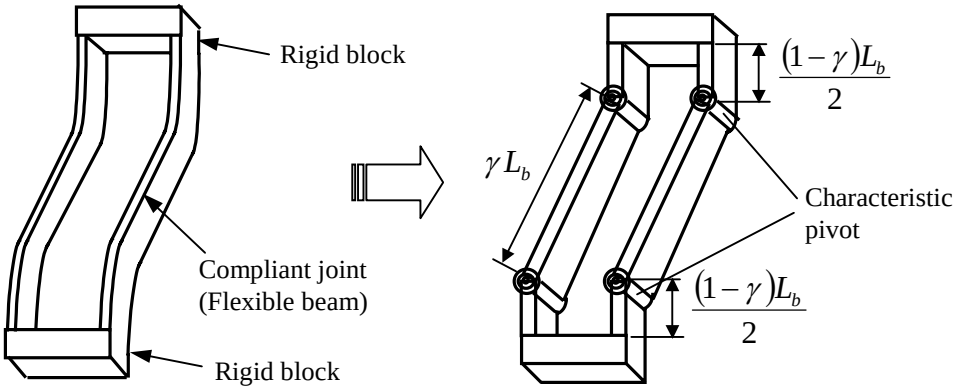

Figure 3.26: Pseudo-rigid-body model of the in-plane compliant joint.

After replacing the original compliant mechanism with the above pseudo-rigid-body models of the compliant joints, the new mechanism model is shown in right side of Figure 3.27. According to this new mechanism model, each limb of the working platform is a PRRRR type of mechanism, where P represents a prismatic joint combined with a

thermal linear motor and R indicates a revolution joint located on a characteristic pivot in the pseudo-rigid-body model.

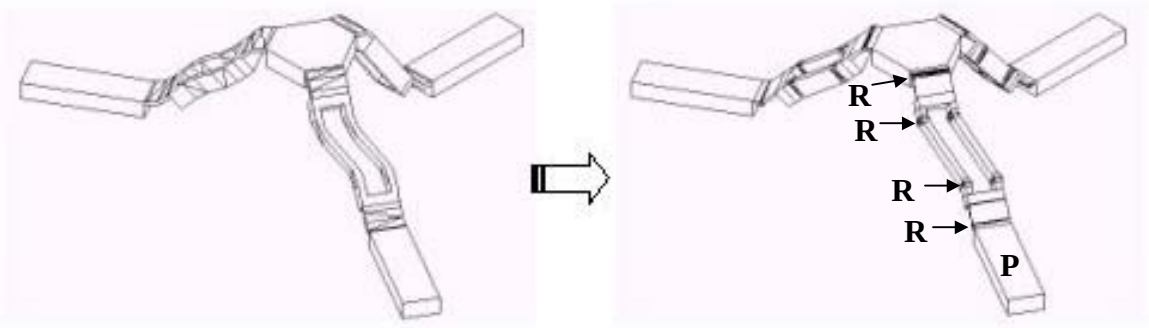

Figure 3.27: Compliant manipulator transforms into its corresponding pseudo-rigid-body model.

Based on the above pseudo-rigid-body model of the mechanism, the total degree of freedom for this spatial parallel manipulator can be calculated from [1]

$$Dof = 6(n_L - 1) - \sum_{i=1}^{j_n} c_i \tag{3.30}$$

where *Dof* is the degree of freedom in the mechanism, n_L is the number of links including the fixed link or the base, j_n is the number of joints, and c_i is the degree of constraint on relative motion imposed by the joint i. Thus the total degree of freedom for this mechanism is three calculated from n_L=14, j_n=15, and c_i=5. Actually, if every compliant joint can perform like a traditional revolution joint, the working platform of this parallel mechanism only moves in pure translation motion.

3.5.2 Inverse Kinematics of Micromanipulators

In order to control the position of the moving platform in the manipulator, the movement for each thermal linear motor surrounding the mechanism must be identified by the inverse kinematics. As illustrated in Figure 3.28, in each $x_iy_iz_i$ local coordinate system attached at the end of three prismatic joints, the center position of the moving platform can be described as

$$\begin{cases} Q_{x_i} = -b_i - \left(c_i + e_i + d_i\, Cos\theta_2^i\right) Cos\theta_1^i - f_i \\ Q_{y_i} = -d_i\, Sin\theta_2^i \\ Q_{z_i} = a + \left(c_i + e_i + d_i\, Cos\theta_2^i\right) Sin\theta_1^i \end{cases}, i = 1,2,3 \qquad (3.31)$$

where Q_{x_i}, Q_{y_i}, and Q_{z_i} are x-y-z local coordinates of the center point $\boldsymbol{Q}$ fixed in the platform. a is the thickness of the prismatic joint. b_i, c_i, d_i, e_i, and f_i are the distances depicted in Figure 3.28. θ_1^i is a rotation angle of the out-of-plane joint located in the ith limb. θ_2^i is a rotation angle of the in-plane joint located in the ith limb. Subsequently, changing the expression of Eq.(3.31) from the local coordinate to the XYZ global coordinate system, the equations described $\boldsymbol{Q}$ in the XYZ coordinate system are

$$\begin{bmatrix} Q_X \\ Q_Y \\ Q_Z \end{bmatrix} = \begin{bmatrix} Cos\phi_i & -Sin\phi_i & 0 \\ Sin\phi_i & Cos\phi_i & 0 \\ 0 & 0 & 1 \end{bmatrix} \begin{bmatrix} Q_{x_i} + P_i \\ Q_{y_i} \\ Q_{z_i} \end{bmatrix} \qquad (3.32)$$

$$\Rightarrow \begin{cases} Q_X = \left[-b_i - \left(c_i + e_i + d_i\, Cos\theta_2^i\right) Cos\theta_1^i - f_i + P_i\right] Cos\phi_i + d_i\, Sin\theta_2^i\, Sin\phi_i \\ Q_Y = \left[-b_i - \left(c_i + e_i + d_i\, Cos\theta_2^i\right) Cos\theta_1^i - f_i + P_i\right] Sin\phi_i - d_i\, Sin\theta_2^i\, Cos\phi_i \\ Q_Z = a + \left(c_i + e_i + d_i\, Cos\theta_2^i\right) Sin\theta_1^i \end{cases} \qquad (3.33)$$

where Q_X, Q_Y, and Q_Z are x-y-z coordinates of the center point $\boldsymbol{Q}$ expressed in the global coordinate system fixed in the center of the whole manipulator on the ground. P_i is

the distance between the origin of the global coordinate system and the end of the prismatic joint combined with the linear motor. ϕ_i is the rotation angle compared the global coordinate system with the local system settled on the *i*th limb.

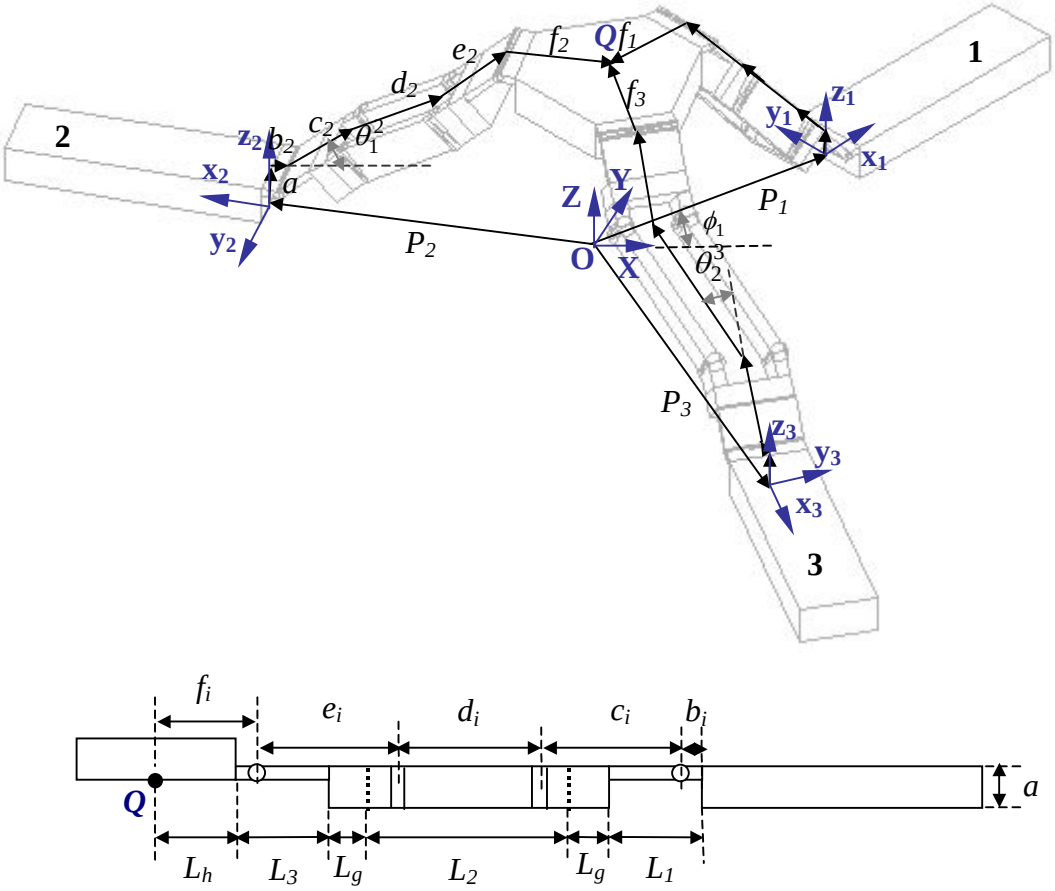

Figure 3.28: Coordinate configuration of the spatial parallel mechanism.

After converting the above equations, the inverse kinematics of the parallel manipulator in the pseudo-rigid-body model can be described as

$$\begin{cases} P_i = b_i + (c_i + e_i + AA)BB + f_i + Q_y \ Sin\phi_i + Q_x \ Cos\phi_i \\ \theta_1^i = \tan^{-1}\left(\dfrac{Q_Z - a}{c_i + e_i + AA}, BB\right) \\ \theta_2^i = \tan^{-1}\left(\dfrac{Q_x \ Sin\phi_i - Q_y \ Cos\phi_i}{d_i}, \dfrac{AA}{d_i}\right) \end{cases} \tag{3.34}$$

where

$$AA = \pm\sqrt{2Q_xQ_y \ Sin\phi_i Cos\phi_i - Q_x^2 \ Sin\phi_i^{\,2} + d_i^2 + Q_y^2 \ Sin\phi_i^{\,2} - Q_y^2} \tag{3.35}$$

$$BB = \pm\sqrt{\frac{(AA + c_i + e_i)^2 - (a - Q_z)^2}{(AA + c_i + e_i)^2}} \tag{3.36}$$

and

$$b_i = (1 - \gamma_1^i)L_1 \tag{3.37}$$

$$c_i = \gamma_1^i L_1 + L_g + \frac{(1 - \gamma_2^i)L_2}{2} \tag{3.38}$$

$$d_i = \gamma_2^i L_2 \tag{3.39}$$

$$e_i = \gamma_3^i L_3 + L_g + \frac{(1 - \gamma_2^i)L_2}{2} \tag{3.40}$$

$$f_i = L_h + (1 - \gamma_3^i)L_3 \tag{3.41}$$

where L_1, L_2, and L_3 are the length of the beams modeled as rotating compliant joints. L_g is the length of rigid blocks attached between out-of-plane joints and in-plane joints. L_h is the distance between the center of the platform and the platform edge connected with the out-of-plane joint. γ_1^i is the characteristic radius factor of the first out-of-plane compliant joint located in the *i*th limb near the linear motor. γ_2^i is the characteristic radius factor of the in-plane compliant joint located in the *i*th limb. γ_3^i is the characteristic radius factor

of the second out-of-plane compliant joint located in the *i*th limb near the moving platform.

3.6 Dynamic Analysis of Spatial Parallel Micromanipulators

3.6.1 Dynamic Equation

The Newton's law of motion is the most common approach used for dynamic analysis. However, for complex systems of rigid bodies, it is not always easy to determine appropriate equations to describe the dynamic behaviors of each component. In practice, each individual type of problem requires its own particular insights and techniques. In this section, using the Lagrangian approach to derive the dynamics of the micromanipulator is adopted to avoid the complicated analysis in Newton method. The Lagrangian method based on the kinetic energy and the work of systems is particularly useful in the analysis of mechanical systems which contain a number of rigid bodies that are connected in some way but may move relative to each other. Lagrangian method treats the system as a whole and only considers the forces that do work in the virtual displacement. Besides, it also provides a direct and systematic method to derive the dynamic model of the complex system. In general, the motion equations of the system can be presented as the following equations:

$$\frac{d}{dt}\left(\frac{\partial \hat{L}}{\partial \dot{q}_j}\right) - \frac{\partial \hat{L}}{\partial q_j} = \hat{Q}_j + \sum_{i=1}^{k} \lambda_i A_{ij}, \quad j = 1,2,.....,n \tag{3.42}$$

where *i* is the constraint index, *j* is the generalized coordinate index, *k* is the total number of constraint equations, *n* is the total number of generalized coordinates, $\hat{L}$ is the

Lagrangian function, q_j is the j-th generalized coordinate, $\hat{Q}_j$ is a generalized external force, λ_i is the Lagrange multiplier, CE_i is a constraint equation and $A_{ij} = \partial CE_i / \partial q_j$.

The characteristic radius factor in the pseudo-rigid-body model is assumed to be fixed at the average value 0.85 [29] to simplify the model due to insignificant variation in different loading conditions, that is, $\gamma_1^i = \gamma_2^i = \gamma_3^i = 0.85$ (i=1,2,3). Then the length of each link connected together in every limb of the manipulator expressed in the pseudo-rigid-body model is the same, namely, $b_1=b_2=b_3=b$, $c_1=c_2=c_3=c$, $d_1=d_2=d_3=d$, $e_1=e_2=e_3=e$, and $f_1=f_2=f_3=f$. Since the degree-of-freedom of the designed manipulator is three, the dynamic analysis could be done using only three generalized coordinates without any Lagrange multiplier. However, in this way the expression of the Lagrange function would be very cumbersome due to the complex kinematics of the manipulator. Thus the number of generalized coordinates is selected to conveniently describe the system first, and then some constrain equations are found to restrict the motion to fit the total degree-of-freedom in this system. In the following analysis, six Lagrange multipliers and nine generalized coordinates are used to express the dynamic equations. For this manipulator, as shown in Figure 3.29, the generalized coordinates in Lagrange equations are

$$q_j = \left(\theta_1^1, \theta_1^2, \theta_1^3, \theta_2^1, \theta_2^2, \theta_2^3, P_1, P_2, P_3\right) \quad , \quad j = 1,2,.....,9 \tag{3.43}$$

Then Eq.(3.42) represents a system of nine equations in nine unknown variables which are λ_i for i = 1 to 6 and three actuator forces, $\hat{Q}_j$ for j = 7 to 9. Other generalized external forces, $\hat{Q}_j$ for j = 1 to 6, are zero due to no externally applied forces or torques

at the pseudo joints. Therefore, solving these nine equations can obtain unique three actuator forces provided from linear motors.

Six constraint equations written in terms of the generalized coordinates are required in this Lagrangian model. The platform position can be described by the different forms based on each of the three manipulator limbs. However, these three different formulas indicate the same position. Thus six constraint equations are

$$\begin{cases} CE_i = Q_X^i - Q_X^{i+1} = 0\,, \quad i = 1, 2 \\ CE_j = Q_Y^{j-2} - Q_Y^{j-1} = 0\,, \quad j = 3, 4 \\ CE_k = Q_Z^{k-4} - Q_Z^{k-3} = 0\,, \quad k = 5, 6 \end{cases} \tag{3.44}$$

where Q_X^i, Q_Y^i, Q_Z^i are XYZ global coordinates of $\boldsymbol{Q}$ expressed in the parameters of the *i*-th limb. By substituting the parameters, constraint equations become

$$\begin{aligned} CE_i = &\left[-b-\left(c+e+d\cos\theta_2^i\right)\cos\theta_1^i - f + P_i\right]\cos\phi_i + d\sin\theta_2^i\sin\phi_i \\ &-\left[-b-\left(c+e+d\cos\theta_2^{i+1}\right)\cos\theta_1^{i+1} - f + P_{i+1}\right]\cos\phi_{i+1} - d\sin\theta_2^{i+1}\sin\phi_{i+1} \quad , i = 1, 2 \end{aligned} \tag{3.45}$$

$$\begin{aligned} CE_j = &\left[-b-\left(c+e+d\cos\theta_2^{j-2}\right)\cos\theta_1^{j-2} - f + P_{j-2}\right]\sin\phi_{j-2} - d\sin\theta_2^{j-2}\cos\phi_{j-2} \\ &-\left[-b-\left(c+e+d\cos\theta_2^{j-1}\right)\cos\theta_1^{j-1} - f + P_{j-1}\right]\sin\phi_{j-1} + d\sin\theta_2^{j-1}\cos\phi_{j-1} \quad , j = 3, 4 \end{aligned} \tag{3.46}$$

$$CE_k = \left(c+e+d\cos\theta_2^{k-4}\right)\sin\theta_1^{k-4} - \left(c+e+d\cos\theta_2^{k-3}\right)\sin\theta_1^{k-3} \quad , \quad k = 5, 6 \tag{3.47}$$

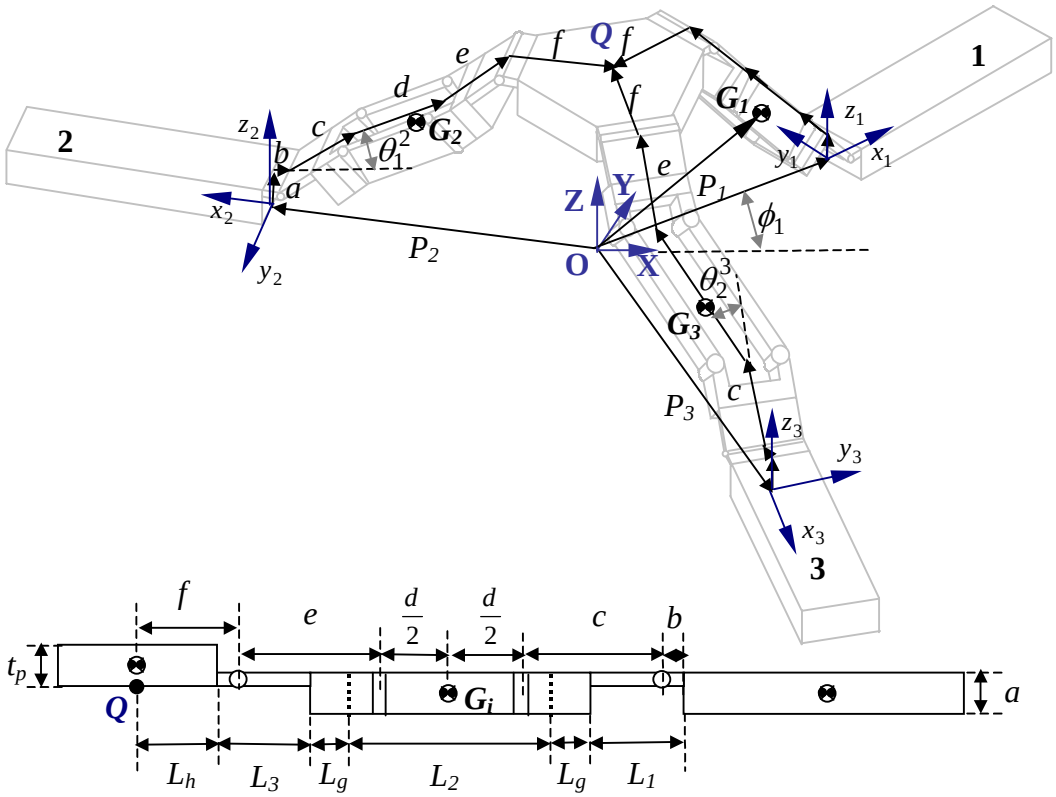

Figure 3.29: Coordinate configuration for the simplified model of the manipulator.

In order to derive dynamic equations, Lagrangian function $\hat{L}$, which is defined as the difference between the total kinetic energy of the system, $\hat{T}$, and the total potential energy of the system, $\hat{V}$, must be first developed. The whole manipulator can be divided into three parts -- the moving platform, the connecting bars, and linear motors. The following will separately discuss the kinetic and potential energy for each part.

(1) kinetic energy of the moving platform, $\hat{T}_p$

According to the pseudo-rigid-body model, some parts of out-of-plane compliant joints are combined with the moving platform during deformation, so the total mass of the moving platform, m_p, is defined as

$$m_p = \text{Platform mass} + 3^* \text{ the link mass of } (1-\gamma)L_3 + \text{loading mass} \tag{3.48}$$

Then the kinetic energy of the moving platform is

$$\begin{aligned} \hat{T}_p &= \frac{1}{2} m_p V_p^2 \\ &= \frac{1}{2} m_p \left(\dot{Q}_X{}^2 + \dot{Q}_Y{}^2 + \dot{Q}_Z{}^2 \right) \end{aligned} \tag{3.49}$$

In the above equation, V_p is the velocity of the moving platform and equals $\dot{Q}_X \vec{i} + \dot{Q}_Y \vec{j} + \dot{Q}_Z \vec{k}$. If the parameters of the number one limb, i=1, are selected to express the center point of the moving platform, then

$$\begin{cases} Q_X = \left[-b - \left(c + e + d\cos\theta_2^1 \right) \cos\theta_1^1 - f + P_1 \right] \cos\phi_1 + d\sin\theta_2^1 \sin\phi_1 \\ Q_Y = \left[-b - \left(c + e + d\cos\theta_2^1 \right) \cos\theta_1^1 - f + P_1 \right] \sin\phi_1 - d\sin\theta_2^1 \cos\phi_1 \\ Q_Z = a + \left(c + e + d\cos\theta_2^i \right) \sin\theta_1^1 \end{cases} \tag{3.50}$$

Thus the velocity of the moving platform is

$$\begin{cases} \dot{Q}_X = \left[d\dot{\theta}_2^1 \sin\theta_2^1 \cos\theta_1^1 + \left(c + e + d\cos\theta_2^1 \right) \dot{\theta}_1^1 \sin\theta_1^1 + \dot{P}_1 \right] \cos\phi_1 + d\dot{\theta}_2^1 \cos\theta_2^1 \sin\phi_1 \\ \dot{Q}_Y = \left[d\dot{\theta}_2^1 \sin\theta_2^1 \cos\theta_1^1 + \left(c + e + d\cos\theta_2^1 \right) \dot{\theta}_1^1 \sin\theta_1^1 + \dot{P}_1 \right] \sin\phi_1 - d\dot{\theta}_2^1 \cos\theta_2^1 \cos\phi_1 \\ \dot{Q}_Z = -d\dot{\theta}_2^1 \sin\theta_2^1 \sin\theta_1^1 + \left(c + e + d\cos\theta_2^1 \right) \dot{\theta}_1^1 \cos\theta_1^1 \end{cases} \tag{3.51}$$

and its kinetic energy becomes

$$\begin{aligned} \hat{T}_p = \frac{1}{2} m_p \Big[& \dot{P}_1{}^2 + d^2 \dot{\theta}_2^{1\,2} + (c+e)^2 \dot{\theta}_1^{1\,2} + 2\dot{P}_1 \dot{\theta}_1^1 \left(c + e + d\cos\theta_2^1 \right) \sin\theta_1^1 \\ & + 2d(c+e)\dot{\theta}_1^{1\,2} \cos\theta_2^1 + 2d\dot{P}_1 \dot{\theta}_2^1 \cos\theta_1^1 \sin\theta_2^1 + d^2 \dot{\theta}_1^{1\,2} \cos^2\theta_2^1 \Big] \end{aligned} \tag{3.52}$$

(2) kinetic energy of three connecting bars, $\hat{T}_c$

In pseudo-rigid-body model, the connecting bar between the moving platform and the linear motor consists of two out-of-plane joints and one deformable parallelogram formed by two in-plane joints. The total mass of this connecting bar, m_c, is defined as

$$m_c = 2 \text{ (mass of the link } L_2 + \text{mass of the rigid block} + \text{mass of the link } \gamma L_1) \quad (3.53)$$

Here the lengths of two out-of-plane joints are assumed to be the same, so the centroid of the connecting bar can be located at the centroid of the parallelogram-shape joint, as shown in Figure 3.29. Then the centroid point $\boldsymbol{G_i}$ expressed in the local coordinate, $O^{\,i}{}_{xyz}$, is considered as

$$\begin{cases} G_x^i = -b - \left(c + \dfrac{d}{2}\cos\theta_2^i \right)\cos\theta_1^i - \dfrac{a}{2}\sin\theta_1^i \cos\theta_2^i \\ G_y^i = -\left(\dfrac{d}{2} + \dfrac{a}{2}\sin\theta_1^i \right)\sin\theta_2^i \\ G_z^i = a + \left(c + \dfrac{d}{2}\cos\theta_2^i \right)\sin\theta_1^i - \dfrac{a}{2}\cos\theta_1^i \end{cases} \quad (3.54)$$

Expressed in the global coordinate, O_{XYZ}, the centroid point $\boldsymbol{G_i}$ becomes

$$\begin{bmatrix} G_X^i \\ G_Y^i \\ G_Z^i \end{bmatrix} = \begin{bmatrix} \cos\phi_i & -\sin\phi_i & 0 \\ \sin\phi_i & \cos\phi_i & 0 \\ 0 & 0 & 1 \end{bmatrix} \begin{bmatrix} G_x^i + P_i \\ G_y^i \\ G_z^i \end{bmatrix} \quad (3.55)$$

$$\Rightarrow \begin{cases} G_X^i = \left[P_i - b - \left(c + \dfrac{d}{2}\cos\theta_2^i \right)\cos\theta_1^i - \dfrac{a}{2}\sin\theta_1^i \cos\theta_2^i \right]\cos\phi_i + \left(\dfrac{d}{2} + \dfrac{a}{2}\sin\theta_1^i \right)\sin\theta_2^i \sin\phi_i \\ G_Y^i = \left[P_i - b - \left(c + \dfrac{d}{2}\cos\theta_2^i \right)\cos\theta_1^i - \dfrac{a}{2}\sin\theta_1^i \cos\theta_2^i \right]\sin\phi_i - \left(\dfrac{d}{2} + \dfrac{a}{2}\sin\theta_1^i \right)\sin\theta_2^i \cos\phi_i \\ G_Z^i = a + \left(c + \dfrac{d}{2}\cos\theta_2^i \right)\sin\theta_1^i - \dfrac{a}{2}\cos\theta_1^i \end{cases} \quad (3.56)$$

Then the kinetic energy of the connecting bar in the i-th limb, $\hat{T}_c^{\,i}$, is

$$\hat{T}_c^i = \frac{1}{2} m_c \dot{\overrightarrow{OG_i}} \bullet \dot{\overrightarrow{OG_i}}$$

$$= \frac{1}{2} m_c \left(\dot{G}_X^{i\,2} + \dot{G}_Y^{i\,2} + \dot{G}_Z^{i\,2} \right)$$

$$= \frac{1}{2} m_c \left\{ \left[\left(\dot{P}_i + \frac{d}{2}\dot{\theta}_2^i \sin\theta_2^i \cos\theta_1^i + (c + \frac{d}{2}\cos\theta_2^i)\dot{\theta}_1^i \sin\theta_1^i - \frac{a}{2}\dot{\theta}_1^i \cos\theta_1^i \cos\theta_2^i + \frac{a}{2}\dot{\theta}_2^i \sin\theta_2^i \sin\theta_1^i \right) \cos\phi_i \right.\right.$$

$$\left. + \frac{a}{2}\dot{\theta}_1^i \cos\theta_1^i \sin\theta_2^i \sin\phi_i + \left(\frac{d}{2} + \frac{a}{2}\sin\theta_1^i \right)\dot{\theta}_2^i \cos\theta_2^i \sin\phi_i \right]^2$$

$$+ \left[\left(\dot{P}_i + \frac{d}{2}\dot{\theta}_2^i \sin\theta_2^i \cos\theta_1^i + (c + \frac{d}{2}\cos\theta_2^i)\dot{\theta}_1^i \sin\theta_1^i - \frac{a}{2}\dot{\theta}_1^i \cos\theta_1^i \cos\theta_2^i + \frac{a}{2}\dot{\theta}_2^i \sin\theta_2^i \sin\theta_1^i \right) \sin\phi_i \right.$$

$$\left. - \frac{a}{2}\dot{\theta}_1^i \cos\theta_1^i \sin\theta_2^i \cos\phi_i - \left(\frac{d}{2} + \frac{a}{2}\sin\theta_1^i \right)\dot{\theta}_2^i \cos\theta_2^i \cos\phi_i \right]^2$$

$$\left. + \left[-\frac{d}{2}\dot{\theta}_2^i \sin\theta_2^i \sin\theta_1^i + \left(c + \frac{d}{2}\cos\theta_2^i \right)\dot{\theta}_1^i \cos\theta_1^i + \frac{a}{2}\dot{\theta}_1^i \sin\theta_1^i \right]^2 \right\} \qquad (3.57)$$

Thus the total kinetic energy from all three connecting bars, $\hat{T}_c$, is

$$\hat{T}_c = \hat{T}_c^1 + \hat{T}_c^2 + \hat{T}_c^3 \qquad (3.58)$$

(3) kinetic energy of three sliders, $\hat{T}_s$

There are three linear motors around the moving platform, so the total kinetic energy from these three sliders is

$$\hat{T}_s = \frac{1}{2} m_s \left(\dot{P}_1^{\,2} + \dot{P}_2^{\,2} + \dot{P}_3^{\,2} \right) \qquad (3.59)$$

where m_s is the mass of prismatic joints, which is also the slider of linear motors, in the manipulator.

Therefore, the total kinetic energy of the manipulator is equal to

$$\hat{T} = \hat{T}_p + \hat{T}_c + \hat{T}_s \tag{3.60}$$

The total potential energy of the manipulator is calculated relative to the base plane of the manipulator. Each potential energy of the individual manipulator part is discussed as following:

(1) potential energy of the platform, $\hat{V}_p$

The potential energy of platform is simply defined as

$$\begin{aligned} \hat{V}_p &= m_p g\left(Q_Z + \frac{t_p}{2} \right) \\ &= m_p g\left[a + \left(c + e + d\cos\theta_2^1 \right)\sin\theta_1^1 + \frac{t_p}{2} \right] \end{aligned} \tag{3.61}$$

where g is an acceleration of gravity and t_p is the thickness of the moving platform.

(2) potential energy of the connecting bar on the limb i, $\hat{V}_c^i$

Since the connecting bar contains two kinds of compliant joints, its potential energy involves the gravitational energy and its elastic deformation energy on the bending joints, that is,

$$\hat{V}_c^i = \hat{V}_G^i + \hat{V}_{ip}^i + \hat{V}_{op}^i \tag{3.62}$$

Where $\hat{V}_G^i$ is the gravitational potential energy of the centroid point $\boldsymbol{G_i}$ on the limb i, $\hat{V}_{ip}^i$ is the elastic deformation energy of the in-plane joint connected on the limb i, $\hat{V}_{op}^i$ is the elastic deformation energy of the out-of-plane joint attached on the limb i. Thus

$$\begin{aligned} \hat{V}_c^i &= m_c g G_Z^i + 4\frac{1}{2}K_{ip}\theta_2^{i\,2} + 2\frac{1}{2}K_{op}\theta_1^{i\,2} \\ &= m_c g\left[a + \left(c + \frac{d}{2}\cos\theta_2^i \right)\sin\theta_1^i - \frac{a}{2}\cos\theta_1^i \right] + \gamma K_\Theta EI\left(\frac{1}{L_1}\theta_1^{i\,2} + \frac{4}{L_2}\theta_2^{i\,2} \right) \end{aligned} \tag{3.63}$$

where K_{ip} and K_{op} are the torsional spring constants of in-plane joint and out-of-plane joint, respectively. The in-plane joint is considered as a fixed-fixed beam and the out-of-plane joint is like a fixed-free beam. Therefore, according to the pseudo-rigid-body model, the values of these spring constants are

$$\begin{aligned} K_{ip} &= 2\gamma K_\Theta \frac{EI}{L_2} \\ K_{op} &= \gamma K_\Theta \frac{EI}{L_1} \end{aligned} \tag{3.64}$$

(3) potential energy of three sliders, $\hat{V}_s$

As described in the above kinetic energy, the total potential energy from three sliders is

$$\hat{V}_s = \frac{3}{2} m_s g a \tag{3.65}$$

Therefore, the total potential energy of the manipulator is

$$\hat{V} = \hat{V}_p + \sum_{i=1}^{3} \hat{V}_c^i + \hat{V}_s \tag{3.66}$$

By substituting above three potential terms, the total potential energy of the manipulator is

$$\begin{aligned} \hat{V} = {} & m_p g \left[a + \left(c + e + d\cos\theta_2^1 \right) \sin\theta_1^1 + \frac{t_p}{2} \right] + \frac{3}{2} m_s g a \\ & + m_c g \sum_{i=1}^{3} \left[a + \left(c + \frac{d}{2}\cos\theta_2^i \right) \sin\theta_1^i - \frac{a}{2}\cos\theta_1^i \right] + \gamma K_\Theta EI \sum_{i=1}^{3} \left(\frac{1}{L_1}\theta_1^{i\,2} + \frac{4}{L_2}\theta_2^{i\,2} \right) \end{aligned} \tag{3.67}$$

Since the total kinetic and potential energy of the manipulator are known, the dynamic equations using Lagrangian function can be derived. By grouping the first set of six

equations given from Eq.(3.42), the system of six equations with six unknown Lagrange multipliers is formed as

$$\frac{d}{dt}\left(\frac{\partial \hat{L}}{\partial \dot{\theta}_1^1}\right)-\frac{\partial \hat{L}}{\partial \theta_1^1}=\sum_{i=1}^{6}\lambda_i A_{i1} \tag{3.68}$$

$$\frac{d}{dt}\left(\frac{\partial \hat{L}}{\partial \dot{\theta}_1^2}\right)-\frac{\partial \hat{L}}{\partial \theta_1^2}=\sum_{i=1}^{6}\lambda_i A_{i2} \tag{3.69}$$

$$\frac{d}{dt}\left(\frac{\partial \hat{L}}{\partial \dot{\theta}_1^3}\right)-\frac{\partial \hat{L}}{\partial \theta_1^3}=\sum_{i=1}^{6}\lambda_i A_{i3} \tag{3.70}$$

$$\frac{d}{dt}\left(\frac{\partial \hat{L}}{\partial \dot{\theta}_2^1}\right)-\frac{\partial \hat{L}}{\partial \theta_2^1}=\sum_{i=1}^{6}\lambda_i A_{i4} \tag{3.71}$$

$$\frac{d}{dt}\left(\frac{\partial \hat{L}}{\partial \dot{\theta}_2^2}\right)-\frac{\partial \hat{L}}{\partial \theta_2^2}=\sum_{i=1}^{6}\lambda_i A_{i5} \tag{3.72}$$

$$\frac{d}{dt}\left(\frac{\partial \hat{L}}{\partial \dot{\theta}_2^3}\right)-\frac{\partial \hat{L}}{\partial \theta_2^3}=\sum_{i=1}^{6}\lambda_i A_{i6} \tag{3.73}$$

Based on solving above equations to obtain the Lagrange multipliers, the actuator force of each linear motor can be directly determined from the three remaining equations:

$$F_1=\hat{Q}_7=\frac{d}{dt}\left(\frac{\partial \hat{L}}{\partial \dot{P}_1}\right)-\frac{\partial \hat{L}}{\partial P_1}-\sum_{i=1}^{6}\lambda_i A_{i7} \tag{3.74}$$

$$F_2=\hat{Q}_8=\frac{d}{dt}\left(\frac{\partial \hat{L}}{\partial \dot{P}_2}\right)-\frac{\partial \hat{L}}{\partial P_2}-\sum_{i=1}^{6}\lambda_i A_{i8} \tag{3.75}$$

$$F_3=\hat{Q}_9=\frac{d}{dt}\left(\frac{\partial \hat{L}}{\partial \dot{P}_3}\right)-\frac{\partial \hat{L}}{\partial P_3}-\sum_{i=1}^{6}\lambda_i A_{i9} \tag{3.76}$$

where F_i is the actuator force for the i-th limb of the manipulator. The details of A_{ij} evaluation and the required partial derivatives of the Lagrangian function are provided in Appendix B and C.

3.6.2 Numerical Example

The purpose of this numerical simulation is to provide some insights to the dynamics of the manipulator when its platform follows the desired trajectory. Besides, the dynamic model derived from the section 3.6.1 enables the evaluation of the required force on each linear motor for a given trajectory of the moving platform, so this force can be used to check the design of the thermal actuator inside the linear motor. If the force, which is supplied to push the platform into the edge of the working space, is not sufficiently provided by the thermal actuator, then the thermal V-beams need to be modified to fit the requirement.

To accomplish the simulation, first, the trajectory is selected to represent a typical motion, and then the inverse kinematics conducted in the section 3.5.2 obtains the corresponding values of the parameters in the manipulator. The typical trajectory includes three straight-line segments between four points, which are Q_1, Q_2, Q_3, and Q_4, to let the moving platform follow these paths. The first segment is let the platform move from Q_1, located at (0,0,200) in the XYZ coordinate system, to Q_2, located at (0,0,500), in 3 seconds, where the length dimensions are in micrometers. The second segment goes from Q_2 to Q_3 at (100,100,500) in 1.8 seconds. The third segment goes from Q_3 to Q_4 at (100,100,200) in 3 seconds. For each segment of the trajectory the platform starts and finishes with zero velocity and accelerates or decelerates on 300 um/sec^2. Figure 3.30

shows the conditions of this trajectory including the position, velocity, and acceleration in the three-dimensional space. The design parameters of the manipulator in this simulation are given in Table 3.2. Here the compliant joints of the manipulator are assumed to be the same width and thickness, so the moments of inertia of the two kinds of joints are the same. The characteristic radius factor, γ , and the stiffness coefficient, K_{Θ} , of the compliant joints are selected the average value to simplify this simulation. Using the inverse kinematics and the desired trajectory, the corresponding parameters of the manipulator are shown in Figure 3.31 to Figure 3.33. The velocity and acceleration of each parameter are calculated by numerical approximation of differential, that is,

$$\dot{f}(t) \cong \lim_{\Delta t \to 0} \frac{f(t+\Delta t) - f(t)}{\Delta t} \tag{3.77}$$

Here t denotes the time. By giving the above trajectory and the sets of calculated parameters, the actuator forces are calculated from the solutions of Eq.(3.68) to Eq.(3.76) and the results are shown in Figure 3.34. Based upon the results, it can be demonstrated that during the first segment of the trajectory, from t = 0 to t = 3, all limbs of the manipulator have the same motion and force because three lines in the figures are overlapping. In this segment, all three sliders provide the equal forces to push the limb and raise the platform. Moreover, these three forces are balanced on the center of the platform, so they keep the position of the platform on the XY plane and let the platform vertically rise in the Z direction. Each of three trajectory segments can be divided into there regions. The first region is the acceleration region during which the sliders supply forces to accelerate the platform to the second region, the constant velocity region. In the first segment of the trajectory the movement is vertically upward, the positive acceleration provides the inertia force to keep the platform moving upward. Hence,

during this period the pushing forces from the sliders are slightly decreased because the smaller forces are enough to maintain the motion. The identical phenomenon also happens in the region of the third segment of this trajectory. Once the constant velocity region is reached, a large step change in the magnitude of the actuator force can be observed to allow the moving platform to travel at a constant velocity. In the constant velocity region, the actuator force in the first segment gradually increases due to the growth of the potential energy, including both the gravity and the elastic stored energy. The inverse condition occurs due to the reduction of the potential energy in the third segment at the same region. Finally, in the deceleration region of the first and third trajectory segment, the actuator force slightly increase to eliminate the inertia force to slow down the moving platform until it stops at the desired position. Furthermore, because the lower position of the moving platform needs more force to bend the compliant joint, the first segment of the trajectory, vertically upward motion, owns a stepwise decreasing force change as soon as the region alters. For the same reason, the third segment of the trajectory with vertically downward movement possesses a stepwise increasing change of force when the region shifts. In the second segment of the trajectory, the limb 2 provides more force than the limb 1 and 3 to laterally push the platform. Meanwhile, this force from the limb 2 also transfers to other limbs to gradually decrease their forces.

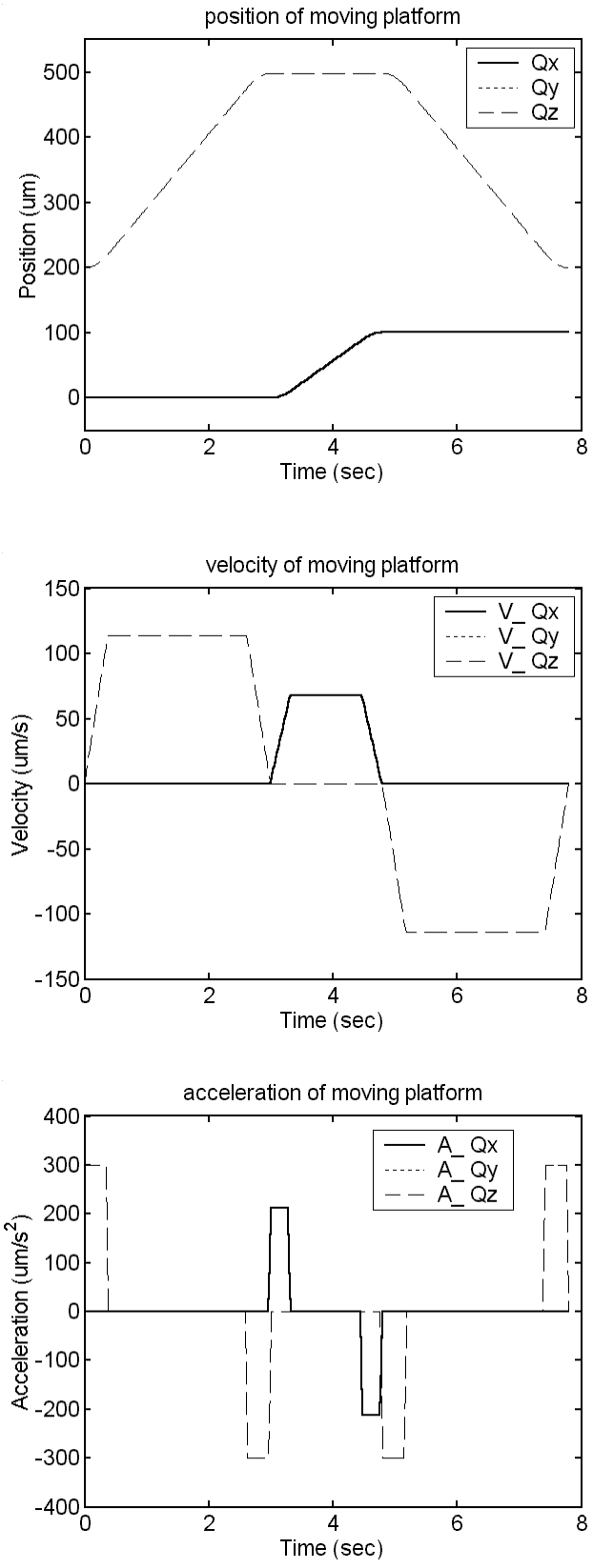

Figure 3.30: Trajectory of the moving platform in 3-D space.

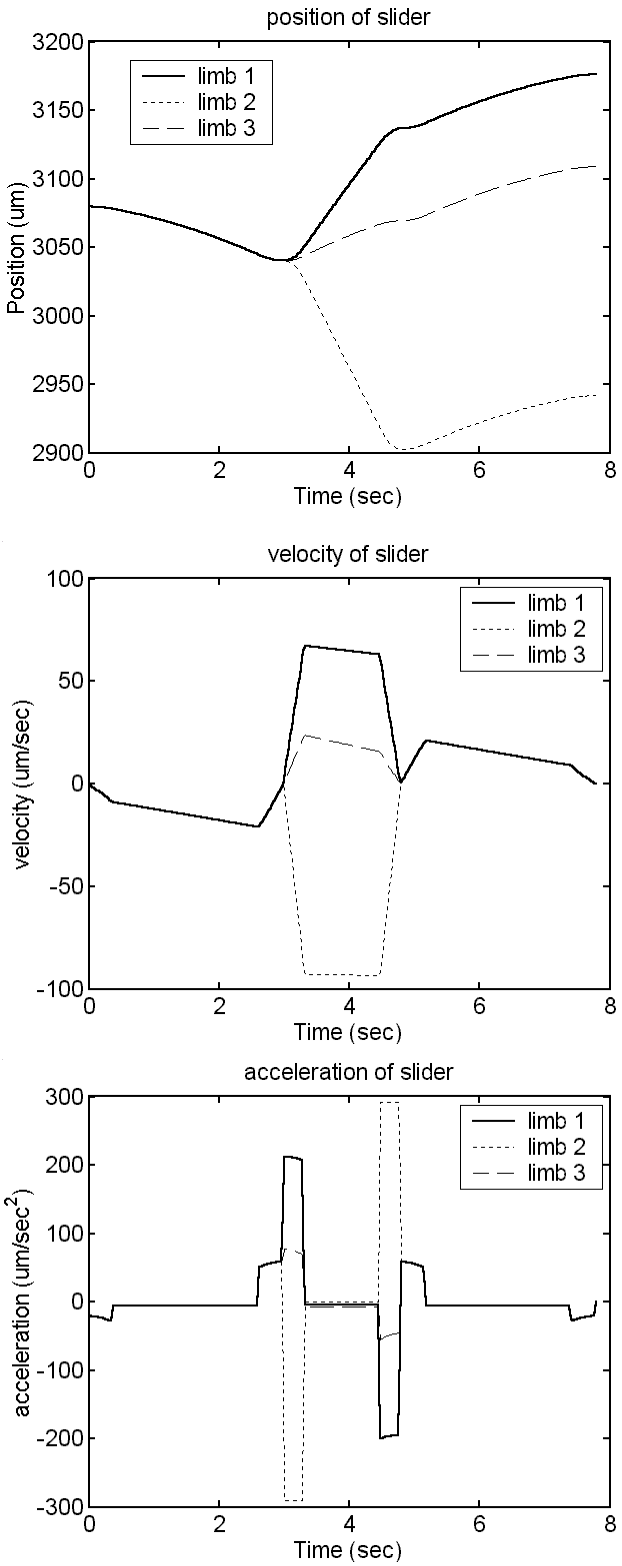

Figure 3.31: Position, velocity, and acceleration of each slider on the manipulator during the moving platform following the desired trajectory.

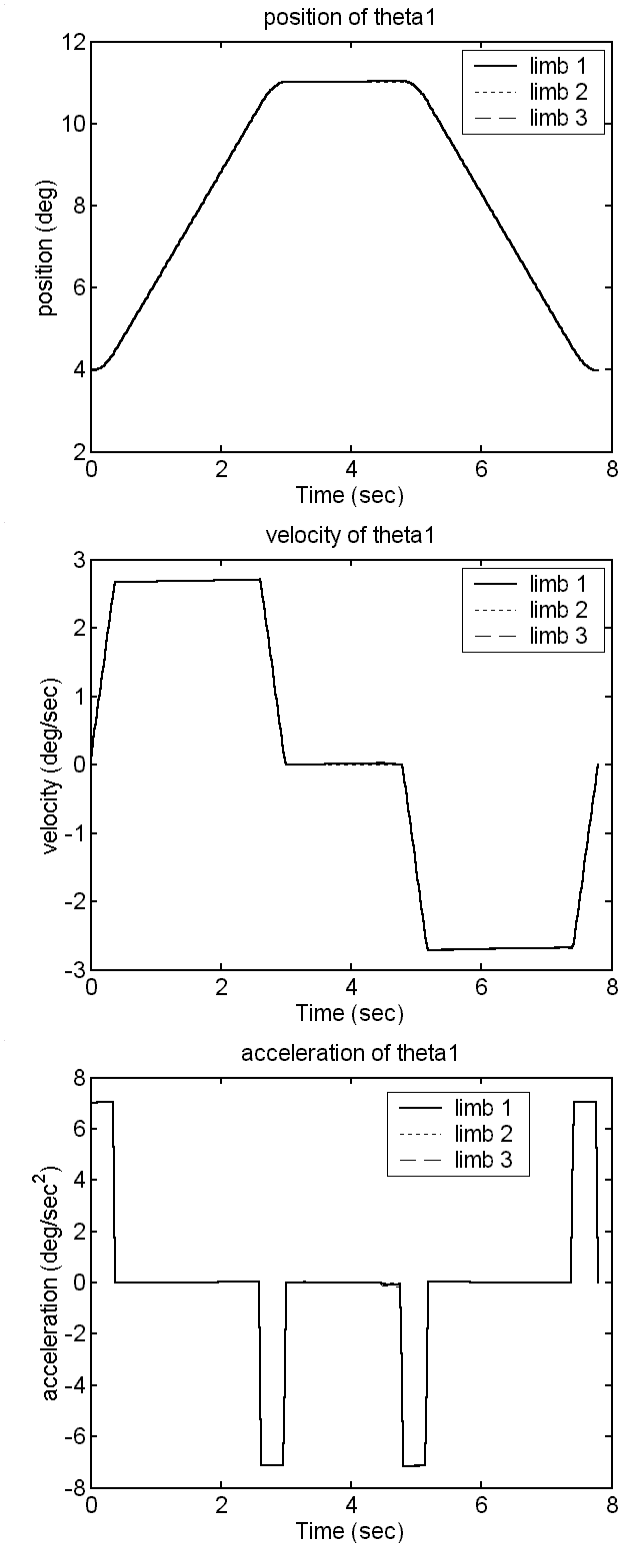

Figure 3.32: Position, velocity, and acceleration of θ_1 on each limb of the manipulator during the moving platform following the desired trajectory.

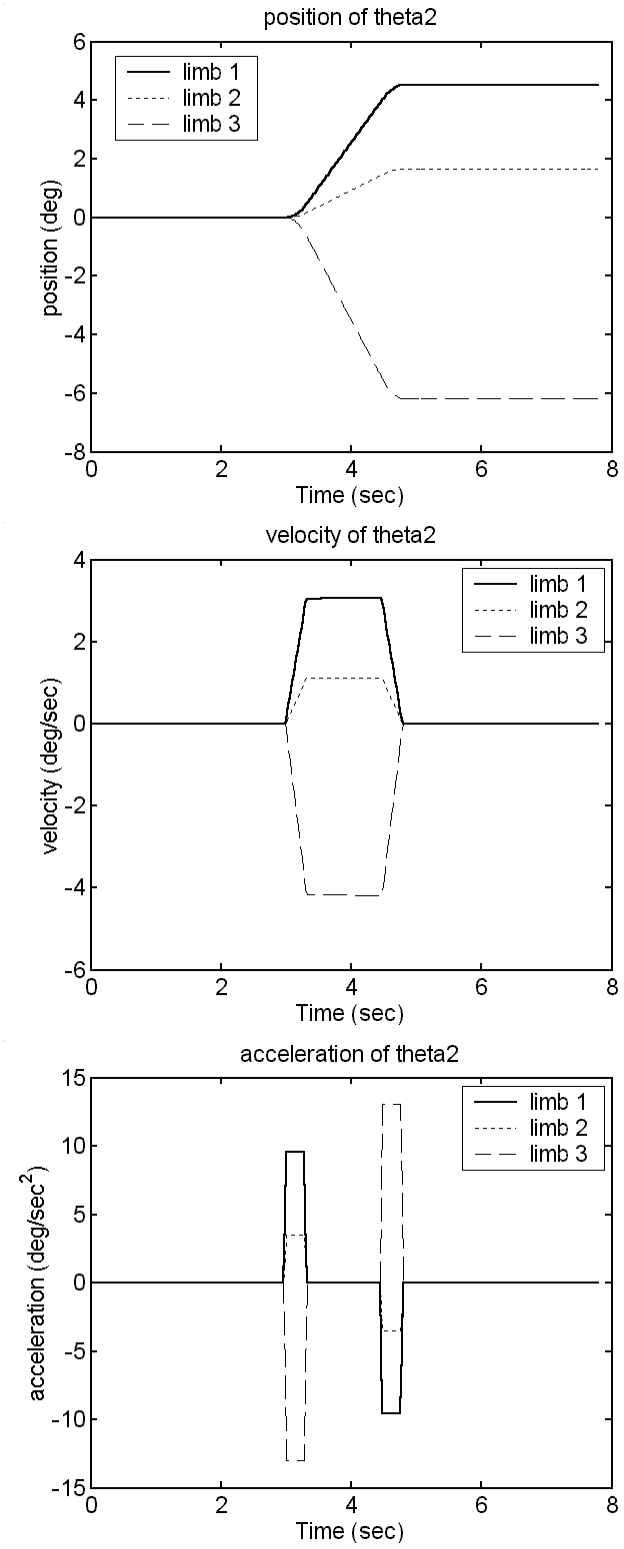

Figure 3.33: Position, velocity, and acceleration of θ_2 on each limb of the manipulator during the moving platform following the desired trajectory.

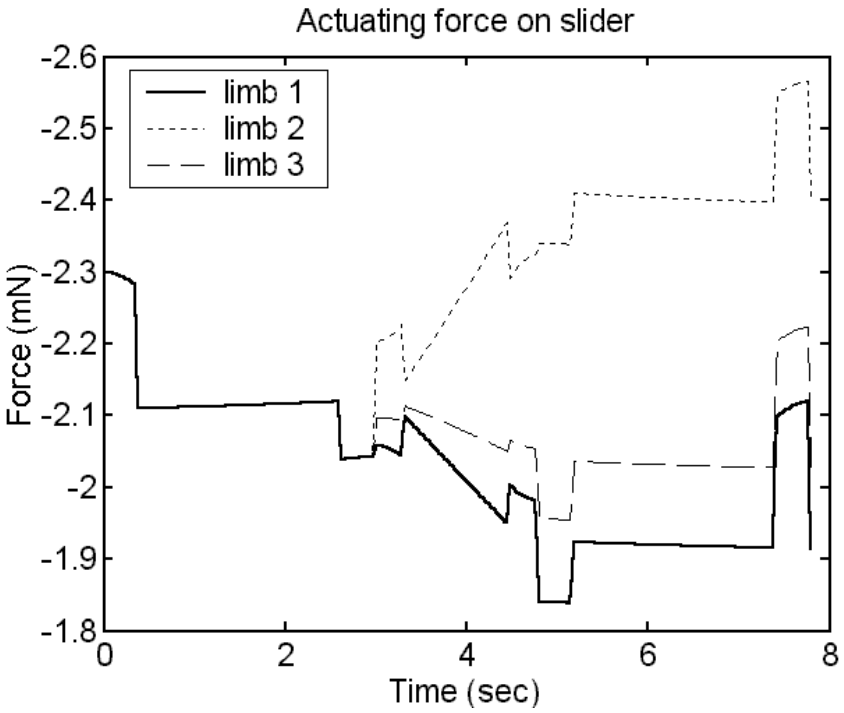

Figure 3.34: Force on each slider of the manipulator during the moving platform following the desired trajectory.

Table 3.2: Manipulator's design parameters used in the numerical dynamics simulation.

$L_1 = L_3 = 425$ um	$a = 30$ um	$m_p = 0.10776$ mg
$L_2 = 1500$ um	$b = 63.75$ um	$m_c = 0.029783$ mg
$L_g = 115$ um	$c = e = 588.75$ um	$m_s = 0.18001$ mg
$L_h = 505.5$ um	$d = 1275$ um	$E = 195$ Gpa
$t_p = 30$ um	$f = 569.25$ um	$I = 2500$ um^4
$\gamma = 0.85$	$K_\Theta = 2.65$	$g = 9.8$ N/m^2
$\phi_1 = 90$ deg	$\phi_2 = 210$ deg	$\phi_3 = 330$ deg

Chapter 4

Design Optimization

4.1 Thermal V-beam Optimization

The geometry of thermal V-beam affects its output performance, including the displacement of the actuator, the output force of the actuator, and frequency response. In this section, a design strategy for thermal V-beam actuator is discussed. By using the pseudo-rigid-body model described in the section 3.2, the geometry and dimension of V-beam can be optimized to fit the design requirements. For the general opinions in the same power input, the longer V-beam produces larger free-loading displacement but less output force, the larger offset angle in V-beam generates larger output force but less displacement, and the thicker or wider V-beam creates larger output force but less displacement. Therefore, a trade-off exists between displacement and force.

The power consumption is another important design issue. An excellent design should contain good performance and power saving. Because the material properties are temperature dependent, the numerical method mentioned in the section 3.2.4 is used to evaluate the performance of thermal actuator in per unit power. This performance index is computed as the total displacement or force on the thermal actuator divided by the total consumption power. Since V-beam is symmetric on the yoke of actuator and only a half beam is considered in the model analysis, the total power consumption, P_c, on the whole V-beam can be obtained by doubling the power consumption of a half beam, that is,

$$P_c = 2\sum_{i=1}^{n} J^2 \rho_i(T) whL_i \tag{4.1}$$

where $\rho_i(T)$ is the temperature dependent resistivity of nickel from Eq.(3.21) in the small divided element *i*, L_i is the length of the small divided element *i*. Figure 4.1 and Figure 4.2 display the performance on displacement and force per unit power based on different V-beam dimensions with a fixed offset angle. Furthermore, Figure 4.3 and Figure 4.4 exhibit the performance on displacement and force per unit power based on different V-beam geometry for various offset angles but the same length.

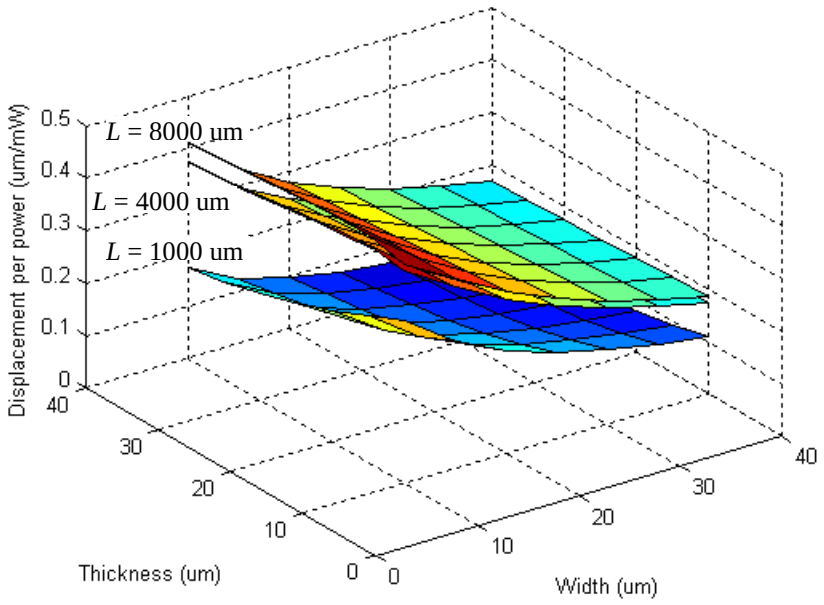

Figure 4.1: Displacement performance per unit power on different V-beam dimensions (offset angle = 3 deg).

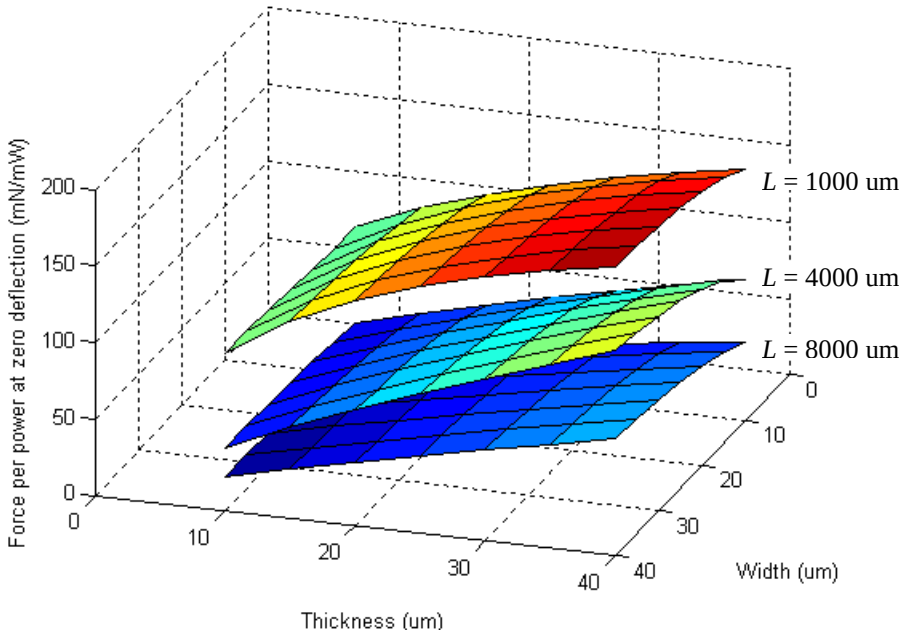

Figure 4.2: Force performance per unit power on different V-beam dimensions (offset angle = 3 deg).

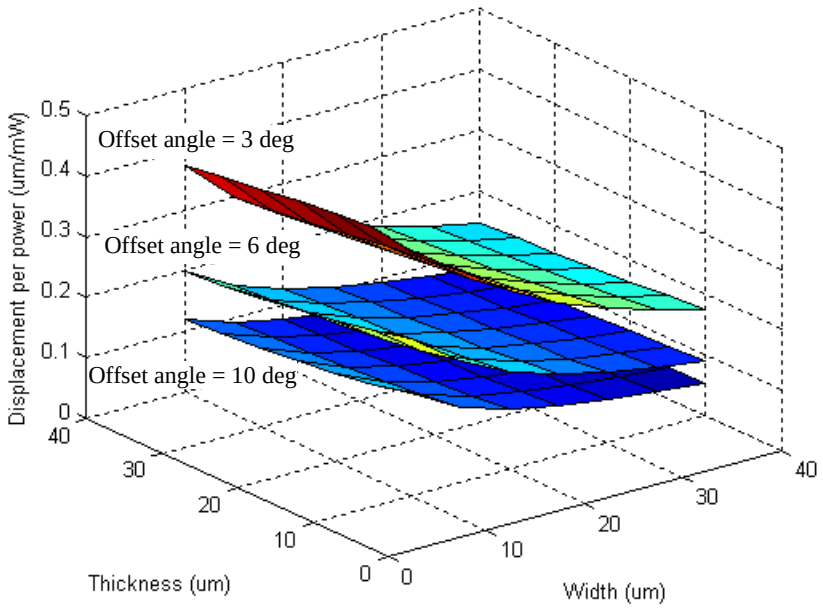

Figure 4.3: Displacement performance per unit power on different V-beam geometry (*L* = 4000 um).

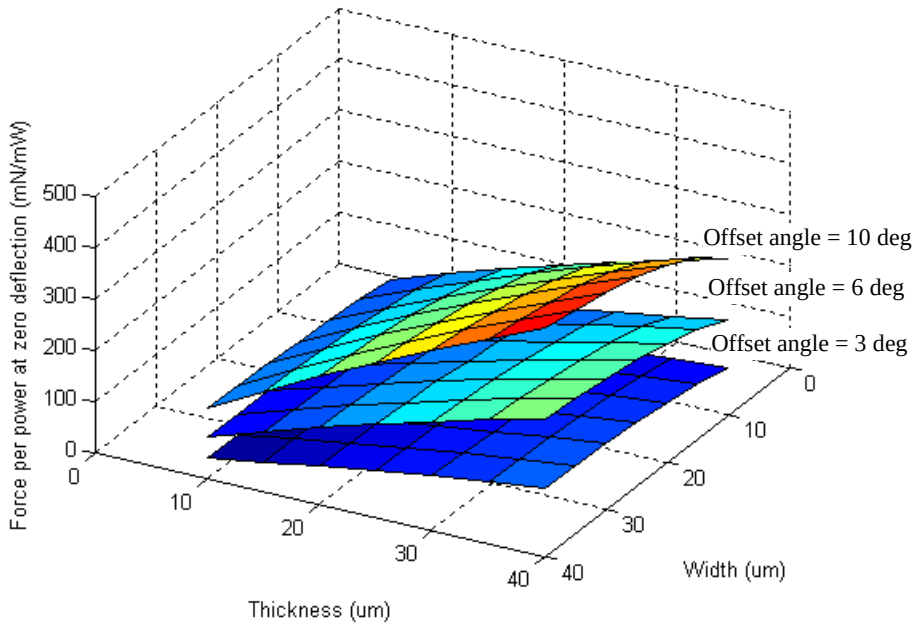

Figure 4.4: Force performance per unit power on different V-beam geometry (*L* = 4000 um).

According to the above four charts, the V-beam width should be made as small as possible to increase its displacement without sacrificing much force, especially in the condition of a small offset angle. At an offset angle equaling 3 degrees, the changing rate of displacement performance curve in Figure 4.3 alters more than others as the beam width decreases in the condition of a specific beam thickness, but the changing rate of the force performance curve in Figure 4.4 keeps almost the same. Meanwhile, when the V-beam thickness increases, the force performance shown in Figure 4.4 is also improved without losing displacement performance. The smaller V-beam width and larger V-beam thickness have the same performance effects in Figure 4.1 and Figure 4.2. When the V-beam length doubles from 4000 um to 8000 um, the displacement performance shown in Figure 4.1 does not improve a lot. Therefore, to save the actuation power and

simultaneously own good performance, the thinner, thicker, shorter thermal V-beam and the smaller offset angle are desirable design strategies. Additionally, if a very small offset angle is used on the thermal V-beam actuator, buckling effects dominate the most conditions of deformation and cause erratic actuation. Based on the experiment, the offset angle should not be below 3 degrees to eliminate the erratic actuation. On the other hand, Since temperature controls the amount of thermal expansion that proportionally generates the deflection and force of the actuator, the changing distributed temperature of the V-beam, caused by some other factors, can affect the actuator performance. Based on Eq.(3.3), in the condition of fixed input power applying on the same dimension V-beams, increasing the air gap between V-beams and substrate, running the actuators in a vacuum chamber, or both, is a good choice to increase the V-beam temperature and to improve the performance.

4.2 Optimization on the Workspace of Micromanipulators

The workspace of a manipulator is defined as the volume of space that the end effector can reach [1]. In the designed parallel manipulator, the end effector is located at the center point ***Q*** of the moving platform. Two different definitions are available for the workspace. A reachable workspace is the volume of space within which every point can be reached by the end effector in at least one orientation. A dextrous workspace is the volume of space within which every point can be reached by the end effector in all possible orientations. Obviously, the dextrous workspace is a subset of the reachable workspace. However, in my case, these two workspaces are the same because the manipulator is a pure translational movement without considering its orientation.

The volume of manipulator workspace can be estimated from various methods. Integrating each differential volume for a specific zone through the whole workspace is one approach. However, due to the complexity of the manipulator, it is difficult to define the integration limits for each zone. A simple approach is to use a numerical technique to approximate the real volume of the workspace. The Monte Carlo method [2], as shown in Figure 4.5, uses a huge amount of random points to determine what proportion of points is within the workspace and then obtains an estimative volume of the workspace. To acquire the proportion and figure out the shape of the workspace without considering the dimension of the manipulator, a normalized coordinate is used to describe the workspace. Figure 4.6 demonstrates the configuration of the manipulator on XY plane in the normalized coordinate system. The total length of each limb in the manipulator, which is the distance between the platform center and the slider edge (L_1+L_2+L_3+2L_g+L_h in Figure 3.28), is used as the unit length in the normalized coordinate system. It is critical to develop a performance index for the manipulator workspace. According to Lee-Yang theorem [80], the workspace performance index, *PI*, of the manipulator is defined as

$$PI = \frac{V_w}{L_{eff}^{\ 3}} \tag{4.2}$$

where V_w is the workspace volume and L_{eff} is an effective total link length of the manipulator. For this parallel manipulator, the effective length is equal to the distance between the platform center and the slider edge plus the total travel of the slider.

Using the design parameters in Table 3.2, the shapes of the workspace based on the different limits of joints are displayed in Figure 4.7 to Figure 4.10. The workspace performance indices from Figure 4.7 to Figure 4.10 are calculated as 0.000514, 0.00324, 0.0114, and 0.0113, respectively. According to the above index results, the larger travel

limit of the slider creates, the bigger workspace generates. Moreover, the backward movement of the prismatic joint also has a great effect on the workspace volume. However, the rotating limits of the compliant joints do not affect the workspace very much. The future work is to find the optimal design on maximizing the workspace of this manipulator.

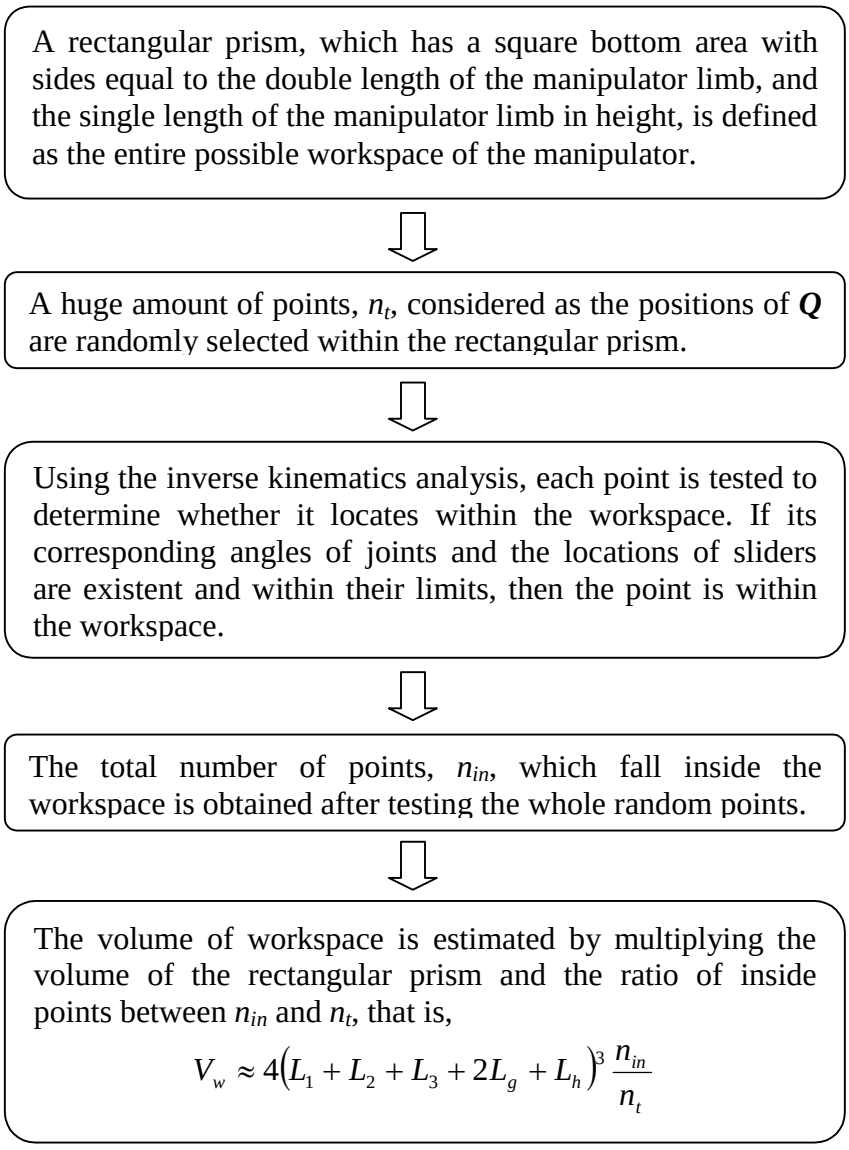

Figure 4.5: Procedure of Monte Carlo method used to estimate a volume of the workspace.

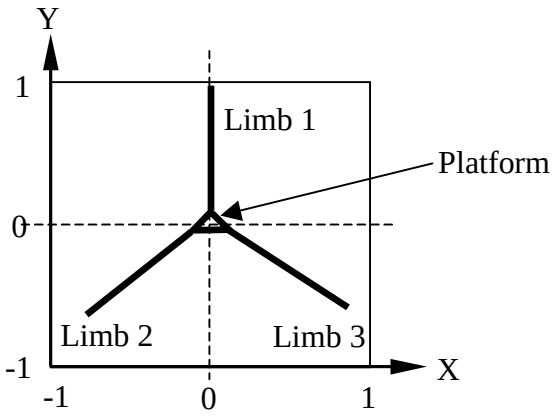

Figure 4.6: Configuration of a manipulator on the XY plane in the normalized coordinate system.

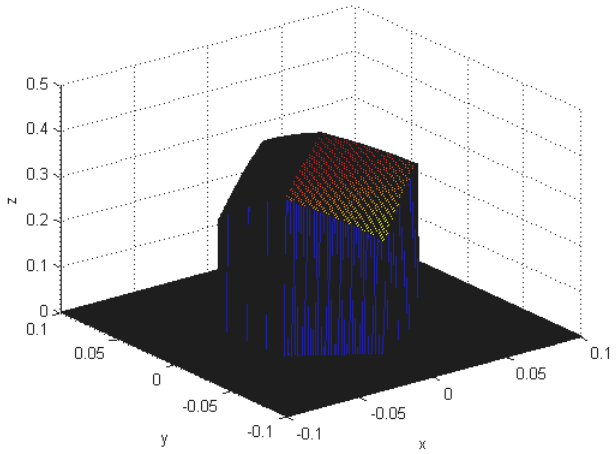

3D workspace

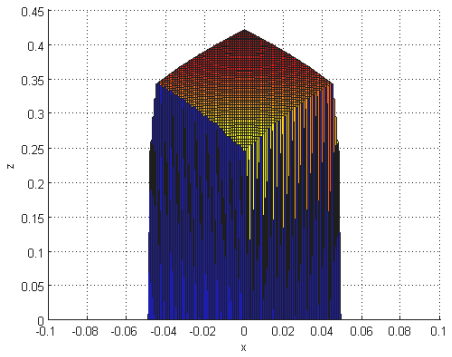

Side view of workspace

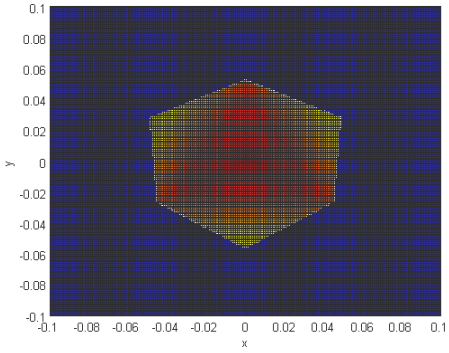

Top view of workspace

Figure 4.7: Workspace shape of the manipulator with Slider limit: 0 ~ 500 um, Out-of-plane joint limit: 0 ~ 60 deg, and In-plane joint limit: -60 ~ 60 deg.

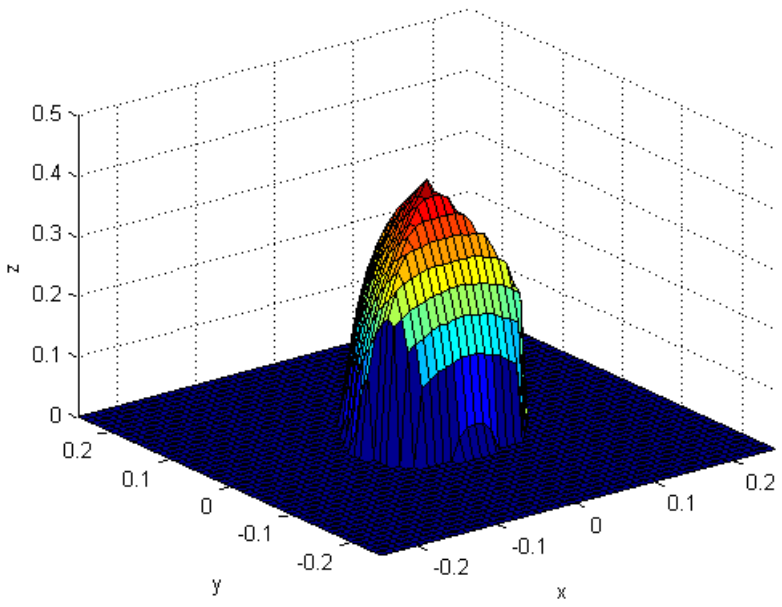

3D workspace

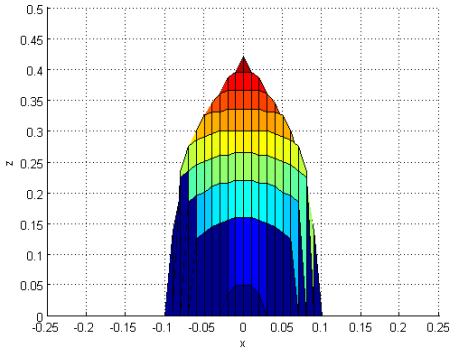

Side view of workspace

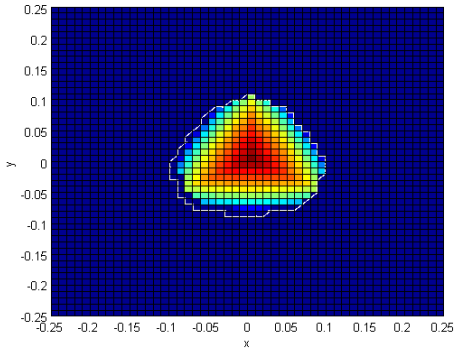

Top view of workspace

Figure 4.8: Workspace shape of the manipulator with Slider limit: -500 ~ 500 um, Out-of-plane joint limit: 0 ~ 60 deg, and In-plane joint limit: -60 ~ 60 deg.

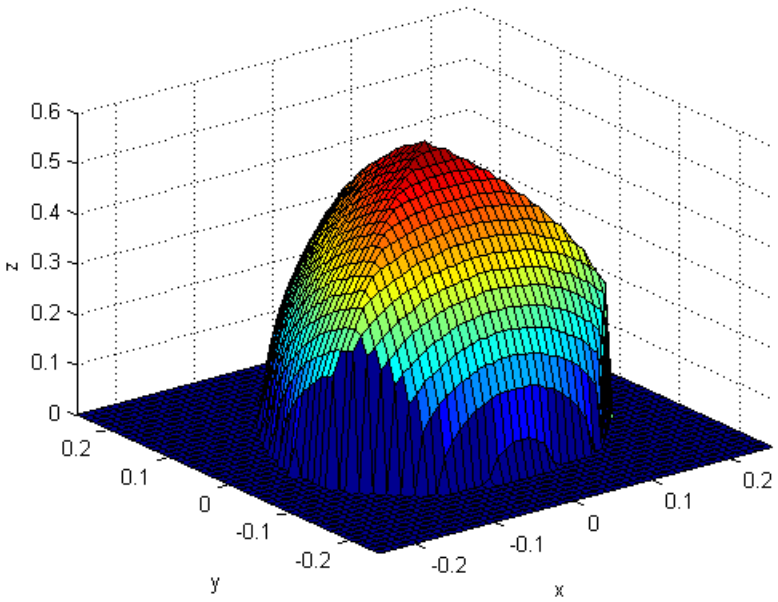

3D workspace

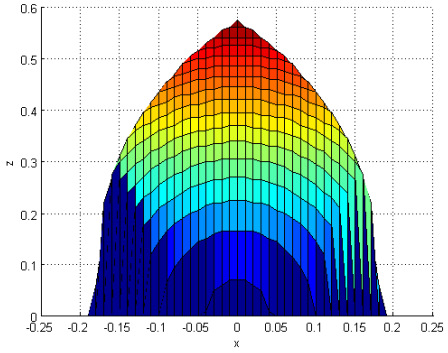

Side view of workspace

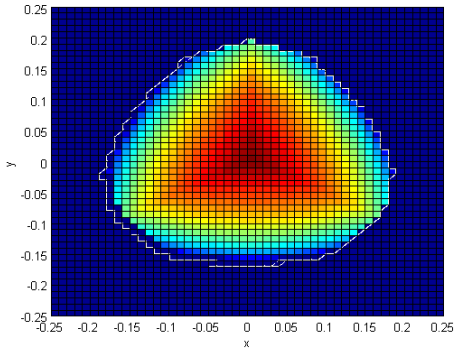

Top view of workspace

Figure 4.9: Workspace shape of the manipulator with Slider limit: -1000 ~ 1000 um, Out-of-plane joint limit: 0 ~ 60 deg, and In-plane joint limit: -60 ~ 60 deg.

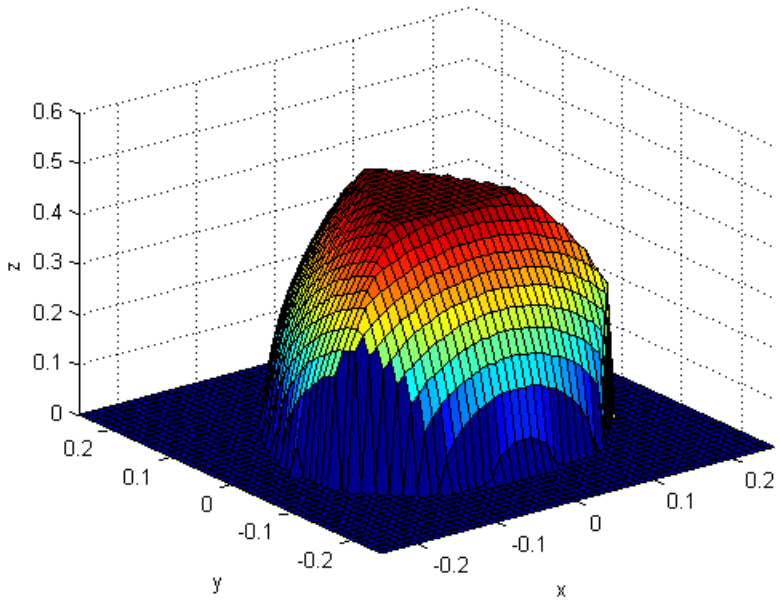

3D workspace

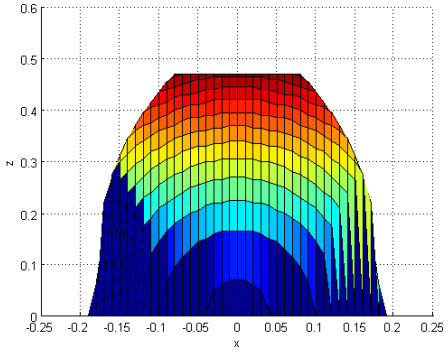

Side view of workspace

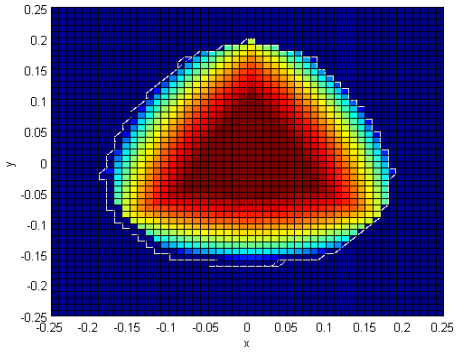

Top view of workspace

Figure 4.10: Workspace shape of the manipulator with Slider limit: -1000 ~ 1000 um, Out-of-plane joint limit: 0 ~ 30 deg, and In-plane joint limit: -30 ~ 30 deg.

4.3 Design Strategy

The whole manipulator discussed in this research can be separated into three main parts as presented in the section 3.1. The whole design procedure is demonstrated in Figure 4.11. First, the degree of freedom and the workspace of a spatial mechanism should be considered as main design factors. After the dimension and the configuration of the mechanism are determined, using dynamic analysis described in the section 3.6 can simply estimate the maximum actuation force for the designed mechanism on its desired trajectory.

The thermal linear motor, an actuator for driving the designed mechanism, is the next design subject. Once the linear motor design is finished, that is, the wedge angle, the wedge dimension, and the location of the four-pair actuators are determined, then the required actuator deflection, d_r, for reaching the tooth bottom can be decided. It is anticipative to have enough force to drive the slider during the loading generated from the mechanism. In order to overcome the maximum force from the mechanism, the required actuation force delivered from the thermal actuator, F_r, can be obtained from the linear motor force analysis in the section 3.4. In the analysis, F_s in Eq.(3.25) is equal to the maximum actuation force, and F_n is equal to the above required force, F_r.

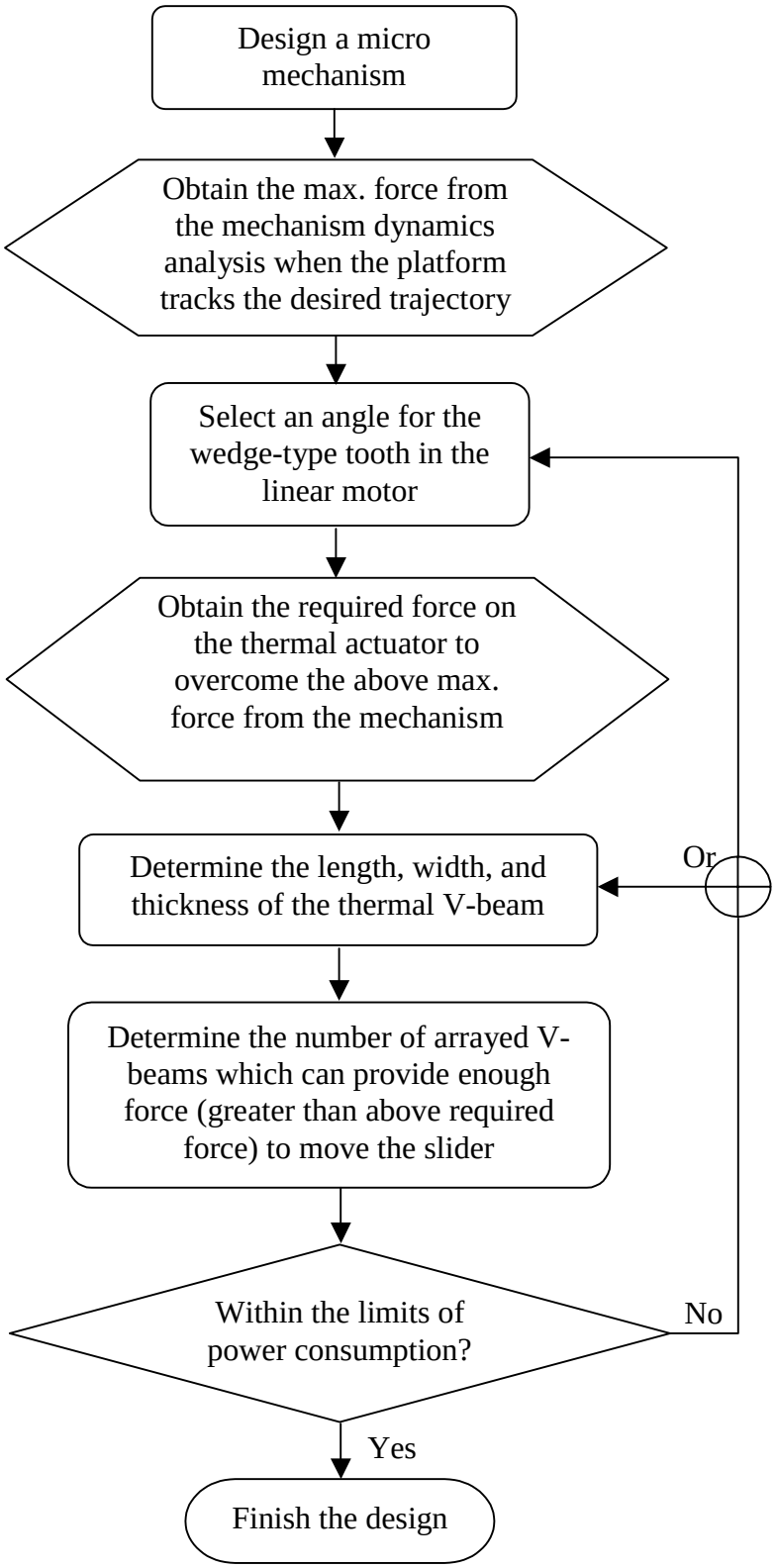

Figure 4.11: Design flowchart of the whole parallel micromanipulator.

The thermal V-beam actuator, a power source inside the linear motor, is the next design topic. Parallel V-beam array will provide enhanced force by multiplying the number of arrayed V-beams with the force generated from a single pair, and it keeps almost the same displacement as a single pair V-beam. This can be observed from the experimental data in Figure 3.19 and Figure 3.20 if different numbers of arrayed V-beams actuate in equimultiple input currents. In general, any designed thermal V-beam should have the maximum operational displacement determined from the V-beam temperature with a fixed input current. Because high temperature will soften the nickel V-beam and greatly drop the output force, the temperature should not exceed 600^{o}K (below Curie temperature of nickel) to prevent the V-beam from permanently deforming and damaging due to the beam's softening. In the design strategy, this maximum operational displacement should at least double the required displacement because the available force is proportional to the difference between the maximum operational displacement and the displacement of the thermal actuator as mentioned in the section 3.2.3. For example, if the required displacement in the thermal V-beam is d_r, then the maximum operational displacement for this V-beam in a free loading condition should need at least $2d_r$. Based on the above optimization discussion about thermal V-beams, the optimal values of the design parameters for thermal V-beams, such as an offset angle (3 degrees), the thinnest width successfully fabricated in UV-LIGA process (10 um), and the largest thickness successfully fabricated in UV-LIGA process (40 um), can be initially selected to decide the length of V-beam, so that this thermal V-beam can provide the maximum operational displacement of $2d_r$ within the specific temperature, 600^{o}K. The number of arrayed thermal V-beams can be acquired by total required force, F_r, divided the single-pair

output force at the required deflection. Next, the total current consumption is calculated by the above current, which applies on V-beam to produce the displacement of $2d_r$, multiplying the required number of arrayed V-beams. This total current consumption can also transform into the consumption power. If the total current or power consumption exceeds the source of power supply, then the dimension of the thermal V-beam or the angle of wedge in the linear motor needs to reconsider and modify until all design parameters fit the whole requirement.

For example, recalling the numerical example on the dynamic analysis in the section 3.6.2, the maximum force for actuating the designed mechanism along the desired trajectory is about 2.57 mN. If the angle of wedge-type tooth is selected as 30^o, then the force, which is generated from the thermal actuator to overcome the above maximum actuation force from the mechanism, is 2.05 mN when the coefficient of friction between the both contact teeth is 0.53 [81]. Besides, the necessary deflection for the thermal actuator is about 35 um if the total travel of one tooth is 20 um. Then the maximum operational displacement of the thermal V-beam should be at least 70 um. After the thermal V-beam, which has 10 um in width, 40 um in thickness, and 3 degrees in an offset angle, runs the numerical analysis in the thermodynamics discussed in the section 3.2, the total length of V-beam is selected as 3300 um for providing the maximum displacement of 70 um under the safe operational temperature. Now, according to the above selected dimension of V-beam, the supplying force is 13.82 mN when the displacement of the thermal V-beam reaches 35 um at the current 0.485 A under the loading condition. Hence the required number of arrayed V-beams is one, and the total consumption power is 0.25 W under the total input current of 0.485A. The whole design

process is finished if the total consumption power satisfies the design requirement or the power supply's limits.

Chapter 5

System Integration

5.1 Introduction

After the parallel micromanipulator is fabricated, the electrical wires need to connect its bond pads to communicate with the outside control system. Then the control signals can be inputted through the wires to actuate the thermal motor and drive the mechanism. In this research, the LabVIEW (Laboratory Virtual Instrument Engineering Workbench) from National Instruments^{TM} is very convenient to be a control system. This software can generate and detect the signals when it works with data acquisition card. Moreover, its graph user interface (GUI) and graphical programming language, rather than textual language to describe programming actions, provide more convenience to create the control panel. In the following sections, the control signals and the whole system setup will be discussed.

5.2 Control Interface Using LabVIEW

5.2.1 Linear Motor Control Strategy

The linear motor drives the prismatic joint or the slider of the micromanipulator by two kinds of motion - a forward motion and a backward motion. In the free loading condition, the linear motor can simply use one of two independent thermal actuator systems shown

in Figure 3.4 to control the forward or backward motion. However, in the loading condition, using only one system may not be enough to control the slider motion in the linear motor. When the slider of the linear motor moves forward to raise the manipulator platform and bend the compliant joints, the elastic storage energy on the compliant joints is produced. Thus, if the pushing force transferred from the thermal actuator disappears, the slider of the linear motor will spontaneously move back to the original place enabling the compliant joints to return their original shape. The saw-toothed impactor attached in front of the thermal actuator can simultaneously provide the lock and push actions on the slider, but it only produces both actions in one direction. In the backward slider motion and the loading in the same direction of movement, if the thermal actuators used in the backward system are individually actuated, the recovery force delivered from the compliant joints will push the slider back until it is locked by some teeth. Figure 5.1 is a snapshot of the beginning backward motion when the slider actuation direction is suddenly changing. Therefore, the lock motion is necessary to stop the spontaneously backward movement caused by the recovery force when the pushing force created in the forward motion disappears. During the backward slider motion, reversing the triangular wave signal used in the forward motion (Figure 5.2) is the best method to provide the actuator with such lock motion. Simply put, using the reverse forward motion displays the backward motion. In other words, if the actuation signal in the left hand side of Figure 5.2 is used for the forward slider movement in the forward thermal actuator, then its reverse signal shown in the right hand side of Figure 5.2 is used for the backward slider movement in the same thermal actuator.

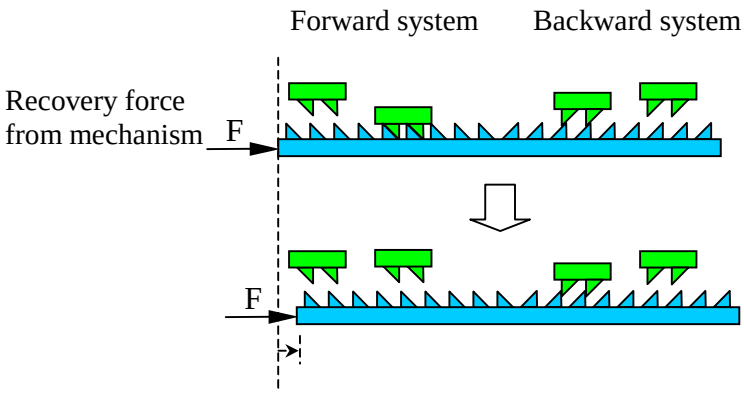

Figure 5.1: Moment of changing the slider actuation direction without the lock motion during the front loading.

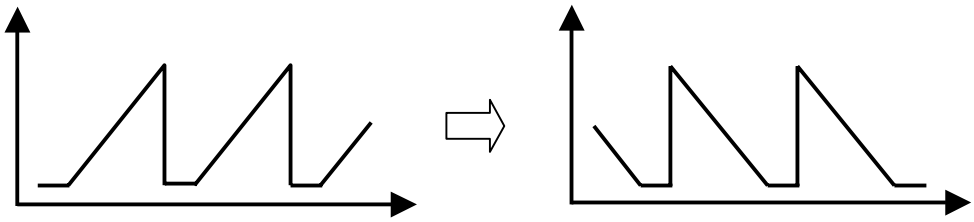

Figure 5.2: Signal (right) used for the same thermal actuator by reversing the original actuation signal (left) when the actuation direction changes.

Since the thermal actuators used in the forward motion already provide the lock motion to prevent retrogression caused by the front-loading at the slider end, the forward slider motion can be produced by simply using the two pairs of thermal actuators in the loading condition. For the backward slider motion, the simplest way is to use the reverse signals for the same two pairs of actuators as mentioned above and let the recovery force automatically push the slider back. However, four pairs of the thermal actuators can work better to provide the active pulling force on the slider. The operation sequence of the

backward movement of the linear motor, driven by four pairs of the thermal actuators, is illustrated in Figure 5.3. The left side of this figure demonstrates the control signals for four pairs of the thermal actuators. The bottom of four control signals is the combination of those four signals to show the state of overlapping signals. The right hand side of this figure illustrates the operation sequence of the corresponding sections on the left. Due to the symmetry of the linear motor, half part of the linear motor is drawn here to demonstrate the operation sequence. In order to keep continuous motion on the slider, overlapping the actuation signals is necessary, as shown the area between two adjacent dashed lines in Figure 5.3. In other words, before one pair of thermal actuators moves back to its original place at the actuation voltage from V_m to 0, another pair must contact the saw-toothed slider to prevent the retrogression at the actuation voltage V_c. Here, V_m is the actuation voltage for the impactor teeth to reach the sawteeth bottom limit of the slider, and V_c is the actuation voltage the moment the impactor sawteeth initially contact the slider.

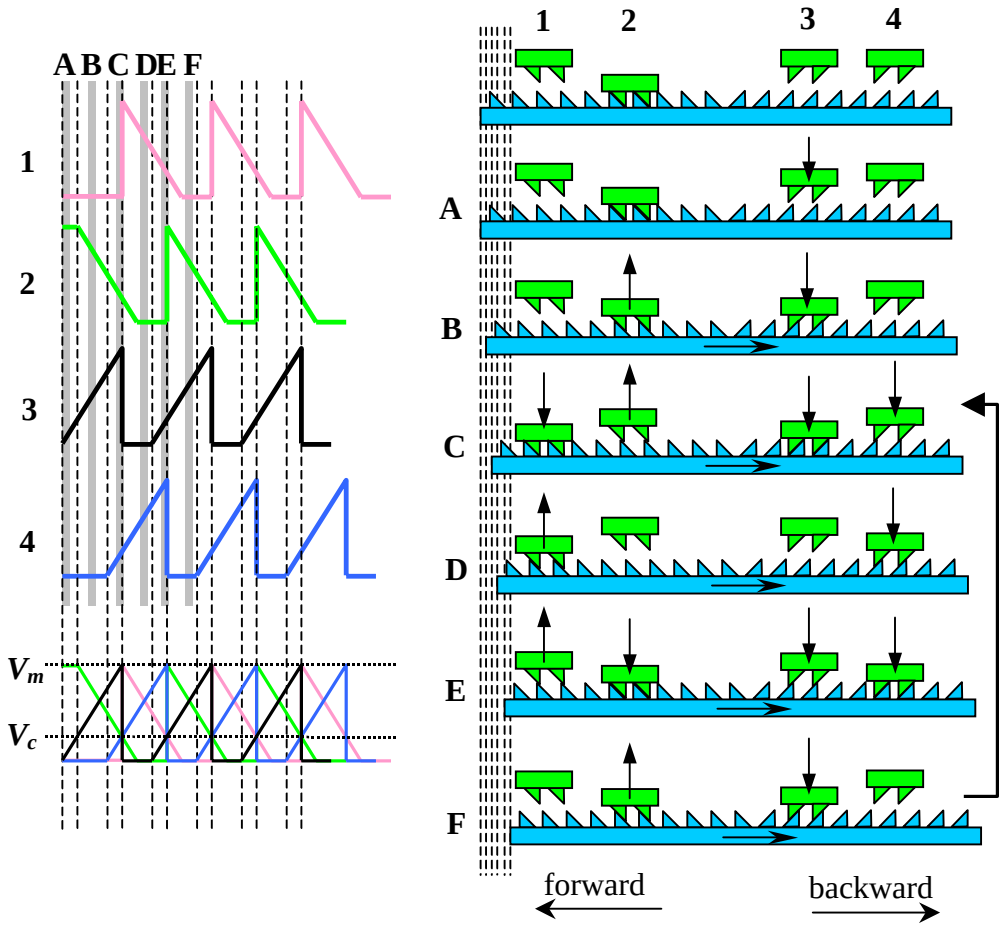

Figure 5.3: Operational sequence of the backward movement in the saw-toothed linear motor.

During the backward slider motion, one pair of the thermal actuators should clamp and fix the slider from the previous forward motion. Here, the pair No.2 of thermal actuators in Figure 5.3 is assumed to be the one to clamp the slider in the final step of the forward motion. First, the pair No.3 of thermal actuators moves to approach the saw-toothed slider as shown in the step A. While the pair No.3 touches the slider at the voltage V_c, the pair No.2 begins to move back. In the step B, the pair No.2 continues to move back so as to release the slider and lock it in the position. Meanwhile, the pair No.3

continuously moves forward to push the slider backward. After the pair No.3 reaches the bottom limit of tooth at the voltage V_m, the pair No.4 takes over the job of the pair No.3 and initially contacts the slider at the voltage V_c. At the same time in the step C, the pair No.2 continuously moves back to reach the critical position of the initial contact at the voltage V_c and the pair No.1 moves to the bottom limit of tooth at the voltage V_m to take over the job of the pair No.2. In the following step D, the motions of thermal actuators are similar to the step B, but the lock motion is provided from the pair No.1 and the active pulling force is from the pair No.4. In the step E, the pair No.3 takes over the job of the pair No.4 to continuously push the slider backward, and the pair No.2 takes over the job of the pair No.1 to lock the slider. The movement of the step F is the same as the step B. Then the cycle of BCDE is repeated to accomplish the continuous backward slider movement.

The similar operation sequence of the forward movement actuated by four pairs of the thermal actuators is displayed in Figure 5.4. However, the pair No.3 and the No.4 are actually redundant because no extra lock motion is necessary to fix the slider position in the forward direction except the circumstance of the rear loading.

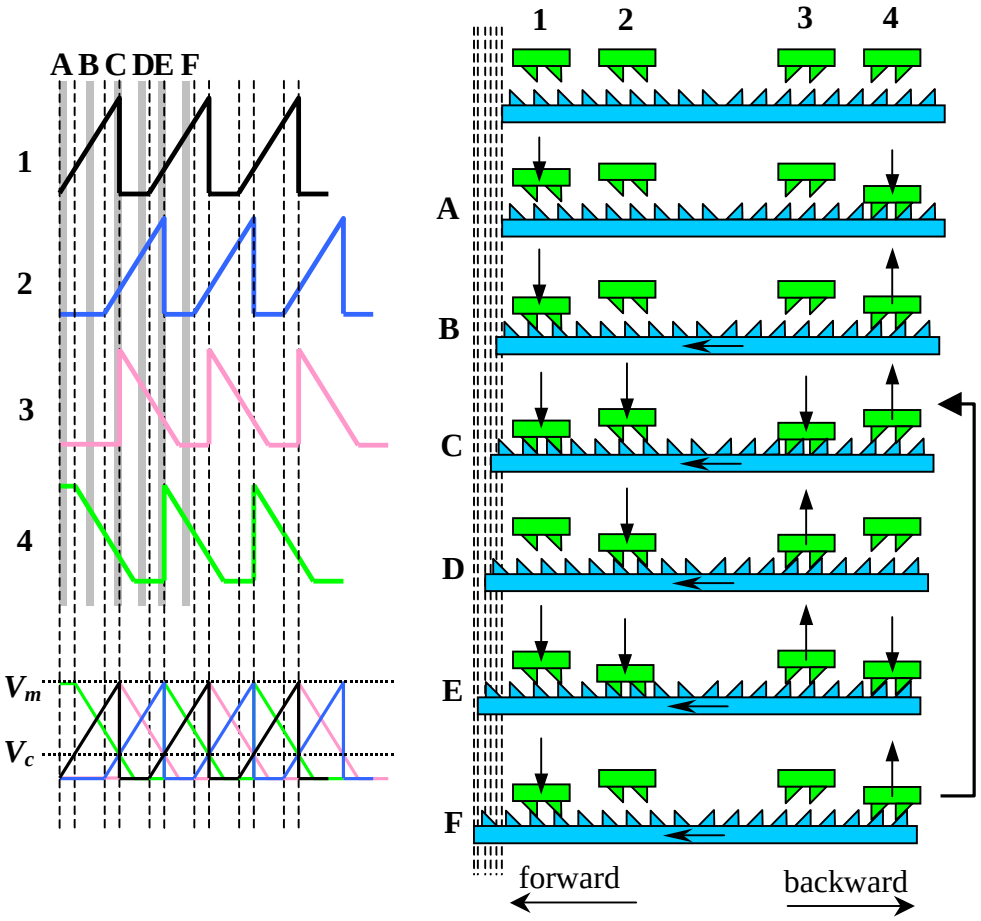

Figure 5.4: Operational sequence of the forward movement in the saw-toothed linear motor.

5.2.2 Actuation Signal Generation Using LabVIEW

As mentioned in the pervious section, triangular wave signals are used as the control signals for the thermal actuators. The advantages of using triangular wave signal are not only its simplicity to reverse as the signal for a changing moving direction, but its slope of the triangular wave signal related to the slider's moving velocity. The slider velocity control takes the characteristic of the linearly proportional relation between the input

voltage of the thermal actuator and its corresponding displacement. For example, on the left side of Figure 5.5 shows the input voltage of the thermal actuator almost linearly proportional to its displacement during the small deformation on the V-beam. The experimental result is based upon the thermal V-beam of 3004 um in length, 11 um in width, 28 um in thickness and 3 degrees in an offset angle. The fitting linear equation and the square of its correlation coefficient, R^2, for the experimental data appear below the trend line. If the linear motor with the tooth angle (θ) of 30^o is controlled at a constant velocity of 1000 um/s, then the variation of the control signal in the time domain looks like the right side of Figure 5.5, which divides the displacement axis by the corresponding perpendicular velocity $1000\sqrt{3}$ um/s on the tooth. The slope *s* of 21.293, the voltage V_m, and the voltage V_c, parameters required by the LabVIEW program to generate the desired actuation signal, are obtained from Figure 5.5 -- *s* from the right side of the figure, and V_m/V_c from the left side according to its corresponding displacement.

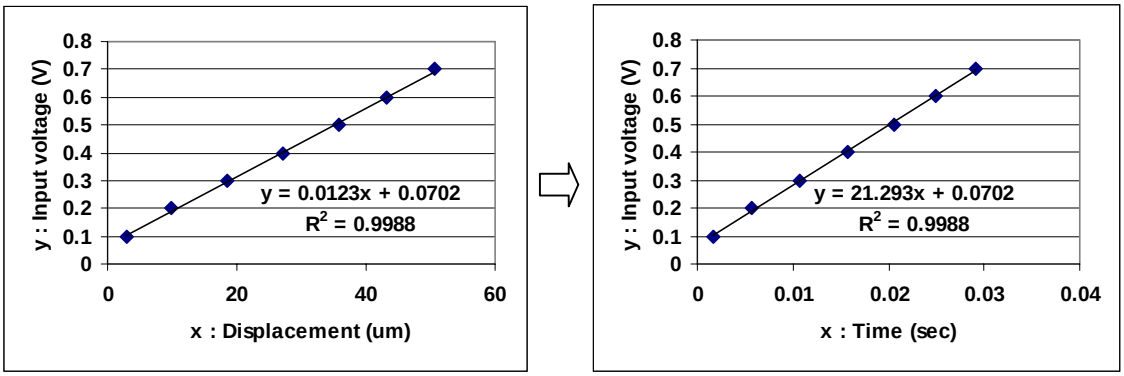

Figure 5.5: Obtaining the slope to build the control signal for doing a constant velocity control from the initially experimental data of the thermal actuator.

However, the slope *s*, the voltage V_m and V_c may be slightly different between each pair of thermal actuators due to different electrical resistances. Assuming V_{m1}, V_{c1}, s_1

and V_{m2}, V_{c2} , s_2 for the two pairs of thermal actuators driving the same slider moving direction, then according to Figure 5.6, the relation of the length can be written as follows:

$$\overline{AC} = \frac{V_{m1}}{s_1} \tag{5.1}$$

$$\overline{BC} = \frac{V_{c2}}{s_2} \tag{5.2}$$

$$\overline{BE} = \frac{V_{m2}}{s_2} \tag{5.3}$$

$$\overline{DE} = \frac{V_{c1}}{s_1} \tag{5.4}$$

$$\overline{CD} = \overline{BE} - \overline{BC} - \overline{DE} = \frac{V_{m2}}{s_2} - \frac{V_{c2}}{s_2} - \frac{V_{c1}}{s_1} \tag{5.5}$$

$$\overline{AD} = \overline{BF} = \overline{AC} + \overline{CD} = \frac{V_{m1}}{s_1} + \frac{V_{m2}}{s_2} - \frac{V_{c1}}{s_1} - \frac{V_{c2}}{s_2} \tag{5.6}$$

$$\overline{AB} = \overline{AC} - \overline{BC} = \frac{V_{m1}}{s_1} - \frac{V_{c2}}{s_2} \tag{5.7}$$

Hence, the parameters of triangular wave signals using for LabVIEW function generator are

Signal 1: Duty cycle = $\frac{\overline{AC}}{\overline{AD}} \times 100\ \% = \frac{V_{m1} s_2}{(V_{m1} - V_{c1}) s_2 + (V_{m2} - V_{c2}) s_1} \times 100\ \%$,

Offset = 0 V, Amplitude = V_{m1}, Phase = 0^o.

Signal 2: Duty cycle = $\frac{\overline{BE}}{\overline{BF}} \times 100\ \% = \frac{V_{m2} s_1}{(V_{m1} - V_{c1}) s_2 + (V_{m2} - V_{c2}) s_1} \times 100\ \%$,

Offset = 0 V, Amplitude = V_{m2},

Phase = $\frac{\overline{AB}}{\overline{AD}} \times 360^{\,o} = \frac{V_{m1} s_2 - V_{c2} s_1}{(V_{m1} - V_{c1}) s_2 + (V_{m2} - V_{c2}) s_1} \times 360^{\,o}$.

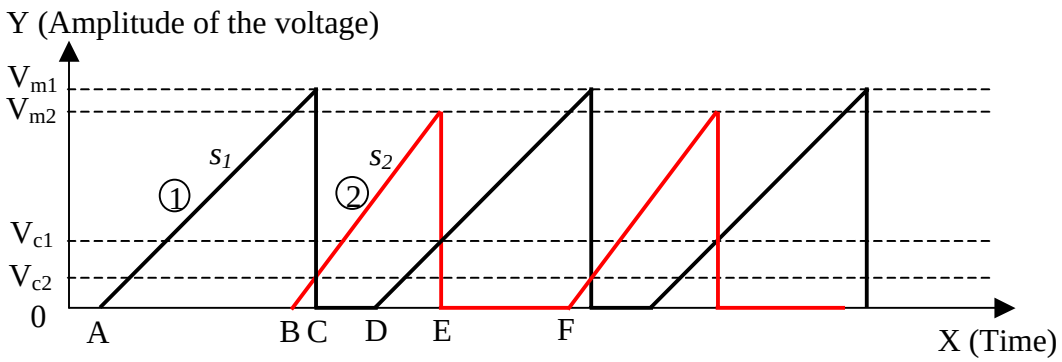

Figure 5.6: Two actuation signals for the two adjacent pairs actuators used in the same slider moving direction.

In ideal design, the electrical resistances, including the inner and the outer electric circuit, should be the same for the two-pair thermal actuators controlling the same slider moving direction. Hence the two key voltages and the slope for these two-pair thermal actuators are the same, that is, $V_{m1} = V_{m2} = V_m$, $V_{c1} = V_{c2} = V_c$, and $s_1 = s_2 = s$. The two signals used for the actuators in the same moving system are shown in Figure 5.7. The parameters of triangular wave signals for LabVIEW function generator are

Signal 1 : Duty cycle = $\frac{V_m}{2(V_m - V_c)} \times 100\,\%$, Offset = 0 V, Amplitude = V_m, Phase = 0^o.

Signal 2 : Duty cycle = $\frac{V_m}{2(V_m - V_c)} \times 100\,\%$, Offset = 0 V, Amplitude = V_m,

Phase = 180^o.

Besides, the frequency of the actuation signal is determined from the desired constant velocity divided by the total travel of one slider tooth.

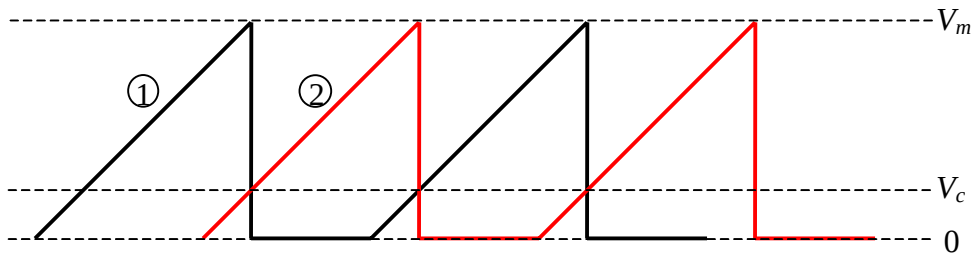

Figure 5.7: Two actuation signals for the two-pair actuators owned by the same moving system in the ideal design condition.

The LabVIEW program has two related parts, the front panel and the block diagram, to generate the signals. The front panel shown in Figure 5.8 displays the user interface as the virtual instrument, including its control constants, a waveform graph, etc. The block diagram is correspondingly graphical codes of the virtual instrument. As described in the previous section, the four pairs of thermal actuators sequentially ignite to smoothly drive the slider. Some logical judgments edited by the LabVIEW program are necessary to determine which pair of the thermal actuators will be the next actuating role. In addition, each whole duty cycle of the triangular wave signal will completely move the total travel of one tooth. However, if a part of the tooth's travel is demanded to satisfy the total accumulated movement on the slider, then the part of signal needs to generate in the final cycle, as shown the signal inside the dotted rectangle in Figure 5.8. For example, if the whole duty cycle of the triangular wave signal can move 30 um on the slider, then one third of that signal can impel the slider about 10 um which is the requirement in the final cycle. Therefore, determining the data length of the signal is very important for doing the accurate position control in the linear motor. Some block diagrams of the LabVIEW program related to this research are shown in Appendix D. A control panel displayed in

Figure 5.8 is used to actuate a linear motor slider to smoothly move about 100 um by its generating signals.

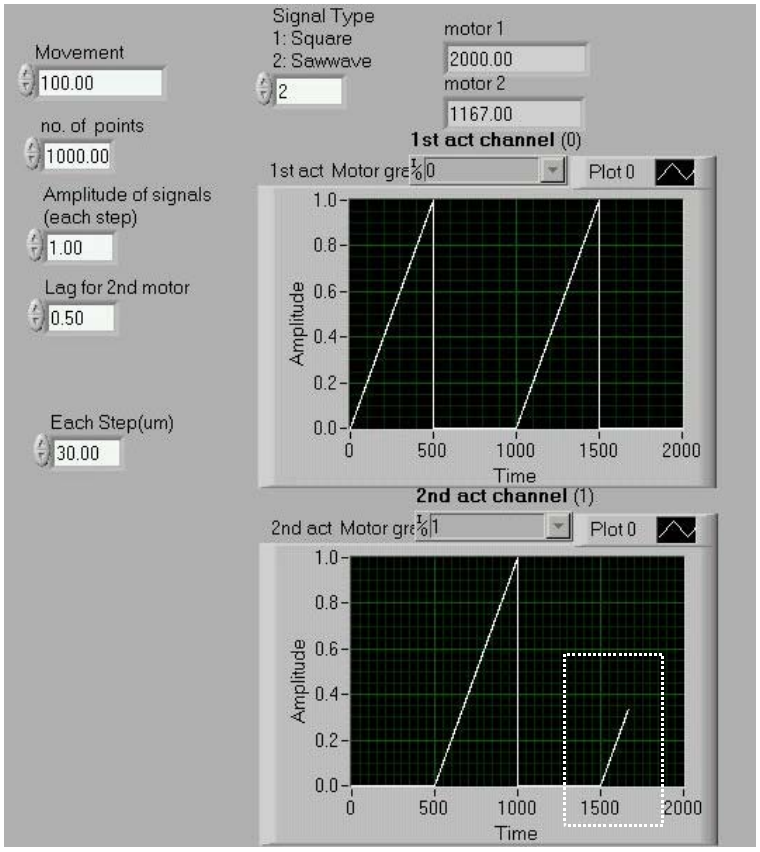

Figure 5.8: LabVIEW control panel used to generate signals for the two pairs of thermal actuators.

5.3 System Setup

For the MUMPs silicon fabrication, the whole dimension of the micromanipulator is small enough to settle on a 1 cm $\times$ 1 cm chip. In order to integrate the LabVIEW control

system with the micromanipulator, the ceramic package and a flat Ribbon cable with a breadboard, as shown in Figure 5.9, are used as an interface to connect the control system and the device. The gold wires used in the Westbond wire bonder machine connect the bond pads between the chip and the ceramic package. The control (actuation) signals created from the LabVIEW program combining with the data acquisition (DAQ) card directly apply to drive the thermal actuators through the corresponding breadboard connecters. The micromanipulator can be placed under the microscope to observe the actuation motion. A setup of the whole system will be like Figure 5.10.

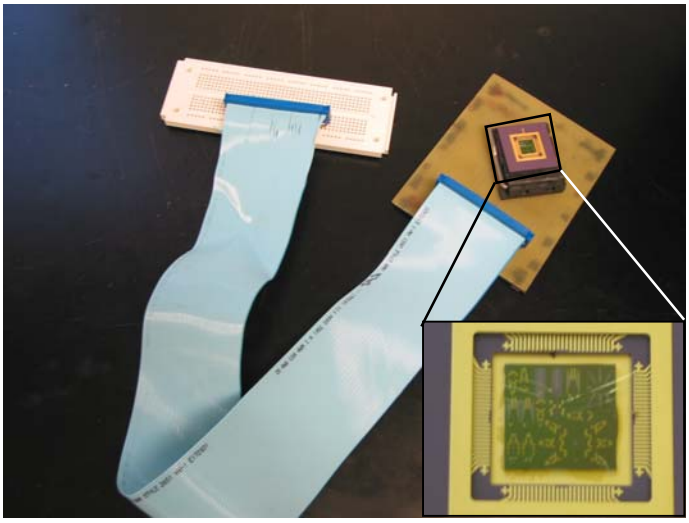

Figure 5.9: Ceramic package with a breadboard used to connect MUMPs devices and the LabVIEW control system.

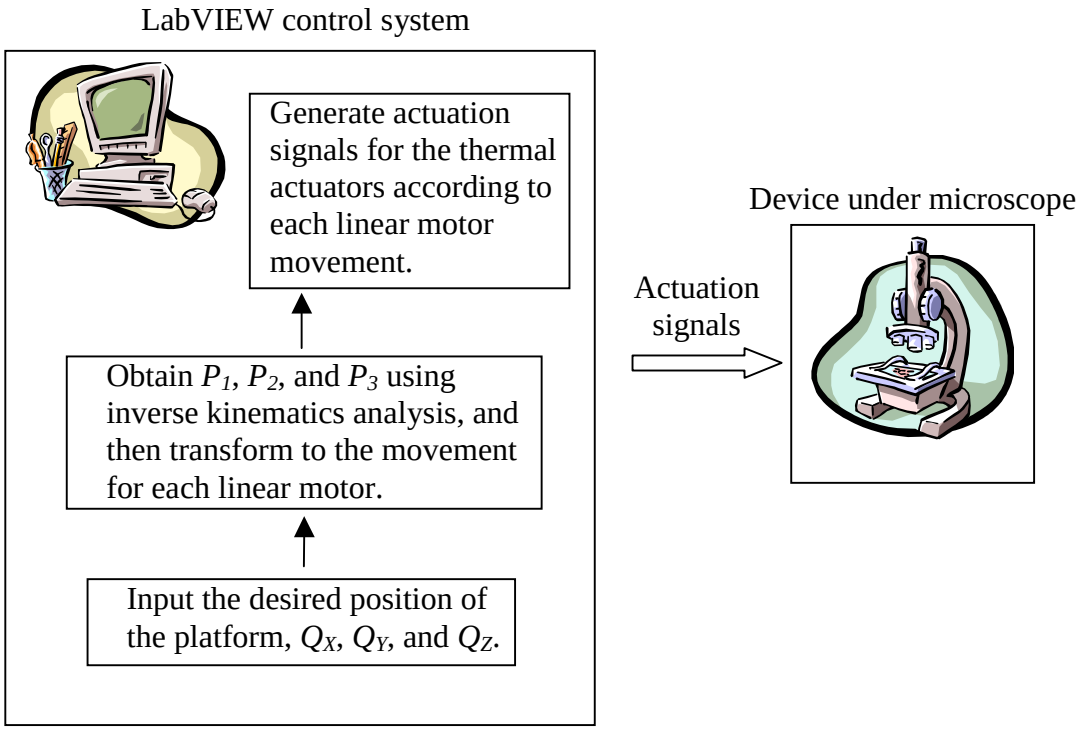

Figure 5.10: Whole system setup for the ideal operation.

For the sake of the micromanipulator fabricated by UV-LIGA process, the electrical resistivity of nickel V-beams is smaller three orders than that of silicon V-beams, and the dimension of the device is also larger than MUMPs process. Thus the device fabricated from the UV-LIGA process requires more power to heat up the nickel V-beam for expanding to produce the necessary deflection. In other words, the much higher actuation current is required to drive the nickel thermal actuator. However, the maximum output current generated from the DAQ card is pretty small in the order of mA, so the power amplifier is an essential tool for amplifying the control signals before they input the device. Furthermore, the LabVIEW program can only directly control the output voltage, and as mentioned above the displacement of the thermal V-beam is linearly proportional to the input voltage. It is convenient to control the deflection of the thermal

actuator as well as the slider displacement by amplifying the current only but keeping the same output voltage after the control signals pass through the power amplifier. Thus using voltage follower is a better choice for this control system. Figure 5.11 illustrates one voltage follower with OPA548T to amplify the current in this research. OPA548 is an operational amplifier for a high current output from Burr-Brown Corporation. The whole system setup is similar to Figure 5.10, but the power amplifier must be mounted between the control signals and the micromanipulator.

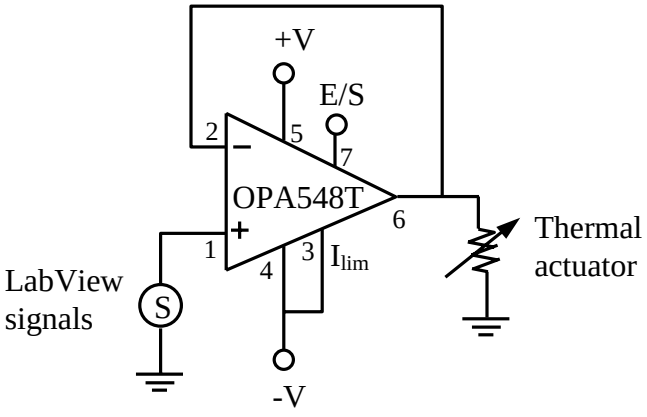

Figure 5.11: Voltage follower used to amplify the operational current.

Chapter 6

Future Work and Conclusions

Contributions

This research demonstrates the following:

- A modified UV-LIGA fabrication process is suitable for micromechanisms development.
- A novel saw-toothed linear motor is able to provide smooth linear motion.
- A pseudo-rigid-body model has been developed to predict the displacement and force of a thermal actuator with experimental agreement within 5 %.
- A pseudo-rigid-body model has been created to simplify compliant mechanism analysis, substantially reducing computational time in kinematic and dynamic analysis.

Conclusions

UV-LIGA process is suitable for fabrication of multiple layered structures. This multi-layered electroplating process has been successfully developed to create a three-degree-of-freedom spatial micromechanism. Comparing to the MUMPs silicon based fabrication process, the UV-LIGA fabrication method provides more benefits such as low cost, flexible fabrication process, etc.

Since the displacement of the thermal actuator is linearly proportional to the input voltage during small V-beam deformations from the experimental data, the slider movement should be also linearly related to that input voltage. Therefore, the motion

resolution of the saw-toothed linear micromotor can become infinitesimal, possible down to nano-meter scale, because the amplitude resolution of voltage is very small. Then the accurate open-loop position control of the linear motor will be easy to perform, so as to have a good control for the location of the platform in the parallel manipulator. Besides, the constant velocity control of the linear motor can also be achieved if the triangular wave signals are used to be the actuation signals for the thermal actuators. The saw-toothed linear motor has many benefits compared to the push-clamp stepmotor, such as accurate open-loop position control, continuously smooth motion, infinitesimal resolution, and long duration life. A control system built by LabVIEW program has been used to successfully drive the saw-toothed linear motor.

Electrothermal V-beam actuators using multiple arrayed beams have been shown to provide large force up to several mN without loss of displacement. Using a new modeling approach based on the pseudo-rigid-body model, the predicted forces and displacements for electrothermal V-beam actuators are shown to have good agreement with the experimental results. For saving input power and simultaneously having good performance, a thinner, thicker, shorter V-beam and a smaller offset angle for the thermal actuator are desirable design strategies.

Based on the pseudo-rigid-body model, the inverse kinematics and dynamics of the spatial mechanisms have been derived to do the whole micromanipulator design. The characterization of the designed mechanism workspace has also been discussed in this research.

Future work

Due to the adhesion problem, the complete spatial parallel micromechanism was not successfully obtained after release. Since the copper seed layer needs to be deposited between each layer structure, it affects the adhesive strength between different layer nickel structures due to the dissimilar materials. Hence, in the future UV-LIGA fabrication process, a small hole should be opened on the seed layer above the nickel structure, which needs to connect with the other nickel structure, before electroplating. This improved fabrication process will greatly enhance the adhesion, so as to obtain the good device.

Since the pseudo-rigid-body model is used to derive the inverse kinematics of the parallel compliant mechanism, the predicted results are still not accurate enough to fit the real deformation condition. During modeling the compliant mechanism, the fixed characteristic radius factor γ is used to simplify the pseudo-rigid-body model due to its small deviation. However, this value should be changed with the different loading directions. In the future work, this varying factor can be considered into the pseudo-rigid-body model to improve the model accuracy. Furthermore, thin plates are used to be pseudo-revolute compliant joints in the micromechanism. However, the deformation in other orientations may not be negligible due to not enough stiffness. If those compliant joints cannot rotate in only one orientation as the assumption, then this will greatly affect the current model accuracy. To solve this problem in the future, one method is to design the new shape of plate or beam which is more closer to the one-way rotational joint, and the other is to consider other rotational effects into the pseudo-rigid-body model. However, the latter method will influence the degree-of-freedom of the mechanism and

increase the complexity of the mechanism.

In addition, the workspace for this spatial parallel manipulator is another design issue. The dimensions of the compliant joints and the configuration of the parallel manipulator will decide the shape and the volume of this workspace. The workspace optimization of the manipulator will be an advanced research in the future.

The LabVIEW program will be further developed to fit the whole parallel manipulator system. In the program, the calculation of the inverse kinematics will add to the current developed program on the linear motor control. The final control panel will require users to input the desired platform position, and then three linear motors around the platform will automatically move their required locations to let the platform reach its desired position. On the other hand, the LabVIEW program can be modified to provide a full trajectory control over the mechanism workspace. In this program, the user can manually move the working platform to the desired position step by step through the control panel. In other words, the control panel will have six buttons (forward, backward, left, right, up, and down) to actuate six independent platform movements. Any position within the workspace can be reached by combining above six motions. In the absence of sensor measurement, a microscope will be set up on the top of the device to view the planar location of the platform. Therefore, through the observation from microscope, the current platform position can be recognized and modified by a step movement through the control panel if necessary.

Appendix A

Microchannel Fabrication

Microchannels are used in the biological industry for various applications. This appendix will discuss how to create microchannels using the UV-LIGA fabrication process mentioned in Chapter two. In the first step, UV-LIGA fabrication process makes nickel structure on the copper plate as a microchannel mold. Next, the mold repeatedly presses many plastic boards to form channels through the hot embossing process. Figure A.1 demonstrates the whole manufacturing process. The embossing mold and its complementary channels on the plastic board are displayed in Figure A.2.

The silicon bulk manufacturing process is another popular fabrication method for making an embossing mold. The advantages of this process include simple creation and low cost. However, the drawbacks include non-vertical sidewalls in the formed microchannels due to the characteristic of anisotropic silicon etching in KOH solution and the fragile silicon mold subject to break during the hot embossing process. In order to obtain vertical sidewalls, the UV-LIGA process is used to generate the microchannel pattern on the silicon wafer. Figure A.3 exhibits the nickel mold on the silicon wafer and its complementary channels on the plastic board. Unfortunately, due to a fragile silicon wafer and bad adhesion between the wafer and nickel structures, the mold fabricated from UV-LIGA process with the silicon substrate cannot sustain multiple presses during the hot embossing. Therefore, as described above, a 0.125”-thick copper plate replaces the silicon wafer as an electroplating base because the copper plate, providing excellent

adhesion between copper and nickel and possessing strong stiffness, prevents bending and breaking during the hot embossing. Furthermore, such a high-stiff mold can increase the pressing speed so as to shorten the fabrication time without any damage on the mold. Thus the fabrication process is profitable in mass production.

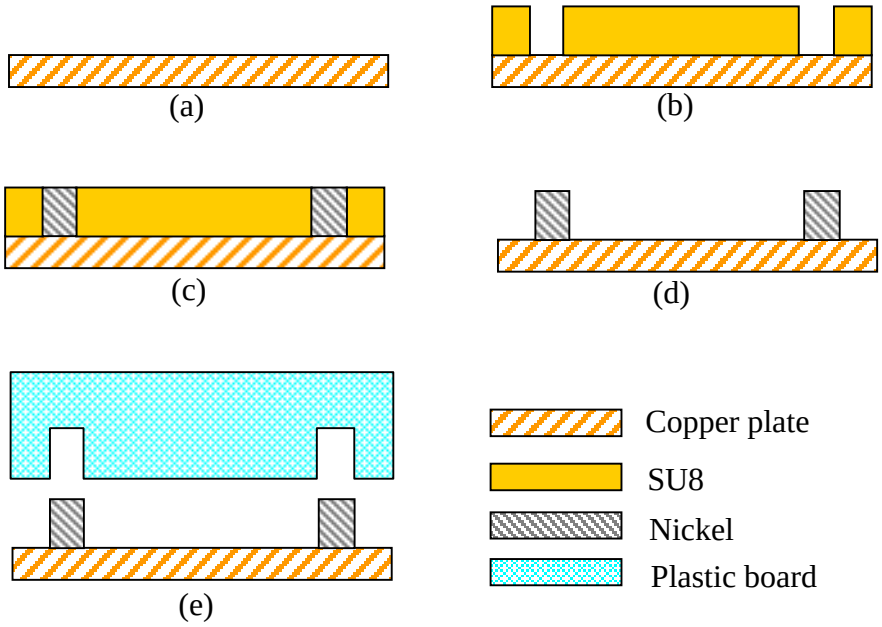

Figure A.1: Whole manufacturing process of microchannels : (a) Prepare a Cu plate (b) Spin SU8 and pattern (c) Electroplate Ni into the SU8 mold and polish the whole plate (d) Remove SU8 using Dynasolve 185 (e) Press the mold on a plastic board by hot embossing.

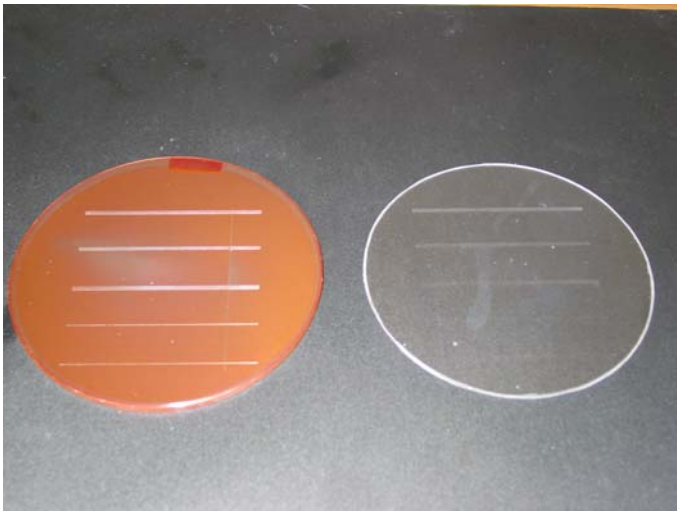

Figure A.2: The left side of the figure is a 4” copper plate with Ni structures, and the right side is microchannels on a plastic board.

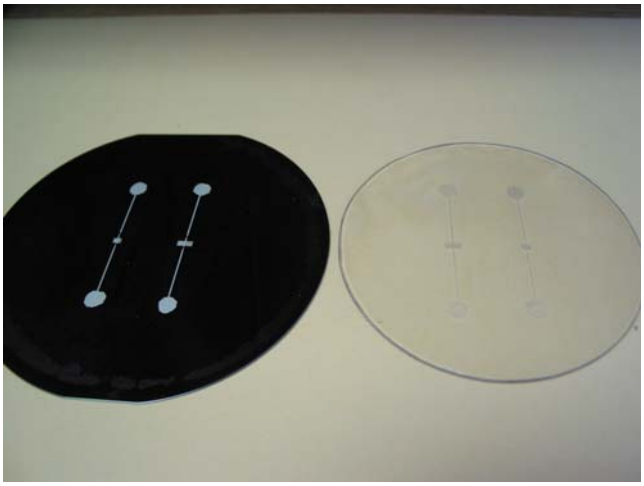

Figure A.3: The left side of the figure is a 4” silicon wafer with Ni structures, and the right side is microchannels on a plastic board.

Appendix B

Evaluation of Partial Derivatives of Constraint Functions for Lagrange-based Dynamics

The generalized coordinates

$$(q_1, q_2, q_3, q_4, q_5, q_6, q_7, q_8, q_9) = (\theta_1^1, \theta_1^2, \theta_1^3, \theta_2^1, \theta_2^2, \theta_2^3, P_1, P_2, P_3)$$

For i = 1, and j = 1,2,…. ,9:

$$CE_1 = \left[-b - \left(c + e + d\cos\theta_2^1\right)\cos\theta_1^1 - f + P_1\right]\cos\phi_1 + d\sin\theta_2^1\sin\phi_1 - \left[-b - \left(c + e + d\cos\theta_2^2\right)\cos\theta_1^2 - f + P_2\right]\cos\phi_2 - d\sin\theta_2^2\sin\phi_2$$

$$A_{11} = \frac{\partial CE_1}{\partial \theta_1^1} = \left(c + e + d\cos\theta_2^1\right)\sin\theta_1^1\cos\phi_1$$

$$A_{12} = \frac{\partial CE_1}{\partial \theta_1^2} = -\left(c + e + d\cos\theta_2^2\right)\sin\theta_1^2\cos\phi_2$$

$$A_{13} = \frac{\partial CE_1}{\partial \theta_1^3} = 0$$

$$A_{14} = \frac{\partial CE_1}{\partial \theta_2^1} = d\sin\theta_2^1\cos\theta_1^1\cos\phi_1 + d\cos\theta_2^1\sin\phi_1$$

$$A_{15} = \frac{\partial CE_1}{\partial \theta_2^2} = -d\sin\theta_2^2\cos\theta_1^2\cos\phi_2 - d\cos\theta_2^2\sin\phi_2$$

$$A_{16} = \frac{\partial CE_1}{\partial \theta_2^3} = 0$$

$$A_{17} = \frac{\partial CE_1}{\partial P_1} = \cos\phi_1$$

$$A_{18} = \frac{\partial CE_1}{\partial P_2} = -\cos\phi_2$$

$$A_{19} = \frac{\partial CE_1}{\partial P_3} = 0$$

For i = 2, and j = 1,2,…. ,9.

$$CE_2 = \left[-b-\left(c+e+d\cos\theta_2^2\right)\cos\theta_1^2 - f + P_2\right]\cos\phi_2 + d\sin\theta_2^2\sin\phi_2$$
$$-\left[-b-\left(c+e+d\cos\theta_2^3\right)\cos\theta_1^3 - f + P_3\right]\cos\phi_3 - d\sin\theta_2^3\sin\phi_3$$

$$A_{21} = \frac{\partial CE_2}{\partial\theta_1^1} = 0$$

$$A_{22} = \frac{\partial CE_2}{\partial\theta_1^2} = \left(c+e+d\cos\theta_2^2\right)\sin\theta_1^2\cos\phi_2$$

$$A_{23} = \frac{\partial CE_2}{\partial\theta_1^3} = -\left(c+e+d\cos\theta_2^3\right)\sin\theta_1^3\cos\phi_3$$

$$A_{24} = \frac{\partial CE_2}{\partial\theta_2^1} = 0$$

$$A_{25} = \frac{\partial CE_2}{\partial\theta_2^2} = d\sin\theta_2^2\cos\theta_1^2\cos\phi_2 + d\cos\theta_2^2\sin\phi_2$$

$$A_{26} = \frac{\partial CE_2}{\partial\theta_2^3} = -d\sin\theta_2^3\cos\theta_1^3\cos\phi_3 - d\cos\theta_2^3\sin\phi_3$$

$$A_{27} = \frac{\partial CE_2}{\partial P_1} = 0$$

$$A_{28} = \frac{\partial CE_2}{\partial P_2} = \cos\phi_2$$

$$A_{29} = \frac{\partial CE_2}{\partial P_3} = -\cos\phi_3$$

For i = 3, and j = 1,2,…. ,9:

$$CE_3 = \left[-b-\left(c+e+d\cos\theta_2^1\right)\cos\theta_1^1 - f + P_1\right]\sin\phi_1 - d\sin\theta_2^1\cos\phi_1$$
$$-\left[-b-\left(c+e+d\cos\theta_2^2\right)\cos\theta_1^2 - f + P_2\right]\sin\phi_2 + d\sin\theta_2^2\cos\phi_2$$

$$A_{31} = \frac{\partial CE_3}{\partial\theta_1^1} = \left(c+e+d\cos\theta_2^1\right)\sin\theta_1^1\sin\phi_1$$

$$A_{32} = \frac{\partial CE_3}{\partial\theta_1^2} = -\left(c+e+d\cos\theta_2^2\right)\sin\theta_1^2\sin\phi_2$$

$$A_{33} = \frac{\partial CE_3}{\partial\theta_1^3} = 0$$

$$A_{34} = \frac{\partial CE_3}{\partial\theta_2^1} = d\sin\theta_2^1\cos\theta_1^1\sin\phi_1 - d\cos\theta_2^1\cos\phi_1$$

$$A_{35} = \frac{\partial CE_3}{\partial\theta_2^2} = -d\sin\theta_2^2\cos\theta_1^2\sin\phi_2 + d\cos\theta_2^2\cos\phi_2$$

$$A_{36} = \frac{\partial CE_3}{\partial\theta_2^3} = 0$$

$$A_{37} = \frac{\partial CE_3}{\partial P_1} = \sin\phi_1$$

$$A_{38} = \frac{\partial CE_3}{\partial P_2} = -\sin\phi_2$$

$$A_{39} = \frac{\partial CE_3}{\partial P_3} = 0$$

For i = 4, and j = 1,2,…. ,9.

$$CE_4 = \left[-b-\left(c+e+d\cos\theta_2^2\right)\cos\theta_1^2 - f + P_2\right]\sin\phi_2 - d\sin\theta_2^2\cos\phi_2$$
$$-\left[-b-\left(c+e+d\cos\theta_2^3\right)\cos\theta_1^3 - f + P_3\right]\sin\phi_3 + d\sin\theta_2^3\cos\phi_3$$

$$A_{41} = \frac{\partial CE_4}{\partial\theta_1^1} = 0$$

$$A_{42} = \frac{\partial CE_4}{\partial\theta_1^2} = \left(c+e+d\cos\theta_2^2\right)\sin\theta_1^2\sin\phi_2$$

$$A_{43} = \frac{\partial CE_4}{\partial\theta_1^3} = -\left(c+e+d\cos\theta_2^3\right)\sin\theta_1^3\sin\phi_3$$

$$A_{44} = \frac{\partial CE_4}{\partial\theta_2^1} = 0$$

$$A_{45} = \frac{\partial CE_4}{\partial\theta_2^2} = d\sin\theta_2^2\cos\theta_1^2\sin\phi_2 - d\cos\theta_2^2\cos\phi_2$$

$$A_{46} = \frac{\partial CE_4}{\partial\theta_2^3} = -d\sin\theta_2^3\cos\theta_1^3\sin\phi_3 + d\cos\theta_2^3\cos\phi_3$$

$$A_{47} = \frac{\partial CE_4}{\partial P_1} = 0$$

$$A_{48} = \frac{\partial CE_4}{\partial P_2} = \sin\phi_2$$

$$A_{49} = \frac{\partial CE_4}{\partial P_3} = -\sin\phi_3$$

For i = 5, and j = 1,2,…. ,9:

$$CE_5 = \left(c + e + d\cos\theta_2^1\right)\sin\theta_1^1 - \left(c + e + d\cos\theta_2^2\right)\sin\theta_1^2$$

$$A_{51} = \frac{\partial CE_5}{\partial \theta_1^1} = \left(c + e + d\cos\theta_2^1\right)\cos\theta_1^1$$

$$A_{52} = \frac{\partial CE_5}{\partial \theta_1^2} = -\left(c + e + d\cos\theta_2^2\right)\cos\theta_1^2$$

$$A_{53} = \frac{\partial CE_5}{\partial \theta_1^3} = 0$$

$$A_{54} = \frac{\partial CE_5}{\partial \theta_2^1} = -d\sin\theta_2^1\sin\theta_1^1$$

$$A_{55} = \frac{\partial CE_5}{\partial \theta_2^2} = d\sin\theta_2^2\sin\theta_1^2$$

$$A_{56} = \frac{\partial CE_5}{\partial \theta_2^3} = 0$$

$$A_{57} = \frac{\partial CE_5}{\partial P_1} = 0$$

$$A_{58} = \frac{\partial CE_5}{\partial P_2} = 0$$

$$A_{59} = \frac{\partial CE_5}{\partial P_3} = 0$$

For i = 6, and j = 1,2,…. ,9:

$$CE_6 = \left(c + e + d\cos\theta_2^2\right)\sin\theta_1^2 - \left(c + e + d\cos\theta_2^3\right)\sin\theta_1^3$$

$$A_{61} = \frac{\partial CE_6}{\partial \theta_1^1} = 0$$

$$A_{62} = \frac{\partial CE_6}{\partial \theta_1^2} = \left(c + e + d\cos\theta_2^2\right)\cos\theta_1^2$$

$$A_{63} = \frac{\partial CE_6}{\partial \theta_1^3} = -\left(c + e + d\cos\theta_2^3\right)\cos\theta_1^3$$

$$A_{64} = \frac{\partial CE_6}{\partial \theta_2^1} = 0$$

$$A_{65} = \frac{\partial CE_6}{\partial \theta_2^2} = -d\sin\theta_2^2\sin\theta_1^2$$

$$A_{66} = \frac{\partial CE_6}{\partial \theta_2^3} = d\sin\theta_2^3\sin\theta_1^3$$

$$A_{67} = \frac{\partial CE_6}{\partial P_1} = 0$$

$$A_{68} = \frac{\partial CE_6}{\partial P_2} = 0$$

$$A_{69} = \frac{\partial CE_6}{\partial P_3} = 0$$

Appendix C

Evaluation of Partial Derivatives of Lagrangian Function for Lagrange-based Dynamics

$$
\begin{aligned}
LQF_i = m_c\Bigg\{&\Bigg[\dot{P}_i + \frac{d}{2}\dot{\theta}_2^i\cos\theta_1^i\sin\theta_2^i + \left(c + \frac{d}{2}\cos\theta_2^i\right)\dot{\theta}_1^i\sin\theta_1^i - \frac{a}{2}\dot{\theta}_1^i\cos\theta_1^i\cos\theta_2^i \\
&+ \frac{a}{2}\dot{\theta}_2^i\sin\theta_1^i\sin\theta_2^i\Bigg]\cos\phi_i + \frac{a}{2}\dot{\theta}_1^i\cos\theta_1^i\sin\theta_2^i\sin\phi_i + \left(\frac{d}{2} + \frac{a}{2}\sin\theta_1^i\right)\dot{\theta}_2^i\cos\theta_2^i\sin\phi_i\Bigg\} \\
&*\Bigg\{\Bigg[-\frac{d}{2}\dot{\theta}_2^i\sin\theta_1^i\sin\theta_2^i + \left(c + \frac{d}{2}\cos\theta_2^i\right)\dot{\theta}_1^i\cos\theta_1^i + \frac{a}{2}\dot{\theta}_1^i\sin\theta_1^i\cos\theta_2^i + \frac{a}{2}\dot{\theta}_2^i\cos\theta_1^i\sin\theta_2^i\Bigg]\cos\phi_i \\
&- \frac{a}{2}\dot{\theta}_1^i\sin\theta_1^i\sin\theta_2^i\sin\phi_i + \frac{a}{2}\dot{\theta}_2^i\cos\theta_1^i\cos\theta_2^i\sin\phi_i\Bigg\} \\
&+ m_c\Bigg\{\Bigg[\dot{P}_i + \frac{d}{2}\dot{\theta}_2^i\cos\theta_1^i\sin\theta_2^i + \left(c + \frac{d}{2}\cos\theta_2^i\right)\dot{\theta}_1^i\sin\theta_1^i - \frac{a}{2}\dot{\theta}_1^i\cos\theta_1^i\cos\theta_2^i \\
&+ \frac{a}{2}\dot{\theta}_2^i\sin\theta_1^i\sin\theta_2^i\Bigg]\sin\phi_i - \frac{a}{2}\dot{\theta}_1^i\cos\theta_1^i\sin\theta_2^i\cos\phi_i - \left(\frac{d}{2} + \frac{a}{2}\sin\theta_1^i\right)\dot{\theta}_2^i\cos\theta_2^i\cos\phi_i\Bigg\} \\
&*\Bigg\{\Bigg[-\frac{d}{2}\dot{\theta}_2^i\sin\theta_1^i\sin\theta_2^i + \left(c + \frac{d}{2}\cos\theta_2^i\right)\dot{\theta}_1^i\cos\theta_1^i + \frac{a}{2}\dot{\theta}_1^i\sin\theta_1^i\cos\theta_2^i + \frac{a}{2}\dot{\theta}_2^i\cos\theta_1^i\sin\theta_2^i\Bigg]\sin\phi_i \\
&+ \frac{a}{2}\dot{\theta}_1^i\sin\theta_1^i\sin\theta_2^i\cos\phi_i - \frac{a}{2}\dot{\theta}_2^i\cos\theta_1^i\cos\theta_2^i\cos\phi_i\Bigg\} \\
&+ m_c\left[-\frac{d}{2}\dot{\theta}_2^i\sin\theta_1^i\sin\theta_2^i + \left(c + \frac{d}{2}\cos\theta_2^i\right)\dot{\theta}_1^i\cos\theta_1^i + \frac{a}{2}\dot{\theta}_1^i\sin\theta_1^i\right]*\left[-\frac{d}{2}\dot{\theta}_2^i\cos\theta_1^i\sin\theta_2^i\right. \\
&\left.-\left(c + \frac{d}{2}\cos\theta_2^i\right)\dot{\theta}_1^i\sin\theta_1^i + \frac{a}{2}\dot{\theta}_1^i\cos\theta_1^i\right] - m_c g\left[\left(c + \frac{d}{2}\cos\theta_2^i\right)\cos\theta_1^i + \frac{a}{2}\sin\theta_1^i\right] - \frac{2\gamma K_\Theta EI}{L_1}\theta_1^i
\end{aligned}
$$

$$
\begin{aligned}
\frac{\partial\hat{L}}{\partial q_1} = \frac{\partial\hat{L}}{\partial\theta_1^1} &= LQF_1 + m_p\left[d\dot{P}_1\dot{\theta}_1^1\cos\theta_1^1\cos\theta_2^1 + (c+e)\dot{P}_1\dot{\theta}_1^1\cos\theta_1^1 - d\dot{P}_1\dot{\theta}_2^1\sin\theta_1^1\sin\theta_2^1\right] \\
&\quad - m_p g\left(c + e + d\cos\theta_2^1\right)\cos\theta_1^1
\end{aligned}
$$

$$
\frac{\partial\hat{L}}{\partial q_2} = \frac{\partial\hat{L}}{\partial\theta_1^2} = LQF_2
$$

$$
\frac{\partial\hat{L}}{\partial q_3} = \frac{\partial\hat{L}}{\partial\theta_1^3} = LQF_3
$$

$$
\begin{aligned}
LQS_i = m_c \Bigg\{ \Bigg[& \dot{P}_i + \frac{d}{2}\dot{\theta}_2^i \cos\theta_1^i \sin\theta_2^i + \left(c + \frac{d}{2}\cos\theta_2^i \right)\dot{\theta}_1^i \sin\theta_1^i - \frac{a}{2}\dot{\theta}_1^i \cos\theta_1^i \cos\theta_2^i \\
& + \frac{a}{2}\dot{\theta}_2^i \sin\theta_1^i \sin\theta_2^i \Bigg] \cos\phi_i + \frac{a}{2}\dot{\theta}_1^i \cos\theta_1^i \sin\theta_2^i \sin\phi_i + \left(\frac{d}{2} + \frac{a}{2}\sin\theta_1^i \right)\dot{\theta}_2^i \cos\theta_2^i \sin\phi_i \Bigg\} \\
& * \Bigg\{ \Bigg[\frac{d}{2}\dot{\theta}_2^i \cos\theta_1^i \cos\theta_2^i - \frac{d}{2}\dot{\theta}_1^i \sin\theta_1^i \sin\theta_2^i + \frac{a}{2}\dot{\theta}_1^i \cos\theta_1^i \sin\theta_2^i + \frac{a}{2}\dot{\theta}_2^i \sin\theta_1^i \cos\theta_2^i \Bigg] \cos\phi_i \\
& + \frac{a}{2}\dot{\theta}_1^i \cos\theta_1^i \cos\theta_2^i \sin\phi_i - \left(\frac{d}{2} + \frac{a}{2}\sin\theta_1^i \right)\dot{\theta}_2^i \sin\theta_2^i \sin\phi_i \Bigg\} \\
& + m_c \Bigg\{ \Bigg[\dot{P}_i + \frac{d}{2}\dot{\theta}_2^i \cos\theta_1^i \sin\theta_2^i + \left(c + \frac{d}{2}\cos\theta_2^i \right)\dot{\theta}_1^i \sin\theta_1^i - \frac{a}{2}\dot{\theta}_1^i \cos\theta_1^i \cos\theta_2^i \\
& + \frac{a}{2}\dot{\theta}_2^i \sin\theta_1^i \sin\theta_2^i \Bigg] \sin\phi_i - \frac{a}{2}\dot{\theta}_1^i \cos\theta_1^i \sin\theta_2^i \cos\phi_i - \left(\frac{d}{2} + \frac{a}{2}\sin\theta_1^i \right)\dot{\theta}_2^i \cos\theta_2^i \cos\phi_i \Bigg\} \\
& * \Bigg\{ \Bigg[\frac{d}{2}\dot{\theta}_2^i \cos\theta_1^i \cos\theta_2^i - \frac{d}{2}\dot{\theta}_1^i \sin\theta_1^i \sin\theta_2^i + \frac{a}{2}\dot{\theta}_1^i \cos\theta_1^i \sin\theta_2^i + \frac{a}{2}\dot{\theta}_2^i \sin\theta_1^i \cos\theta_2^i \Bigg] \sin\phi_i \\
& - \frac{a}{2}\dot{\theta}_1^i \cos\theta_1^i \cos\theta_2^i \cos\phi_i + \left(\frac{d}{2} + \frac{a}{2}\sin\theta_1^i \right)\dot{\theta}_2^i \sin\theta_2^i \cos\phi_i \Bigg\} \\
& + m_c \Bigg[-\frac{d}{2}\dot{\theta}_2^i \sin\theta_1^i \sin\theta_2^i + \left(c + \frac{d}{2}\cos\theta_2^i \right)\dot{\theta}_1^i \cos\theta_1^i + \frac{a}{2}\dot{\theta}_1^i \sin\theta_1^i \Bigg] * \Bigg[-\frac{d}{2}\dot{\theta}_2^i \sin\theta_1^i \cos\theta_2^i \\
& - \frac{d}{2}\dot{\theta}_1^i \cos\theta_1^i \sin\theta_2^i \Bigg] + \frac{1}{2} m_c g d \sin\theta_1^i \sin\theta_2^i - \frac{8\gamma K_\Theta EI}{L_2}\theta_2^i
\end{aligned}
$$

$$
\begin{aligned}
\frac{\partial \hat{L}}{\partial q_4} = \frac{\partial \hat{L}}{\partial \theta_2^1} = LQS_1 + m_p \Big[& - d^2 \dot{\theta}_1^{1^2} \cos\theta_2^1 \sin\theta_2^1 + d\dot{P}_1 \dot{\theta}_2^1 \cos\theta_1^1 \cos\theta_2^1 - (c+e) d \dot{\theta}_1^{1^2} \sin\theta_2^1 \\
& - d\dot{P}_1 \dot{\theta}_1^1 \sin\theta_1^1 \sin\theta_2^1 \Big] + m_p g d \sin\theta_1^1 \sin\theta_2^1
\end{aligned}
$$

$$
\frac{\partial \hat{L}}{\partial q_5} = \frac{\partial \hat{L}}{\partial \theta_2^2} = LQS_2
$$

$$
\frac{\partial \hat{L}}{\partial q_6} = \frac{\partial \hat{L}}{\partial \theta_2^3} = LQS_3
$$

$$
\frac{\partial \hat{L}}{\partial q_7} = \frac{\partial \hat{L}}{\partial P_1} = 0
$$

$$
\frac{\partial \hat{L}}{\partial q_8} = \frac{\partial \hat{L}}{\partial P_2} = 0
$$

$$
\frac{\partial \hat{L}}{\partial q_9} = \frac{\partial \hat{L}}{\partial P_3} = 0
$$

$$DLQF_i = \frac{1}{4} m_c \Big[\Big(a^2 + 4c^2 + d^2 \cos^2 \theta_2^i + 4cd \cos\theta_2^i \Big) \ddot{\theta}_1^i + 4ac\ddot{\theta}_1^i \sin\theta_1^i \cos\theta_1^i \Big(1 - \cos\theta_2^i\Big)$$
$$+ 2ad\ddot{\theta}_1^i \sin\theta_1^i \cos\theta_1^i \cos\theta_2^i \Big(1 - \cos\theta_2^i\Big) + \Big(4c + 2d\cos\theta_2^i\Big)\ddot{P}_i \sin\theta_1^i - 2a\ddot{P}_i \cos\theta_1^i \cos\theta_2^i$$
$$+ (2ac - ad)\ddot{\theta}_2^i \sin^2\theta_1^i \sin\theta_2^i + ad\ddot{\theta}_2^i \Big(\cos\theta_1^i - \cos 2\theta_1^i\Big)\sin\theta_2^i \cos\theta_2^i$$
$$+ 4ac\dot{\theta}_1^{i\,2} \cos 2\theta_1^i \Big(1 - \cos\theta_2^i\Big) + 2ad\dot{\theta}_1^{i\,2} \cos 2\theta_1^i \cos\theta_2^i \Big(1 - \cos\theta_2^i\Big) - ad\dot{\theta}_2^{i\,2} \cos 2\theta_1^i \cos 2\theta_2^i$$
$$+ (2ac - ad)\dot{\theta}_2^{i\,2} \sin^2\theta_1^i \cos\theta_2^i + ad\dot{\theta}_2^{i\,2} \cos\theta_1^i \cos 2\theta_2^i + 4c\dot{P}_i\dot{\theta}_1^i \cos\theta_1^i + 2a\dot{P}_i\dot{\theta}_1^i \sin\theta_1^i \cos\theta_2^i$$
$$+ 2d\dot{P}_i\dot{\theta}_1^i \cos\theta_1^i \cos\theta_2^i + 2a\dot{P}_i\dot{\theta}_2^i \cos\theta_1^i \sin\theta_2^i - 2d\dot{P}_i\dot{\theta}_2^i \sin\theta_1^i \sin\theta_2^i - 4cd\dot{\theta}_1^i\dot{\theta}_2^i \sin\theta_2^i$$
$$+ 8ac\dot{\theta}_1^i\dot{\theta}_2^i \sin\theta_1^i \cos\theta_1^i \sin\theta_2^i - 2d^2\dot{\theta}_1^i\dot{\theta}_2^i \sin\theta_2^i \cos\theta_2^i$$
$$- ad\dot{\theta}_1^i\dot{\theta}_2^i \sin\theta_1^i \sin\theta_2^i \Big(4\cos\theta_1^i - 8\cos\theta_1^i \cos\theta_2^i + \cos\theta_2^i\Big)\Big]$$

$$\frac{d}{dt}\left(\frac{\partial \hat{L}}{\partial \dot{q}_1}\right) = \frac{d}{dt}\left(\frac{\partial \hat{L}}{\partial \dot{\theta}_1^1}\right) = DLQF_1 + m_p \Big[(c+e)^2 \ddot{\theta}_1^1 + \Big(2cd + 2ed + d^2\cos\theta_2^1\Big)\ddot{\theta}_1^1 \cos\theta_2^1$$
$$+ \Big(c + e + d\cos\theta_2^1\Big)\Big(\ddot{P}_1 \sin\theta_1^1 + \dot{P}_1\dot{\theta}_1^1 \cos\theta_1^1\Big) - d\dot{P}_1\dot{\theta}_2^1 \sin\theta_1^1 \sin\theta_2^1$$
$$- 2\Big(cd + ed + d^2\cos\theta_2^1\Big)\dot{\theta}_1^1\dot{\theta}_2^1 \sin\theta_2^1\Big]$$

$$\frac{d}{dt}\left(\frac{\partial \hat{L}}{\partial \dot{q}_2}\right) = \frac{d}{dt}\left(\frac{\partial \hat{L}}{\partial \dot{\theta}_1^2}\right) = DLQF_2$$

$$\frac{d}{dt}\left(\frac{\partial \hat{L}}{\partial \dot{q}_3}\right) = \frac{d}{dt}\left(\frac{\partial \hat{L}}{\partial \dot{\theta}_1^3}\right) = DLQF_3$$

$$DLQS_i = \frac{1}{4} m_c \Big[2\left(a\sin\theta_1^i + d\cos\theta_1^i\right)\ddot{P}_i \sin\theta_2^i - ad\ddot{\theta}_1^i \sin^2\theta_1^i \sin\theta_2^i + ad\ddot{\theta}_1^i \left(\cos\theta_1^i - \cos 2\theta_1^i\right)\sin\theta_2^i \cos\theta_2^i$$
$$+ 2ac\ddot{\theta}_1^i \sin^2\theta_1^i \sin\theta_2^i + d^2\ddot{\theta}_2^i + a^2\ddot{\theta}_2^i \sin^2\theta_1^i + 2ad\ddot{\theta}_2^i \sin\theta_1^i \cos^2\theta_2^i$$
$$+ 2ad\ddot{\theta}_2^i \sin\theta_1^i \cos\theta_1^i \sin^2\theta_2^i + \left(4ac - 2ad\right)\dot{\theta}_1^{i\,2} \sin\theta_1^i \cos\theta_1^i \sin\theta_2^i$$
$$- ad\left(\dot{\theta}_1^{i\,2} + 4\dot{\theta}_2^{i\,2}\right)\sin\theta_1^i \sin\theta_2^i \cos\theta_2^i + 4ad\left(\dot{\theta}_1^{i\,2} + \dot{\theta}_2^{i\,2}\right)\sin\theta_1^i \cos\theta_1^i \sin\theta_2^i \cos\theta_2^i$$
$$+ 4ad\dot{\theta}_1^i\dot{\theta}_2^i \cos^2\theta_2^i \left(\cos\theta_1^i - \cos 2\theta_1^i\right) - ad\dot{\theta}_1^i\dot{\theta}_2^i \sin^2\theta_1^i \cos\theta_2^i + 3ad\dot{\theta}_1^i\dot{\theta}_2^i \cos 2\theta_1^i$$
$$- ad\dot{\theta}_1^i\dot{\theta}_2^i \cos\theta_1^i + 2a^2\dot{\theta}_1^i\dot{\theta}_2^i \sin\theta_1^i \cos\theta_1^i + 2ac\dot{\theta}_1^i\dot{\theta}_2^i \sin^2\theta_1^i \cos\theta_2^i$$
$$+ 2\left(a\cos\theta_1^i - d\sin\theta_1^i\right)\dot{P}_i\dot{\theta}_1^i \sin\theta_2^i + 2\left(a\sin\theta_1^i + d\cos\theta_1^i\right)\dot{P}_i\dot{\theta}_2^i \cos\theta_2^i \Big]$$

$$\frac{d}{dt}\left(\frac{\partial\hat{L}}{\partial\dot{q}_4}\right) = \frac{d}{dt}\left(\frac{\partial\hat{L}}{\partial\dot{\theta}_2^1}\right) = DLQS_1 + m_p\left[d^2\ddot{\theta}_2^1 + d\ddot{P}_1 \cos\theta_1^1 \sin\theta_2^1 - d\dot{P}_1\dot{\theta}_1^1 \sin\theta_1^1 \sin\theta_2^1 + d\dot{P}_1\dot{\theta}_2^1 \cos\theta_1^1 \cos\theta_2^1\right]$$

$$\frac{d}{dt}\left(\frac{\partial\hat{L}}{\partial\dot{q}_5}\right) = \frac{d}{dt}\left(\frac{\partial\hat{L}}{\partial\dot{\theta}_2^2}\right) = DLQS_2$$

$$\frac{d}{dt}\left(\frac{\partial\hat{L}}{\partial\dot{q}_6}\right) = \frac{d}{dt}\left(\frac{\partial\hat{L}}{\partial\dot{\theta}_2^3}\right) = DLQS_3$$

$$DLQT_i = \left(m_c + m_s\right)\ddot{P}_i + m_c\Big[\frac{a}{2}\left(\dot{\theta}_1^{i\,2} + \dot{\theta}_2^{i\,2}\right)\sin\theta_1^i \cos\theta_2^i + \frac{d}{2}\left(\dot{\theta}_1^{i\,2} + \dot{\theta}_2^{i\,2}\right)\cos\theta_1^i \cos\theta_2^i + c\dot{\theta}_1^{i\,2} \cos\theta_1^i$$
$$+ \frac{d}{2}\ddot{\theta}_1^i \sin\theta_1^i \cos\theta_2^i + \frac{d}{2}\ddot{\theta}_2^i \cos\theta_1^i \sin\theta_2^i - \frac{a}{2}\ddot{\theta}_1^i \cos\theta_1^i \cos\theta_2^i + \frac{a}{2}\ddot{\theta}_2^i \sin\theta_1^i \sin\theta_2^i + c\ddot{\theta}_1^i \sin\theta_1^i$$
$$+ a\dot{\theta}_1^i\dot{\theta}_2^i \cos\theta_1^i \sin\theta_2^i - d\dot{\theta}_1^i\dot{\theta}_2^i \sin\theta_1^i \sin\theta_2^i\Big]$$

$$\frac{d}{dt}\left(\frac{\partial\hat{L}}{\partial\dot{q}_7}\right) = \frac{d}{dt}\left(\frac{\partial\hat{L}}{\partial\dot{P}_1}\right) = DLQT_1 + m_p\Big[\ddot{P}_1 + \left(c+e\right)\dot{\theta}_1^{1\,2} \cos\theta_1^1 + \left(c+e\right)\ddot{\theta}_1^1 \sin\theta_1^1 + d\left(\dot{\theta}_1^{1\,2} + \dot{\theta}_2^{1\,2}\right)\cos\theta_1^1 \cos\theta_2^1$$
$$+ d\ddot{\theta}_1^1 \sin\theta_1^1 \cos\theta_2^1 + d\ddot{\theta}_2^1 \cos\theta_1^1 \sin\theta_2^1 - 2d\dot{\theta}_1^1\dot{\theta}_2^1 \sin\theta_1^1 \sin\theta_2^1\Big]$$

$$\frac{d}{dt}\left(\frac{\partial\hat{L}}{\partial\dot{q}_8}\right) = \frac{d}{dt}\left(\frac{\partial\hat{L}}{\partial\dot{P}_2}\right) = DLQT_2$$

$$\frac{d}{dt}\left(\frac{\partial\hat{L}}{\partial\dot{q}_9}\right) = \frac{d}{dt}\left(\frac{\partial\hat{L}}{\partial\dot{P}_3}\right) = DLQT_3$$

Appendix D

LabVIEW Diagram

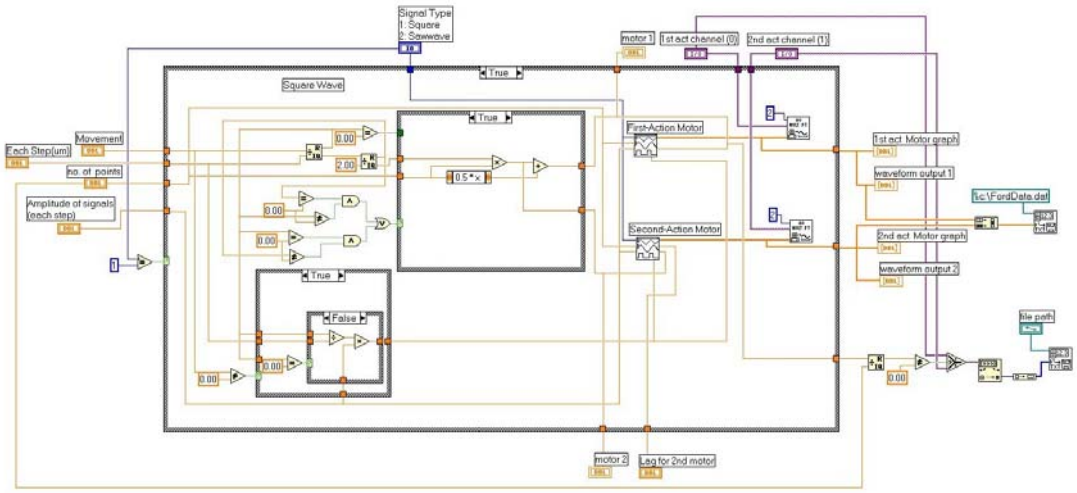

Forward system block diagram

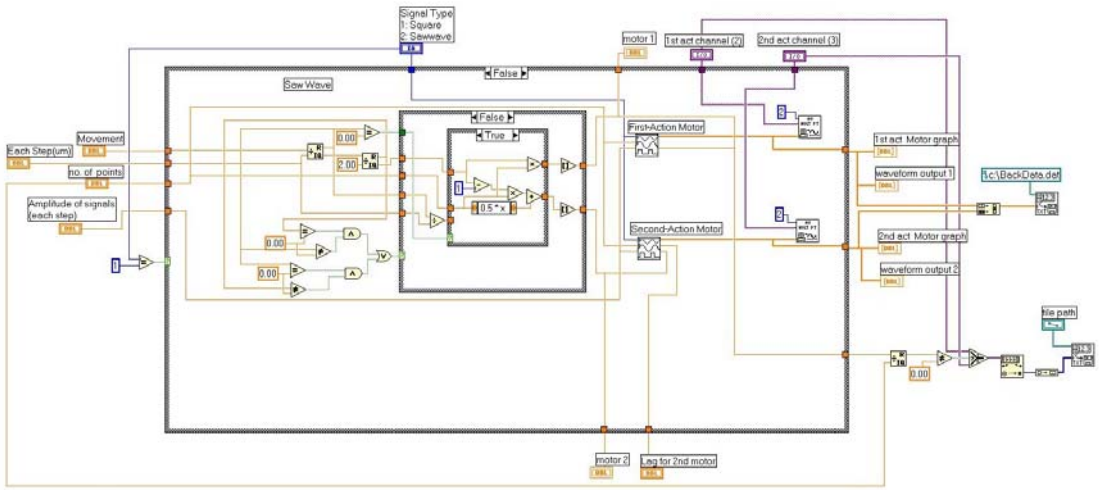

Backward system block diagram

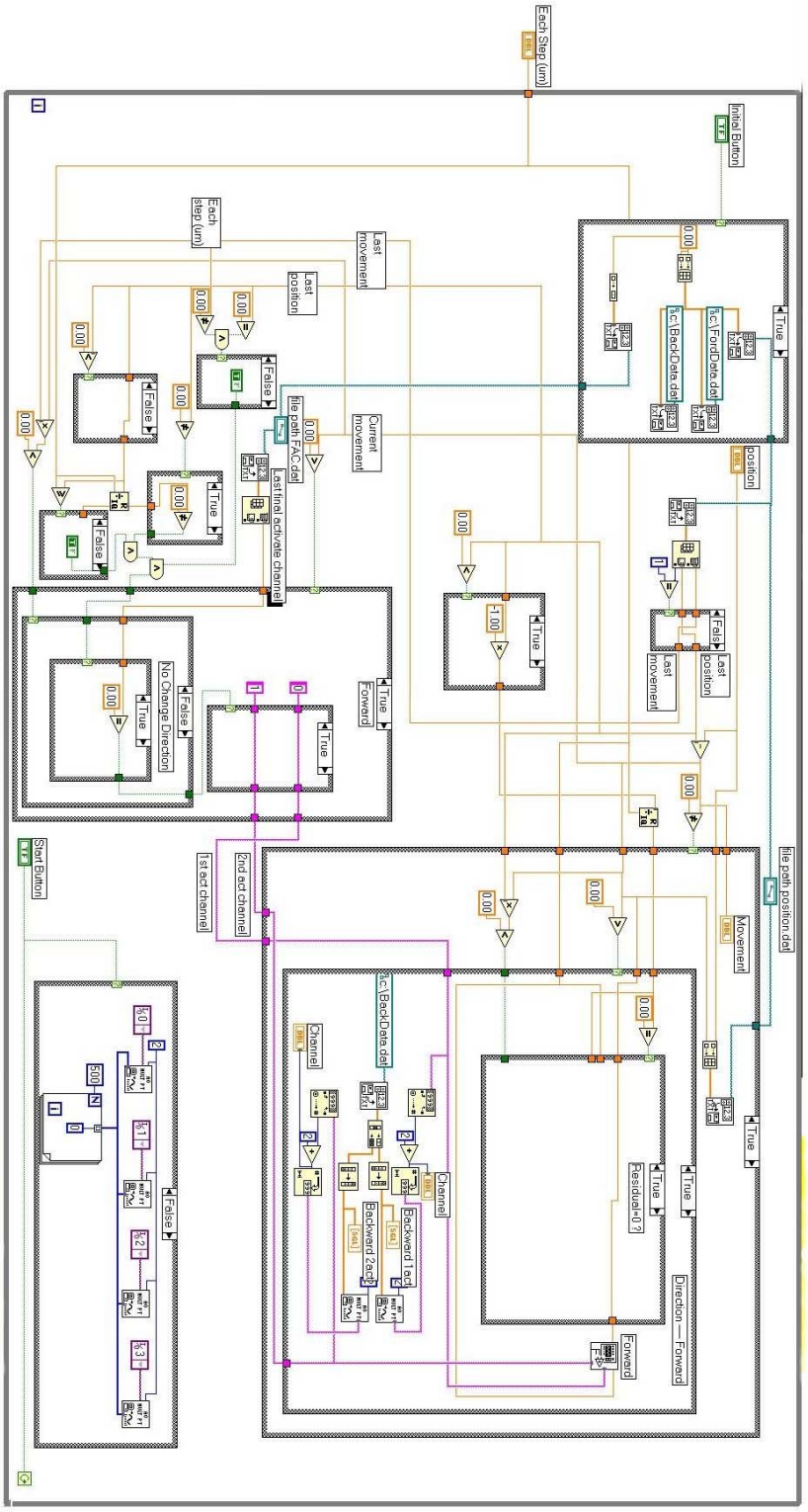

Main control block diagram

References

[1] Lung-Wen Tsai, Robot Analysis ---- the mechanics of serial and parallel manipulators, John Wiley & Sons, Inc. 1999.

[2] Richard E. Stamper, A Three Degree of Freedom Parallel Manipulator with Only Translational Degrees of Freedom, PhD's dissertation, University of Maryland, College Park, MD. 1997.

[3] John M. Maloney, Fabrication and Thermal Actuation of 3-D Micro Electro Mechanical Systems, Master's thesis, University of Maryland, College Park, MD. 2001.

[4] David S. Schreiber, Surface Micromachined Electrothermal V-beam Microactuators and Microstepper Motors, Master's thesis, University of Maryland, College Park, MD. 2001.

[5] David S. Schreiber, Wei-jen Cheng, John M. Maloney, and Don L. DeVoe. "Surface Micromachined Electrothermal V-beam micromotors". Proc of 2001 ASME International Mechanical Engineering Congress and Exposition, 2001, pp.141-147.

[6] Richard Yeh, Ezekiel J.J. Kruglick, and Kristofer S.J. Pister, "Microelectromechanical components for articulated microrobots", Transducers '95, IEEE International Conference on Solid-State Sensors and Actuators, Sweden, 1995, pp.346-349.

[7] Xinxin Li, Minhang Bao, and Shaoqun Shen, “Maskless anisotropic etching ---- A novel micromachining technology for multilevel microstructures”, Transducers ’97. IEEE International Conference on Solid-State Sensors and Actuators, 1997, pp.699-702.

[8] M. Steven Rodgers and Jeffry J. Sniegowski, “5-level polysilicon surface micromachine technology: application to complex mechanical systems”, Solid-State Sensor and Actuator Workshop, 1998, pp.144-149.

[9] Jun-Bo Yoon, Chul-Hi Han, Euisik Yoon and Choong-Ki Kim, “Monolithic integration of 3-D electroplated microstructures with unlimited number of levels using planarization with a sacrificial metallic mold (PSMM)”, 12th IEEE International Conference on Micro Electro Mechanical Systems, 1999, pp.624-629.

[10] Todd R. Christenson and Dave T. Schmale, “A batch wafer scale LIGA assembly and packaging technique via diffusion bonding”, 12th IEEE International Conference on Micro Electro Mechanical Systems, 1999, pp.476-481.

[11] Shaun Sullivan, Xin Zhang, Arturo A. Ayon, and J.G. Brisson, “Demonstration of a microscale heat exchanger for a silicon micro gas turbine engine”, Transducers ’01, IEEE International Conference on Solid-State Sensors and Actuators, Germany, 2001.

[12] Murat Gel and Isao Shimoyama, “High aspect ratio micro actuation mechanism”, 14th IEEE International Conference on Micro Electro Mechanical Systems, 2001, pp.582-585.

[13] L.L. Howell, A. Midha, and T.W. Norton, “Evaluation of equivalent spring stiffness for use in a pseudo-rigid-body model of large-deflection compliant mechanisms”, Journal of Mechanical Design, Trans. ASME, Vol. 118, No. 1, 1996, pp.126-131.

[14] Siu Lai Chan, “Large deflection kinematic formulations for three-dimensional framed structures”, Computer Methods in Applied Mechanics and Engineering, Vol. 95, 1992, pp.17-36.

[15] Zhijia Yang and J.P. Sadler, “Large-displacement finite element analysis of flexible linkages”, Journal of Mechanical Design, Trans. ASME, Vol. 112, 1990, pp.175-182.

[16] Yoshihiko Koseki, Tamio Tanikawa, Noriho Koyachi and Tatsuo Arai, “Kinematic analysis of a translational 3-d.o.f. micro-parallel mechanism using the matrix method”, Advanced Robotics, Vol. 16, No. 3, 2002, pp.251-264.

[17] C.M. Gosselin and D. Zhang, “Stiffness analysis of parallel mechanisms using a lumped model”, International Journal of Robotics and Automation, Vol. 17, No. 1, 2002, pp.17-27.

[18] S.L. Canfield, J.W. Beard, N. Lobontiu, E. O’Malley, M. Samuelson, and J. Paine,” Development of a spatial compliant manipulator”, International Journal of Robotics and Automation, Vol. 17, No. 1, 2002, pp.63-70.

[19] Qing-An Huang and Necille Ka Shek Lee. “Analysis and design of polysilicon thermal flexure actuator “ Journal of Micromechanics and Microengineering, Vol. 9, No. 1, 1999, pp. 64-70.

[20] Liwei Lin, MuChiao. “Electrothermal responses of lineshape microstructures”, Sensors and Actuators A (Physical), Vol. A55, 1996, pp.35-41.

[21] Comtois, J.h., Michalicek, M.A., and Barron, C.C.,”Electrothermal Actuator Fabricated in Four_Level Planarized Surface Micromachined Polycrystalline Silicon”, Sensors and Actuators A (Physical), Vol. A70, 1998, pp.23-31.

[22] Okada, Y., and Y. Tokumaru, “Precise determination of lattice parameter and thermal expansion coefficient of silicon between 300 and 1500 K”, Journal of Applied Physics. Vol. 56, 1984, pp. 314-320.

[23] Jonsmnn, J., Sigmund, O., and Bouwstra, S.,”Compliant Thermal Microactuators.” Sensors and Actuators (Physical), Vol. A76, 1999, pp.463-469.

[24] M. Baltzer, T. Kraus, and E. Obermeier, “A linear stepping actuator in surface micromachining technology for low voltages and large displacements”, Transducers’ 97, IEEE International Conference on Solid-State Sensors and Actuators, 1997, pp. 781-784.

[25] Richard Yeh, Seth Hollar, and Kristofer S.J. Pister, “Single mask, large force, and large displacement electrostatic linear inchworm motors”, Journal of Microelectromechanical Systems, Vol. 11, No. 4, 2002, pp. 330-336.

[26] N.R. Tas, A.H. Sonnenberg, A.F. Sander and M.C. Elwenspoek, “Surface micromachined linear electrostatic stepper motor”, Proc. IEEE Micro Electro Mechanical Systems Workshop 1997, Nagoya, Japan, 1997, pp. 215-220.

[27] Niels Tas, Jeroen Wissink, Louis Sander, Theo Lammerink, Miko Elwenspoek, “Modeling, design and testing of the electrostatic shuffle motor”, Sensors and Actuators A (Physical), Vol. A70, 1998, pp. 171-178.

[28] Minfan Pai and Norman C. Tien, “Current-controlled bi-directional electrothermally actuated vibromtor”, Transducers ’99. IEEE International Conference on Solid-State Sensors and Actuators, 1999.

[29] Larry L. Howell, Compliant Mechanisms, John Wiley & Sons, Inc. 2001.

[30] A. Kenneth Graham, Electroplating Engineering Handbook, Van Nostrand Reinhold Co. 1971.

[31] Jack W. Dini, Electrodeposition: the materials science of coatings and substrates, Noyes Publications, New Jersey 1993.

[32] Chien-Hung Ho, Kan-Ping Chin, Chii-Rong Yang, Hsien-Ming Wu, and Soon-Lin Chen. “ Ultrathick SU-8 mold formation and removal, and its application to the fabrication of LIGA-like micromotors with embedded roots”. Sensors and Actuators A, Vol. 102, 2002, pp. 130-138.

[33] Koester, D. A., Mehadevan, R., Hardy, B., Markus, K. W., MUMPs Introduction and Design Handbook, rev. 6.0. Research Triangle Park, NC: Cronos Integrated Microsystems, A JDS Uniphase Company, 2001.

[34] Terunobu Akiyama and Katsufusa Shono, “Controlled stepwise motion in polysilicon microstructures”, Journal of Microelectromechanical Systems, Vol. 2, No. 3, 1993, pp. 106-110.

[35] A. Koga, K. Suzumori, H. Sudo, S. Iikura, and M. Kimura, “Electrostatic linear microactuator mechanism for focusing a CCD camera”, Journal of Lightwave Technology, Vol. 17, No. 1, 1999, pp. 43-47.

[36] K. Minami, S. Kawamura, and M. Esashi, “Fabrication of distributed electrostatic micro actuator (DEMA)”, Journal of Microelectromechanical Systems, Vol. 2, No. 3, 1993, pp. 121-127.

[37] E.T. Carlen and C. H. Mastrangelo, “Simple, high actuation power, thermally activated paraffin microactuator”, Transducers’99, IEEE International Conference on Solid-State Sensors and Actuators, 1999.

[38] John H. Comtois and Victor M. Bright, “Applications for surface- micromachined polysilicon thermal actuators and arrays”, Sensor and Actuators A (Physical), Vol. A58, No. 1, 1997, pp. 19-25.

[39] B. Wagner, M. Kreutzer, and W. Benecke, “Permanent magmet micromotors on silicon substrates”, Journal of Microelectromechanical Systems, Vol. 2, No. 1, 1993, pp. 23-28.

[40] N. Takeshima and H. Fujita, “Polyimide bimorph actuators for a ciliary motion system”, Micromechanical Sensors, Actuators and Systems, Proceedings of the ASME Winter Annual Meeting, DSC-Vol. 32, 1991, pp. 203-209.

[41] M.T.A Saif and N. C. MacDonald, “A millinewton microloading device”, Transducers ’95, IEEE International Conference on Solid-State Sensors and Actuators, Vol. 2, 1995, pp. 60-63.

[42] R. Yeh, E. Kruglick, and K.S.J. Pister, “Microelectromechanical components for articulated microrobots”, Transducers ’95, IEEE International Conference on Solid-State Sensors and Actuators, Vol. 2, 1995, pp. 346-349.

[43] Masaya Takasaki, Minoru K. Kurosawa, and Toshiro Higuchi, “Optimum silicon slider design for 50 MHz SAW linear motor”, Transducers ’99, IEEE International Conference on Solid-State Sensors and Actuators, 1999.

[44] Minoru K. Kurosawa, Makoto Chiba and Toshiro Higuchi, “Evaluation of a surface acoustic wave motor with a multi-contact-point slider”, Smart Material Structure, Vol. 7, 1998, pp. 305-311.

[45] Y. Mita, T. Oba, G. Hashiguchi, M. Mita, P. Minotti, and H. Fujita, “An inverted Scratch-Drive-Actuators array for large area actuation of external objects”, Transducers ’99, IEEE International Conference on Solid-State Sensors and Actuators, 1999.

[46] H. Nakazawa, Y. Watanabe, O. Morita, M. Edo, and E. Yonezawa, “The two-dimensional micro conveyer: principles and fabrication process of the actuator”, Transducers ’97, IEEE International Conference on Solid-State Sensors and Actuators, 1997, pp. 33-36.

[47] Toshiki Hirano, Tomotake Furuhata, Kaigham J. Gabriel, and Hiroyuki Fujita, “Design, fabrication, and operation of submicron gap comb-drive microactuators”, Journal of Microelectromechanical Systems. Vol. 1, No. 1, 1992, pp. 52-59.

[48] Toshiki Niino, Saku Egawa, Noboru Nishiguchi, and Toshiro Higuchi, “Development of an electrostatic actuator exceeding 10N propulsive force”, IEEE Micro Electro Mechanical System, Germany, 1992, pp. 122-127.

[49] David A. Horsley, Naiyavudhi Wongkomet, Roberto Horowitz, and Albert P. Pisano, ”Design and feedback control of electrostatic actuators for magnetic disk drives”, IEEE Solid-State Sensor and Actuator Workshop, 1998, pp. 120-123.

[50] Ki Bang Lee and Young-Ho Cho, “Laterally driven electrostatic repulsive-force microactuators using asymmetric field distribution”, Journal of Microelectromechanical Systems. Vol. 10, No. 1, 2001, pp. 128-136.

[51] Rob Legtenberg, Erwin Berenschot, Miko Elwenspoek and Jan Fluitman, ”Electrostatic curved electrode actuators”, IEEE Solid-State Sensor and Actuator Workshop, 1995, pp. 37-42.

[52] Timothy Moulton and G.K. Ananthasuresh, “Micromechanical devices with embedded electro-thermal-compliant actuation”, Sensors and Actuators A, Vol. 90, 2001, pp. 38-48.

[53] Long Que, Jae-Sung Park, and Y. B. Gianchandani, “Bent-beam electro-thermal actuators for high force applications”, IEEE Conference on Micro Electro Mechanical Systems, Orlando, FL, 1999, pp. 31-36.

[54] Long Que, Jae-Sung Park, and Y. B. Gianchandani, ”Bent-beam electrothermal actuators-Part I: Single beam and cascaded devices”, Journal of Microelectromechanical Systems, Vol. 10, No. 2, 2001, pp. 247-254.

[55] Peter Krulevitch, Abraham P. Lee, Philip B. Ramsey, James C. Trevino, Julie Hamilton, and M. Allen Northrup, “ Thin film shape memory alloy microactuators”, Journal of Microelectromechanical Systems, Vol. 5, No. 4, 1996, pp. 270-281.

[56] John A. Wright, Yu-Chong Tai and Shih-Chia Chang, “A large-force, fully-integrated MEMS magnetic actuator”, Transducers ’97, IEEE International Conference on Solid-State Sensors and Actuators, New York, 1997, pp. 793-796.

[57] X.Y. Ye, Y. Huang, Z.Y. Zhou, Q.C. Li and Q.L. Gong, “A magnetic levitation actuator for micro-assembly”, Transducer ’97, IEEE International Conference on Solid-State Sensors and Actuators, 1997, pp. 797-799.

[58] Ras Kaas Vestergaard and Siebe Bouwstra, “Electroplated compliant metal microactuators with small feature sizes using a removeable SU-8 mould”, Microsystem Technologies, Vol. 6, No. 6, 2000, pp. 214-217.

[59] Junghoon Lee and Chang-Jin Kim, “Surface-tension-driven microactuation based on continuous electrowetting”, Journal of Microelectromechanical Systems, Vol. 9, No. 2, 2000, pp. 171-180.

[60] Masaichiro Seika, Yasuo Nagase, Kikuo Hosono, and Noriaki Taketani, “Fundamental studies on the copper and nickel --- Electroplating methods of Stress Analysis”, Bulletin of the JSME, Vol. 25, No. 209, 1982, pp. 1653-1661.

[61] N.V. Mandich and D.W. Baudrand, “Troubleshooting electroplating installations: nickel sulfamate plating systems”, Plating & Surface Finishing, 2002, pp. 68-76.

[62] W.H. The, J.K. Luo, M.R. Graham, A. Pavlov and C.G. Smith, “Near-zero curvature fabrication of miniaturized micromechanical Ni switches using electron beam cross-linked PMMA”, Journal of Micromechanics and Microengineering, Vol. 13, No. 5, 2003, pp. 591-598.

[63] J. Gobet, F. Cardot, J. Bergqvist, and F. Rudolf, “Electrodeposition of 3D microstructures on silicon”, Journal of Micromechanics and Microengineering, Vol. 3, No. 3, 1993, pp. 123-130.

[64] B.B. Knapp, “Notes on nickel plating from sulfamate solutions”, Plating, Vol. 58, 1971, pp. 1187-1193.

[65] J.W. Dini and H.R. Johnson, “The influence of nickel sulfamate operating parameters on the impurity content and properties of electrodeposits”, Thin Solid Films, Vol. 54, 1978, pp. 183-188.

[66] J.R. Weber, “Solution chemistry control for nickel sulfamate electroforming”, Plating and Surface Finishing, Vol. 62, No. 8, 1975, pp. 780-783.

[67] S.A. Watson, “Nickel sulphamate solutions”, NiDi Technical Series, No. 10052, 1990.

[68] R.J. Kendrick, “High speed nickel plating from sulfamate solutions”, Transactions of the Institution of Metal Finishing, Vol. 42, 1964, pp. 235-241.

[69] Fredric Ericson, Staffan Greek, Jan Söderkvist and Jan-Åke Schweitz, “High-sensitivity surface micromachined structures for internal stress and stress gradient evaluation”, Journal of Micromechanical Microengineering, Vol. 7, 1997, pp. 30-36.

[70] Johannes Frans Lodewijk Goosen, Design and fabrication of a surface micromachined positioning device, Delft University Press, 1996.

[71] R.W. Powell, R.P. Tye and M.J. Hickman, “The thermal conductivity of nickel”, International Journal of Heat and Mass Transfer, Vol. 8, 1965, pp. 679-688.

[72] F.H. Schofield, “The thermal and electrical conductivities of some pure metals”, Proceedings of the Royal Society of London, Vol. A107, No. 742, 1925, pp. 206-227.

[73] William H. Safranek, The Properties of Electrodeposited Metals and Alloys, A Handbook, Second Edition, American Electroplaters and Surface Finishers Society, 1986.

[74] M.A. Angadi and L.A. Udachan, “Electrical properties of thin nickel films”, Thin Solid Films, Vol. 79, 1981, pp. 149-153.

[75] Hong Qiu, Gyorgy Safran, Bela Pecz, Peter B. Barna, Akio Kosuge, Hisashi Nakai, Shigemi Yugo and Mituru Hashimoto, “Structural and electrical properties of Ni films grown on Si(100) and SiO_2 by d.c. bias sputtering”, Thin Solid Films, Vol. 229, 1993, pp. 107-112.

[76] Jerry J. Broz, Scott Stalnaker, and Gene Humphrey, “Controlling contact resistance”, EE-Evaluation Engineering, Nelson Publishing Inc., 2004.

(http://www.evaluationengineering.com/archive/articles/0504/0504controlling.asp)

[77] L. Kogut and K. Komvopoulos, “Analysis of interfacial adhesion based on electrical contact resistance measurements”, Journal of Applied Physics, Vol. 94, No. 10, 2003, pp. 6386-6390.

[78] J.B. Griffis, The Theory of Classical Dynamics, Cambridge University Press, 1985.

[79] K. Miller and R. Clavel, “The Lagrange-based model of Delta-4 robot dynamics”, Robotersysteme, Vol. 8, No. 1, 1992, pp. 49-54.

[80] T. W. Lee and D. C. H. Yang, “On the Evaluation of Manipulator Workspace”, Transactions of the ASME, Journal of Mechanisms, Transmissions, and Automation in Design, Vol. 105, No. 5, 1983, pp. 70-77.

[81] http://www.roymech.co.uk/Useful_Tables/Tribology/co_of_frict.htm